LBL-31622

Lawrence Berkeley Laboratory
UNIVERSITY OF CALIFORNIA

CHEMICAL SCIENCES DIVISION

Potential Energy Surfaces and Reaction Dynamics of Polyatomic Molecules

Y.-T. Chang
(Ph.D. Thesis)

November 1991

Prepared for the U.S. Department of Energy under Contract Number DE-AC03-76SF00098

LBL--31622

DE92 008314

Potential Energy Surfaces and Reaction Dynamics of Polyatomic Molecules

Yan-Tyng Chang
(Ph.D. Thesis)

Department of Chemistry
University of California

and

Chemical Sciences Division
Lawrence Berkeley Laboratory
University of California
Berkeley, CA 94720

November 1991

This work was supported by the Director, Office of Energy Research, Office of Basic Energy Sciences, Chemical Sciences Division, of the U.S. Department of Energy under Contract No. DE-AC03-76SF00098.

Potential Energy Surfaces and Reaction Dynamics of Polyatomic Molecules

Yan-Tyng Chang

Abstract

A simple empirical valence bond (EVB) model approach is suggested for constructing global potential energy surfaces for reactions of polyatomic molecular systems. This approach produces smooth and continuous potential surfaces which can be directly utilized in a dynamical study.

Two types of reactions are of special interest, the unimolecular dissociation and the unimolecular isomerization. For the first type, the molecular dissociation dynamics of formaldehyde on the ground electronic surface is investigated through classical trajectory calculations on EVB surfaces. The product state distributions and vector correlations obtained from this study suggest very similar behaviors seen in the experiments.

The intramolecular hydrogen atom transfer in the formic acid dimer is an example of the isomerization reaction. High level *ab initio* quantum chemistry calculations are performed to obtain optimized equilibrium and transition state dimer geometries and also the harmonic frequencies. A few preliminary dynamical studies based on simple one-dimensional WKB and reaction path Hamiltonian methods are presented. A global potential surface of the formic acid dimer is obtained through a normal mode version of the EVB model which should be reasonable for those systems not undergoing a dramatic change in molecular geometries during the course of the reaction.

Acknowledgments

I wish to express my gratitude to my research advisor, Prof. William H. Miller. Through his guidance and support, I had the opportunity to know and learn a very interesting field, gas phase reaction dynamics. Prof. Henry F. Schaefer III and Dr. Yukio Yamaguchi are acknowledged for teaching me and stimulating my interests in *ab initio* quantum chemistry. I am also grateful to Prof. C. Bradley Moore for his interests and concerns about the formaldehyde project. My research advisor in college, Prof. Tzu-Min Su is thanked for encouraging me to come to Berkeley where I found it to be a wonderful place for doing scientific research.

During my stay at Berkeley, I have shared many things in science and in life with members of the Miller group and many other friends in the department. I thank them for their suggestions, assistance and friendship. Among them, I have collaborated with Dr. Beverly A. Ruf on developing reaction path Hamiltonian for polyatomic molecular systems, and with Dr. Camilla Minichino on constructing global potential energy surface for the dissociation of formaldehyde $H_2CO \rightarrow H_2 + CO$. Dr. Nancy Makri was my TA for quantum mechanics 221B. Her patience and help through the course and useful suggestions for my research are gratefully thanked. Special thanks go to our secretary, Mrs. Cheryn Gliebe, who handled all the important paper work (especially the financial ones) and has been very nice to me. The technical support of computer systems from Rigoberto Hernandez, Dan Gezelter and the staff of computer center are greatly appreciated.

Finally, I want to thank my husband, Johnny, my mother, brothers and sisters. Without their love and encouragement, this work would not have been completed. This dissertation is especially dedicated to the memory of my father. It is his wish that I complete my Ph.D. degree which gives me all the strength through these years.

This research was supported by the Director, Office of Energy Research, Office of Basic Energy Sciences, Chemical Sciences Division of the U.S. Department of Energy under con tract No. DE–AC03-76SF00098, and in part by the National Science Foundation.

Table of Contents

Chapter I
Introduction

A successful theoretical study of chemical reaction dynamics in the gas phase requires developments in two categories: the construction of the potential energy surfaces (PES's) and methods for dynamical calculations on the surfaces. For a simple system involving only three to four atoms, for example the H + H_2 exchange reaction, a quantitative description of the Born-Oppenheimer potential surface with chemical accuracy, can be achieved through modern high level *ab initio* quantum chemistry calculations. Some rigorous quantum mechanical dynamics methods have been developed which give good agreement with experimental results. However, the vast majority of chemical reactions occur in polyatomic molecular systems with 4 to $\sim$ 10 (or even more) atoms. Enormous difficulties arise in trying to obtain the full dimensional potential surface with quantum chemistry, and also in the dynamical simulations of the reaction, due to the large number of degrees of freedom involved. One way of simplifying the problem is to use reduced dimensionality techniques. In such techniques, one studies a similar reaction with smaller dimension and hopes it will mimic the dynamics in the original system of interest. For instance, the intramolecular relaxation of benzene CH local mode overtone has been studied by Lu and Hase[1] with the molecular models HC_3 and H_3C_3

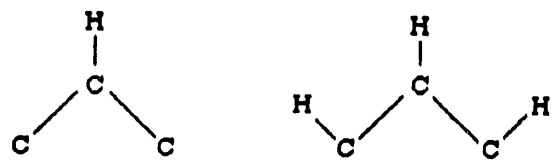

Another popular technique is to use the reaction path Hamiltonian (RPH) developed by Miller, Handy and Adams.[2] Here, typically the steepest descent path (defined in the mass-weighted cartesian coordinates) that starts from the saddle point and

follows the gradients to the reactant and product configurations is calculated. The dynamics are then investigated with an approximate potential surface which consists of the reaction path and local harmonic potentials for vibrational modes that are perpendicular to the reaction coordinate. However, if the reaction involves more than one large amplitude mode or if the reaction path is sharply curved, the RPH is no longer a good approximation. In these cases, the construction of a global PES is inevitable.

In general, the methods[3] of obtaining global PES include (1) fitting *ab initio* data globally in the form of physically meaningful analytical functions or multinomials, or fitting the data locally with cubic splines,[4] and (2) using an approximate surface obtained from empirical or semi-empirical methods. The techniques of diatomics-in-molecules (DIM)[5] and the commonly used London-Eyring-Polanyi-Sato (LEPS)[6] for triatomic systems are just two examples of this second approach. Empirical methods, such as MM2/MM3[7] and AMBER,[8] that are developed for studying near-equilibrium properties of macromolecules in the fields of organic chemistry and biology, could be good candidates for constructing the non-reactive parts of the global PES.

In order to correctly describe the dynamics, at least some of the aspects of the PES have to be reproduced accurately: the equilibrium and transition state geometries, the vibrational frequencies and the reaction barrier height. The surfaces should also be smooth and have continuous first derivatives everywhere. In fact, continuity through higher order derivatives is required if one wishes to calculate the harmonic and/or anharmonic force constants of the potential. The above mentioned semi-empirical and empirical methods frequently suffer the drawbacks of not reproducing the correct transition state geometries and/or having discontinuous derivatives due to improper connections of potential functions. In Chapter II, an approach called the empirical valence bond model (EVB) for constructing global PES is presented. It satisfies most of the important requirements of a good global PES, namely, re-

producing the barrier height and correct geometries, vibrational frequencies of the equilibrium and transition state configurations, and being smooth and continuous through (at least) first derivatives. On the other hand, the requirement of having chemical accuracy (less than 1 kcal/mol error) everywhere on the potential surface is impossible with such a simple method. In fact, the only global PES that is believed to have such an accuracy is the H + H_2 LSTH surface.[9] However, sensitivity analysis of the dynamical quantities such as rate constants, reaction cross sections, product state distributions, etc., on these preliminary global PES's can provide an indication of which regions of the surface are critical and need to be improved.

Two types of polyatomic reactions are of specific interest here. The first one is an unimolecular dissociation and the second, an unimolecular isomerization. Since the invention of modern experimental tools, such as molecular beams and high resolution laser sources, and the new developments of various probing techniques, an understanding of the detailed reaction dynamics for these types of reactions has now become possible. In general, issues such as the time scale of a certain reaction compared to that of energy randomization among various degrees of freedom (i.e.: IVR), the effects of the initial ro-vibrational states, the shape of the potential surfaces, the reaction pathway, the product state distributions and the vector correlations have to be investigated in order to get a complete picture of the reaction.

One of the most well studied photodissociation reactions is that of formaldehyde

$$H_2CO(S_0) + h\nu(280 - 355\text{nm}) \rightarrow H_2CO(S_1, v, J, K_a, K_c)$$

$$\rightarrow H_2CO(S_0^*) \rightarrow H_2(v,j) + CO(v,j).$$

In Chapter III, the method of EVB is used to construct global PES's for formaldehyde, which are then used for dynamical study with classical trajectory simulations.

The results of the product state distributions and the vector correlations are then compared with the experimental observations obtained mostly by Moore and co-workers.[10] From the promising results in our calculations, we feel that the EVB approach certainly provides a good starting strategy for getting a reasonable global PES.

The second reaction studied in this thesis is the intra-molecular double hydrogen atom transfer (an isomerization) reaction in a van der Waals molecule, the formic acid dimer.

This type of reaction can also be found in many chemical and biological systems such as the A-T or G-C base pairs of DNA.[11] Being the simplest carboxyl acid dimer held by two hydrogen bonds, formic acid dimer has been the subject of many experimental and theoretical studies. In Chapter IV, thorough *ab initio* calculations on the IR, and Raman spectra of a few isotopomers of formic acid dimer and the energetics of the dimerization reaction at the SCF level of theory are presented. For the hydrogen transfer reaction, the investigations of the transition state geometry and the corresponding vibrational frequencies are first performed at the SCF level. The potential bare barrier heights obtained by using three different basis sets (STO-3G, DZ and DZ+P) range from 5.2 to 15.6 kcal/mol. Since the reaction rate strongly depends on the potential barrier height, a more elaborate *ab initio* method is necessary in order to get a converged answer.

It is well known that the electron correlation energy for van der Waals molecules cannot be neglected.[12] The classical approach is to use a configuration interaction

(CI) technique.[13] Since more than 90% of the correlation energy comes from double excitation, the most commonly used methods are CI-D and CI-SD. However, these two approaches are not size-consistent,[14] and therefore, are not recommended. Going beyond double excitation, for example CI-SDTQ, certainly reduces the error, but the calculation becomes enormous. Another popular method for treating the electron correlation is the Moller-Plesset (MP) perturbation theory.[13] It provides an economical way without loss of accuracy. Usually, the expansion is truncated after the fourth order. We perform a series of perturbation calculations on the reaction barrier height with increasing order from MP2/DZP to MP4(SDTQ)/DZP. The effect of the size of basis set is also studied by performing a MP2/TZ2P calculation. The converged value of the barrier height is in the range of 7 to 8 kcal/mol. More accurate vibrational frequencies of the MP2/DZP optimized equilibrium dimer and transition state dimer geometries are also performed with analytical methods. This information is very important for the study of the dynamics.

Two simple dynamical models are used to estimate the tunneling splitting of the ground vibrational level of the double hydrogen atom transfer reaction in formic acid dimer. For future classical trajectory simulations of this reaction, we construct a global potential surface for this system using a normal mode version of the EVB model.

References

[1] D.-H Lu and W. L. Hase, *J. Chem. Phys.* **89**, 6723 (1988).

[2] W. H. Miller, N. C. Handy, and J. E. Adams, *J. Chem. Phys.* **72**, 788 (1980).

[3] (a) D. G. Truhlar, R. Steckler, and M. S. Gordon, *Chem. Rev.* **87**, 217 (1987).
(b) G. C. Schatz, *Rev. Mod. Phys.* **61**, 669 (1989).
(c) J. N. L. Connor, *Comput. Phys. Commun.* **17**, 117 (1979).
(d) D. M. Hirst, *Potential Energy Surfaces*, Taylor and Francis, Eds., London (1985).
(e) J. N. Murrell, S. Carter, S. C. Farantos, P. Huxley, and A. J. C. Varandas, *Molecular Potential Energy Functions*, Wiley: New York (1984).
(f) N. Sathyamurthy, *Comput. Phys. Rep.* **3**, 1 (1985).

[4] W. H. Press, B. P. Flannery, S. A. Teukolsky, and W. T. Vetterling, *Numerical Recipes*, Cambridge University Press (1986).

[5] (a) F. O. Ellison, *J. Am. Chem. Soc.* **85**, 3540 (1963).
(b) J. C. Tully, in *Semi-empirical Methods of Electronic Structure Calculation, Part A: Techniques*, Ed. G. D. Segal, Plenum: New York (1977), Chap. 6.

[6] (a) S. Sato, *J. Chem. Phys.* **23**, 592 (1955).
(b) S. Sato, *Bull. Chem. Soc. Jpn.* **28**, 450 (1955).
(c) S. Sato, *J. Chem. Phys.* **23**, 2465 (1955).

[7] (a) N. L. Allinger, *J. Am. Chem. Soc.* **99**, 8127 (1977).
(b) N. L. Allinger, Y. H. Yuh, and J.-H. Lii, *J. Am. Chem. Soc.* **111**, 8551 (1989).
(c) J.-H. Lii and N. L. Allinger, *J. Am. Chem. Soc.* **111**, 8566 (1989).
(d) J.-H. Lii and N. L. Allinger, *J. Am. Chem. Soc.* **111**, 8576 (1989).

[8] (a) P. K. Weiner and P. A. Kollman, *J. Comput. Chem.* **2**, 287 (1981).
(b) S. J. Weiner, P. A. Kollman, D. A. Case, U. C. Singh, C. Ghio, G. Alagona, S. Profeta Jr., and P. Weiner, *J. Am. Chem. Soc.* **106**, 765 (1984).
(c) S. J. Weiner, P. A. Kollman, D. T. Nguyen, and D. A. Case, *J. Comput. Chem.* **7**, 230 (1986).

[9] (a) P. Siegbahn and B. Liu, *J. Chem. Phys.* **68**, 2457 (1978).
(b) D. G. Truhlar and C. J. Horowitz, *J. Chem. Phys.* **68**, 2466 (1978); **71**, 1514(E) (1979).

[10] (a) C. B. Moore and J. C. Weisshaar, *Ann. Rev. Phys. Chem.* **34**, 525 (1983).
(b) D. R. Guyer, W. F. Polik, and C. B. Moore, *J. Chem. Phys.* **84**, 6519 (1986).
(c) H. Bitto, D. R. Guyer, W. F. Polik, and C. B. Moore, *Faraday Discuss. Chem. Soc.* **82**, 149 (1986).
(d) W. F. Polik, D. R. Guyer, and C. B. Moore, *J. Chem. Phys.* **92**, 3453

(1990).
(e) P. Ho, D. J. Bamford, R. J. Buss, Y. T. Lee, and C. B. Moore, *J. Chem. Phys.* **76**, 3630 (1982).
(f) M. Pealat, D. Debarre, J. M. Marie, J. P. E. Taran, A. Tramer, and C. B. Moore,*Chem. Phys. Lett.* **98**, 299 (1983).
(g) D. Debarre, M. Lefebvre, M. Pealat, J. P. E. Taran, D. J. Bamford, and C. B. Moore, *J. Chem. Phys.* **83**, 4476 (1985).
(h) P. Ho and A. V. Smith,*Chem. Phys. Lett.* **90**, 407 (1982).
(i)D. J. Bamford, S. V. Filseth, M. F. Foltz, J. W. Hepbun, and C. B. Moore, *J. Chem. Phys.* **82**, 3032 (1984).
(j) T. J. Butenhoff, K. L. Carleton, and C. B. Moore, *J. Chem. Phys.* **92**, 377 (1990).
(k) T. J. Butenhoff, K. L. Carleton, M.-C. Chuang, and C. B. Moore, *J. Chem. Soc., Faraday Trans.* **85**, 1155 (1989).
(l) K. L. Carleton, T. J. Butenhoff, and C. B. Moore, *J. Chem. Phys.* **93**, 3907 (1990).
(m) T. J. Butenhoff, K. L. Carleton, R. D. van Zee, and C. B. Moore, *J. Chem. Phys.* **94**, 1947 (1990).
(n) T. J. Butenhoff, Ph. D. Thesis, U. C. Berkeley (1990).

[11] S. Scheiner and C. W. Kern, *J. Am. Chem. Soc.* **101**, 4081 (1979).

[12] (a) P. Hobza and R. Zahradnik, *Chem. Rev.* **88**, 871 (1988).
(b) A. D. Buckingham, P. W. Fowler, and J. M. Hutson, *Chem. Rev.* **88**, 963 (1988).

[13] (a) J. A. Pople, J. S. Binkley, and R. Seeger, *Int. J. Quantum Chemistry Symp.* **10**, 1 (1976).
(b) J. A. Pople, R. Seeger, and R. Krishnan, *Int. J. Quantum Chemistry Symp.* **11**, 149 (1977).
(c) R. J. Bartlett, *Ann. Rev. Phys. Chem.* **32**, 359 (1981).

[14] A. Szabo and N. S. Ostlund, *Modern Quantum Chemistry*, Macmillan: New York (1982).

Chapter II
The Empirical Valence Bond Model

1 Introduction

One of the most difficult steps in theoretical treatments of chemical reactions in polyatomic molecular systems is representing the potential energy surface.[1] Ideally, of course, one would like to be able to compute the Born-Oppenheimer electronic energy $V(q_1, \ldots, q_{3N-6})$ from the first principles for any values of the 3N-6 coordinates that are necessary to specify the configuration of the N atom system. Though *ab initio* quantum chemistry calculations[2] are becoming increasingly possible for polyatomic molecular systems, the number of such calculations needed for more than 3 or 4 atom systems tends to make this direct approach unfeasible.

One of the ways used for dealing with the situation has been to exploit the idea of a reaction path.[3–5] Here one computes the potential energy surface only along a one-dimensional curve(the reaction path) in the 3N-6 dimensional space that connects reactant and product configurations. This is often the steepest descent path (in mass-weighted cartesian coordinates) that passes through the transition state for the reaction under study – the "intrinsic" reaction path[5] – but other paths are possible[6] and sometimes more useful.[7] One typically also determines the force constant matrix along this path, thus providing a local harmonic approximation to the potential energy surface along the reaction (or reference) path.

Though reaction path approaches have been very useful, particularly for qualitative and approximate dynamical treatments, and will certainly continue to be so, there are times when a global potential energy surface is needed. This is true, for example, for highly vibrationally excited molecules, where the dynamics tends not

to be localized about any one reaction path, and also for large amplitude motion far away from any reference path.

For vibrational motions about stable molecular geometries a standard normal mode expansion – harmonic plus perhaps anharmonic corrections – provides an adequate global potential function. There also exist a number of completely empirical potential functions[8–12] that describe a variety of non-reactive motions and interactions. Unless special alterations are made, however, these potential functions are not capable of modeling the potential energy surface for a chemical reaction.

In this chapter we wish to pursue and develop an approach used by Warshel[13] that is especially designed to model reactive potential functions, namely the empirical valence bond (EVB) model. To illustrate the basic idea, consider an isomerization reaction such as

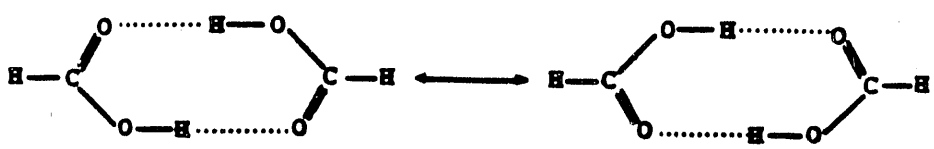

(1) (2) (1)

which is characterized by a muti-dimensional double well potential function. One imagines that this Born-Oppenheimer potential energy surface results from a quantum chemistry calculation with a 2-state valence bond electronic wavefunction

$$|\Psi\rangle = c_1|\phi_1\rangle + c_2|\phi_2\rangle, \tag{2}$$

where $|\phi_1\rangle$ is a valence bond wavefunction that describes the electronic structure of the reactant (1) in Eq.(1) and $|\phi_2\rangle$ the corresponding wave function that describes

the electronic structure of the product (2). The lowest electronic eigenvalue, i.e., the Born-Oppenheimer potential energy surface, is then given by the lower root of the 2×2 secular equation, specifically

$$V = \frac{1}{2}(V_{11} + V_{22}) - \left[\left(\frac{V_{11} - V_{22}}{2}\right)^2 + {V_{12}}^2\right]^{\frac{1}{2}}, \tag{3}$$

where

$$V_{11} = \langle \phi_1 | H_{el} | \phi_1 \rangle,$$

$$V_{22} = \langle \phi_2 | H_{el} | \phi_2 \rangle,$$

$$V_{12} = \langle \phi_1 | H_{el} | \phi_2 \rangle,$$

and H_{el} is the electronic Hamiltonian. V is a function of the nuclear coordinates $\mathbf{q} \equiv (q_1, \ldots, q_{3n-6})$ because the electronic Hamiltonian depends on $\mathbf{q}$, and thus V_{11}, V_{22} and V_{12} also do.

In the *empirical* valence bond approach, however, no electronic matrix elements are actually calculated. $V_{11} \equiv V_{11}(q_1, \ldots, q_{3N-6})$ is identified as the potential energy surface for the reactants and thus taken as a nonreactive (i.e., single minimum) potential energy surface that describes the nonreactive motion about the reactant geometry. The simplest imaginable model for $V_{11}(\mathbf{q})$ would be a harmonic normal-mode approximation about the reactant equilibrium geometry. At a more sophisticated level, one could use one of the nonreactive empirical potential models[8-12] that has the bonding designated as in (1) of Eq.(1). $V_{22}(\mathbf{q})$ is similarly a nonreactive (i.e., single minimum) potential energy surface that describes motion about the

product geometry. V_{11} and V_{22} are often referred to as *diabatic* potential surfaces, in constrast to V itself which is the Born-Oppenheimer or *adiabatic* potential surface.

The most crucial part of the EVB model is the exchange matrix element (or resonance integral) $V_{12} = V_{12}(\mathbf{q})$, for it is less obvious how it should be chosen. Warshel[13] has used some very simple approximations in his (very complex) applications, while we describe a more rigorous way of choosing it which is feasible for modest size polyatomic systems. Specifically, in section 2 it is shown how $V_{12}(\mathbf{q})$ can be chosen so that the EVB potential V($\mathbf{q}$) of Eq.(3) exactly reproduces a given harmonic force field about a given transition-state geometry.[14] We envision that the transition state quantities(geometry, energy, and force constant matrix) will be obtained by *ab initio* quantum chemistry calculations. That is, the logic of the approach is that *ab initio* calculations of useful accuracy can be carried out for a few selected features of the reactive potential surface, and the most important of these are the transition state parameters since this is the least well-known region of the potential. The reactant and product regions are described reasonably well by simple (non-reactive) empirical potential functions[8-12] for stable molecules. The EVB model that we present is thus a way of incorporating *ab initio* calculations for the transition-state parameters with simple diabatic potential functions that describe reactants and products separately.

Some other related work that bears reference is that of Ross and co-workers[15] in which a diabatic electronic representation is introduced as an aid in treating the *dynamics* of the reaction (specifically in deriving Frank-Condon approximations for product-state distribution); such, of course, is not the purpose here. Also related is the work by Downing *et al.*[16] in which the diabatic potential form, Eq.(3), is used (with linear approximations for the matrix elements) to fit single-minimum potential energy surfaces(e.g. that for H_2O[16(b)]).

Section 3 shows how the EVB model that we present is able to provide a good description of reactive potential surfaces for a wide variety of test potential functions

for isomerization reactions such as Eq.(1). It is also shown in section 4 that the EVB model can also be applied to cases that the reactants and/or products are dissociative states.

2 Choosing the Exchange Matrix Element

The potential energy surface V(q) is thus taken to be in the form of Eq.(3), where the diabatic potentials $V_{11}(\mathbf{q})$ and $V_{22}(\mathbf{q})$ are nonreactive (i.e., single minimum) potential functions that correctly describe the regions near the equilibrium geometries $\mathbf{q}_1$ and $\mathbf{q}_2$, respectively. V_{11} and V_{22} are assumed to be known, and the goal here is to find a useful way of determining the exchange matrix element $V_{12}(\mathbf{q})$. It is clear that in the reactant or product regions themselves, i.e., for $\mathbf{q}$ near $\mathbf{q}_1$ or $\mathbf{q}_2$, one will have

$$V_{12}^2 \ll \left(\frac{V_{11} - V_{22}}{2}\right)^2, \tag{4.a}$$

and in this limit it is easy to see that Eq.(3) gives

$$V(\mathbf{q}) \approx min\left[V_{11}(\mathbf{q}), V_{22}(\mathbf{q})\right], \tag{4.b}$$

which is clearly correct in these regions. It is thus only necessary to know $V_{12}(\mathbf{q})$ in the intermediate region between reactants and products, and to determine it in this region we appeal to *ab initio* quantum chemistry.

Equation (3) can be used to express V_{12} in terms of V_{11}, V_{22}, and V as follows:

$$V_{12}(\mathbf{q})^2 = \left[V_{11}(\mathbf{q}) - V(\mathbf{q})\right]\left[V_{22}(\mathbf{q}) - V(\mathbf{q})\right]. \tag{5}$$

Near the transition-state geometry one has

$$V(\mathbf{q}) \approx V_0 + \frac{1}{2}(\mathbf{q}-\mathbf{q}_0)\cdot\mathbf{K}_0\cdot(\mathbf{q}-\mathbf{q}_0), \tag{6}$$

where the transition-state geometry $\mathbf{q}_0$, energy V_0, and force constant matrix $\mathbf{K}_0$ are obtained from an independent *ab initio* calculation. Since the nonreactive potential functions $V_{11}(\mathbf{q})$ and $V_{22}(\mathbf{q})$ are known, they can also be expanded in a Taylor's series about the transition state geometry

$$V_{nn}(\mathbf{q}) = V_n + \mathbf{D}_n\cdot\Delta\mathbf{q} + \frac{1}{2}\Delta\mathbf{q}\cdot\mathbf{K}_n\cdot\Delta\mathbf{q}, \tag{7}$$

where $\Delta\mathbf{q} = \mathbf{q}-\mathbf{q}_0$

$$V_n = V_{nn}(\mathbf{q}_0),$$

$$\mathbf{D}_n = \left(\frac{\partial V_{nn}(\mathbf{q})}{\partial \mathbf{q}}\right)_{\mathbf{q}=\mathbf{q}_0},$$

$$\mathbf{K}_n = \left(\frac{\partial^2 V_{nn}(\mathbf{q})}{\partial \mathbf{q}\partial\mathbf{q}}\right)_{\mathbf{q}=\mathbf{q}_0},$$

for n=1,2. With Eqs.(6) and (7), Eq.(5) thus gives the following power series expansion for V_{12}^2, correct through quadratic order in $\Delta\mathbf{q}$

$$\begin{aligned} V_{12}^2 = {} & (V_1-V_0)(V_2-V_0) + (V_2-V_0)\mathbf{D}_1\cdot\Delta\mathbf{q} \\ & + (V_1-V_0)\mathbf{D}_2\cdot\Delta\mathbf{q} + \frac{1}{2}(V_1-V_0)\Delta\mathbf{q}\cdot(\mathbf{K}_2-\mathbf{K}_0)\cdot\Delta\mathbf{q} \\ & + \frac{1}{2}(V_2-V_0)\Delta\mathbf{q}\cdot(\mathbf{K}_1-\mathbf{K}_0)\cdot\Delta\mathbf{q} + (\mathbf{D}_1\cdot\Delta\mathbf{q})(\mathbf{D}_2\cdot\Delta\mathbf{q}). \end{aligned} \tag{8}$$

A cumulant resummation,[17] though, gives better extrapolation properties ; therefore $V_{12}(\mathbf{q})^2$ is taken to be a generalized Gaussian

$$V_{12}(\mathbf{q})^2 = A \exp\left[\mathbf{B}\cdot\Delta\mathbf{q} - \frac{1}{2}\Delta\mathbf{q}\cdot\mathbf{C}\cdot\Delta\mathbf{q}\right], \tag{9}$$

and this function is expanded through quadratic order in $\Delta\mathbf{q}$ and equated to the corresponding terms on the right-hand side of Eq.(8) to determine the parameters A, $\mathbf{B}$(a vector), and $\mathbf{C}$(a matrix). The arithmetic is straightforward and one obtains

$$A = (V_1 - V_0)(V_2 - V_0), \tag{10.a}$$

$$\mathbf{B} = \frac{\mathbf{D}_1}{(V_1 - V_0)} + \frac{\mathbf{D}_2}{(V_2 - V_0)}, \tag{10.b}$$

$$\mathbf{C} = \frac{\cdot\mathbf{D}_1\mathbf{D}_1\cdot}{(V_1 - V_0)^2} + \frac{\cdot\mathbf{D}_2\mathbf{D}_2\cdot}{(V_2 - V_0)^2} + \frac{\mathbf{K}_0 - \mathbf{K}_1}{(V_1 - V_0)} + \frac{\mathbf{K}_0 - \mathbf{K}_2}{(V_2 - V_0)}. \tag{10.c}$$

For completeness, we note that if the intermediate position $\mathbf{q}_0$ is actually not the transition-state geometry, so that Eq.(6) has a linear term $\mathbf{D}_0\cdot\Delta\mathbf{q}$, then Eqs.(8)-(10) still apply if the following change is made in (8), (10.b), and (10.c)

$$\mathbf{D}_n \rightarrow \mathbf{D}_n - \mathbf{D}_0, \tag{10.d}$$

for n=1,2.

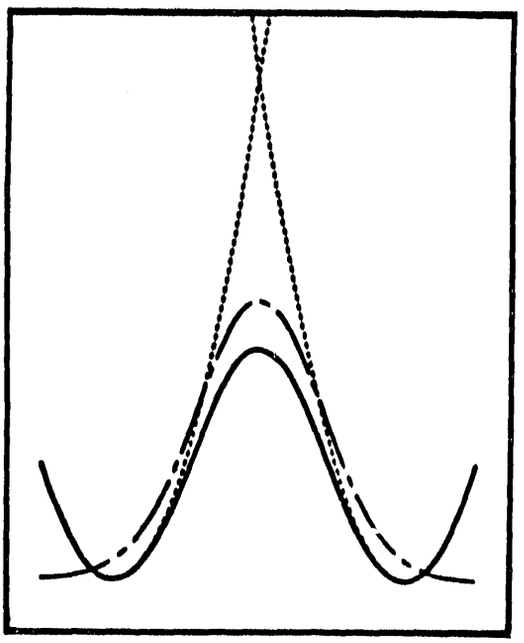

Figure 1: A one dimensional model with the diabatic potentials V_{11} and V_{22} shown with dotted lines, the adiabatic potential V with solid line and the exchange potential V_{12} with long-dashed line.

Equations (9)-(10) are the basic theoretical result of this chapter. They give a very simple prescription for the exchange matrix element that will cause the EVB potential, equation (3), to reproduce a given harmonic force field about a given transition-state (or any other intermediate) geometry. Because of its Gaussian form, as is illustrated in Figure 1, V_{12} is damped out away from this region so that the EVB expression (Eq.(3)) reduces to V_{11} or V_{22} in the reactant and product regions. It thus provides a useful way to incorporate *ab initio* quantum chemistry calculations for the transition state with simple empirical potential functions which model the nonreactive motions of the reactants and products.

3 Model Potentials for Isomerization Reactions

Here we test the empirical valence bond (EVB) model on a series of two-dimensional problems to illustrate its capabilities (and limitions) in a variety of situations. The first example is a two-dimensional double-well potential function that has been used previously[18] as a test of various dynamical theories and also as a model for isomerization reactions such as Eq.(1). The specific form of the potential function is

$$V(s,Q) = V_0(s) + \frac{1}{2}m\omega^2\left(Q - \frac{cs^n}{m\omega^2}\right)^2, \tag{11}$$

where $V_0(s)$ is a one-dimensional symmetric double-well potential and c is a coupling constant which characterizes the strength of the coupling between the "reaction coordinate" s and the "bath mode" Q. Written in this renormalized form, the barrier height is independent of the coupling constant. $n = 1$ or 2 in Eq.(11) determines the symmetry of the coupling. In all cases the mass m is that of a hydrogen atom and the one-dimensional double-well potential is

$$V_0(s) = \frac{1}{2}(v_{11}(s) + v_{22}(s)) - \left[\left(\frac{v_{11}(s) - v_{22}(s)}{2}\right)^2 + v_{12}(s)^2\right]^{1/2}, \tag{12.a}$$

where

$$v_{11}(s) = \frac{1}{2}m\omega_0^2(s + s_0)^2, \tag{12.b}$$

$$v_{22}(s) = \frac{1}{2}m\omega_0^2(s - s_0)^2, \tag{12.c}$$

$$v_{12}(s) = a\exp(-bs^2), \tag{12.d}$$

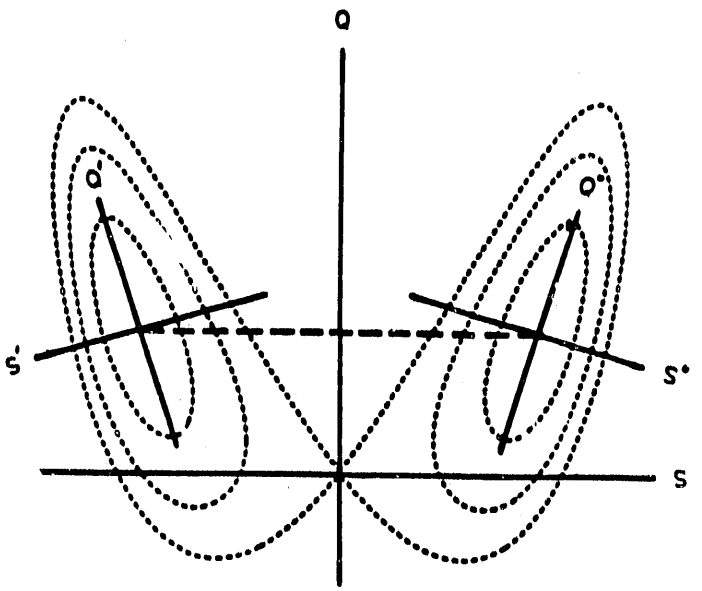

Figure 2: Definition of coordinates.

with parameters $\omega_0 = 1600$ cm^{-1}, $s_0 = 1$, $a = 0.036065963$, and $b = 1.81678095$ (all distance in atomic units). These parameters yield a barrier height of ~ 8.2 kcal/mol, which is typical of H atom transfer.

Sections 3.1 and 3.2 compare the true potential, Eqs.(11)-(12), and the EVB approximation to it given by Eqs.(3) and (9)-(10). The case of a low-frequency ($\omega \simeq 300$ cm^{-1}) bath mode is considered in section 3.1 and that of a high-frequency ($\omega \simeq 3000$ cm^{-1}) bath in section 3.2. In most cases the diabatic potentials V_{11} and V_{22} are taken as the harmonic normal-mode potentials for reactants and products, i.e.,

$$V_{11}(s,Q) = 1/2m\omega_1^2 s'^2 + 1/2m\omega_2^2 Q'^2, \qquad (13.a)$$

$$V_{22}(s,Q) = 1/2m\omega_1^2 s''^2 + 1/2m\omega_2^2 Q''^2, \qquad (13.b)$$

where s' and Q' are the normal-mode coordinates (linear combinations of s and Q as shown in Figure 2) about the reactant minimum on the potential surface and s'' and Q'' are the product normal-mode coordinates. (The normal-mode frequencies ω_1 and ω_2 are the same for reactants and products in this example because of symmetry). As discussed in the Introducion, this is the simplest possible choice for the diabatic potentials.

Some of the applications in sections 3.1 and 3.2 show how the EVB model can be improved by including anharmonicities in the diabatic potentials; i.e., the harmonic potentials Eq.(13.a) are replaced by Morse Potentials

$$\frac{1}{2}m\omega_1^2 s'^2 \rightarrow D_1(1 - e^{-\alpha_1 s'})^2, \qquad (14.a)$$

$$\frac{1}{2}m\omega_2^2 Q'^2 \rightarrow D_2(1 - e^{-\alpha_2 Q'})^2, \qquad (14.b)$$

where the Morse paramters are chosen to approximate the potential about the reactant minimum(and similarly for the product potential in Eq.(13.b)).

3.1 Low-Frequency Bath Mode

Figure 3 shows a contour plot of the uncoupled (c=0) potential surface, Eqs.(11)-(12), for the case of a low-frequency ($\omega \simeq 300$ cm^{-1}) bath mode. Since the one-dimensional double-well functions $V_0(s)$ of Eq.(12) is of EVB form, it is clear the general EVB model, Eqs.(3) and (9)-(10), will exactly reproduce the potential in the uncoupled limit. It is thus of interest to see how the EVB model performs as the coupling c is increased.

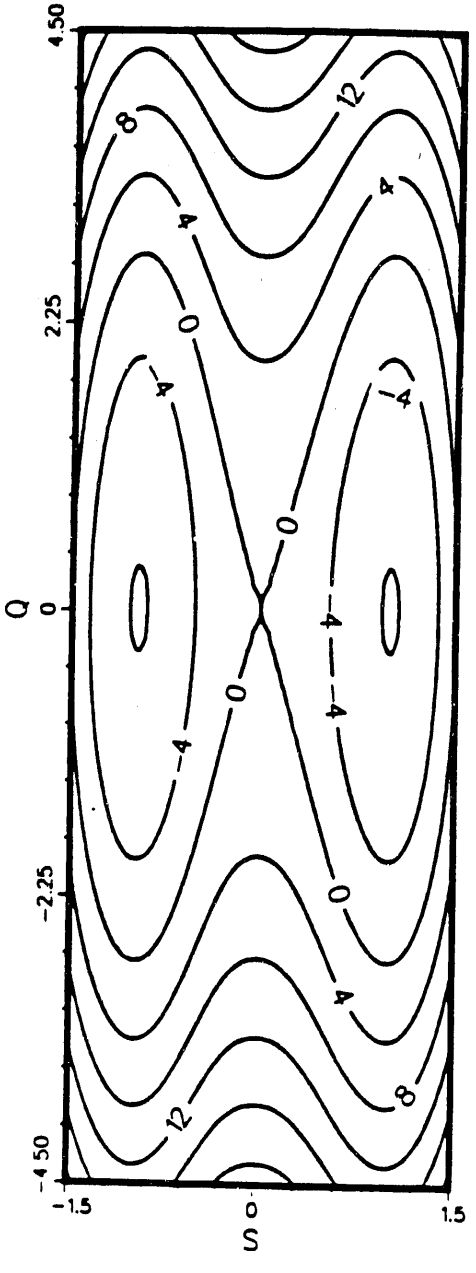

Figure 3: The double well potential energy surface of Eq.(11), for the uncoupled case ($c = 0$) and a low-frequency ($\omega = 300$ cm^{-1}) bath mode Q. The coordinates are in atomic units and the contour values in kcal/mol.

Figure 4, a and b, shows contour plots of the original potential and the EVB approximation to it, respectively, for a modest size even (n=2 in Eq.(11)) coupling constant. A typical example for this type of coupling is found for the formic acid dimer (shown below) with s being the reaction coordinate of the double hydrogen atom transfer defined at the transition state and Q as one of the normal modes with A_g symmetry. Though some quantitative differences are apparent in this model calculation, on the whole the EVB model does an excellent job in representing the important regions of the potential energy surface.

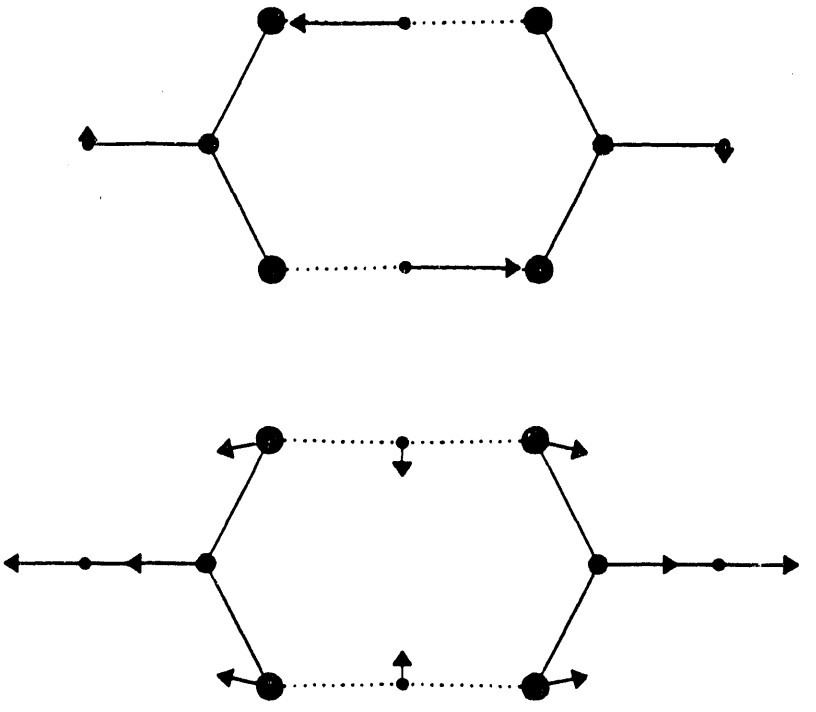

The three different types of atom are represented with solid circles of decreasing sizes, i.e., O > C > H. Top: Eigenvector of the reaction coordinate of the double H atom transfer reaction in formic acid dimer. Bottom: Eigenvector of a low frequency normal mode with A_g symmetry.

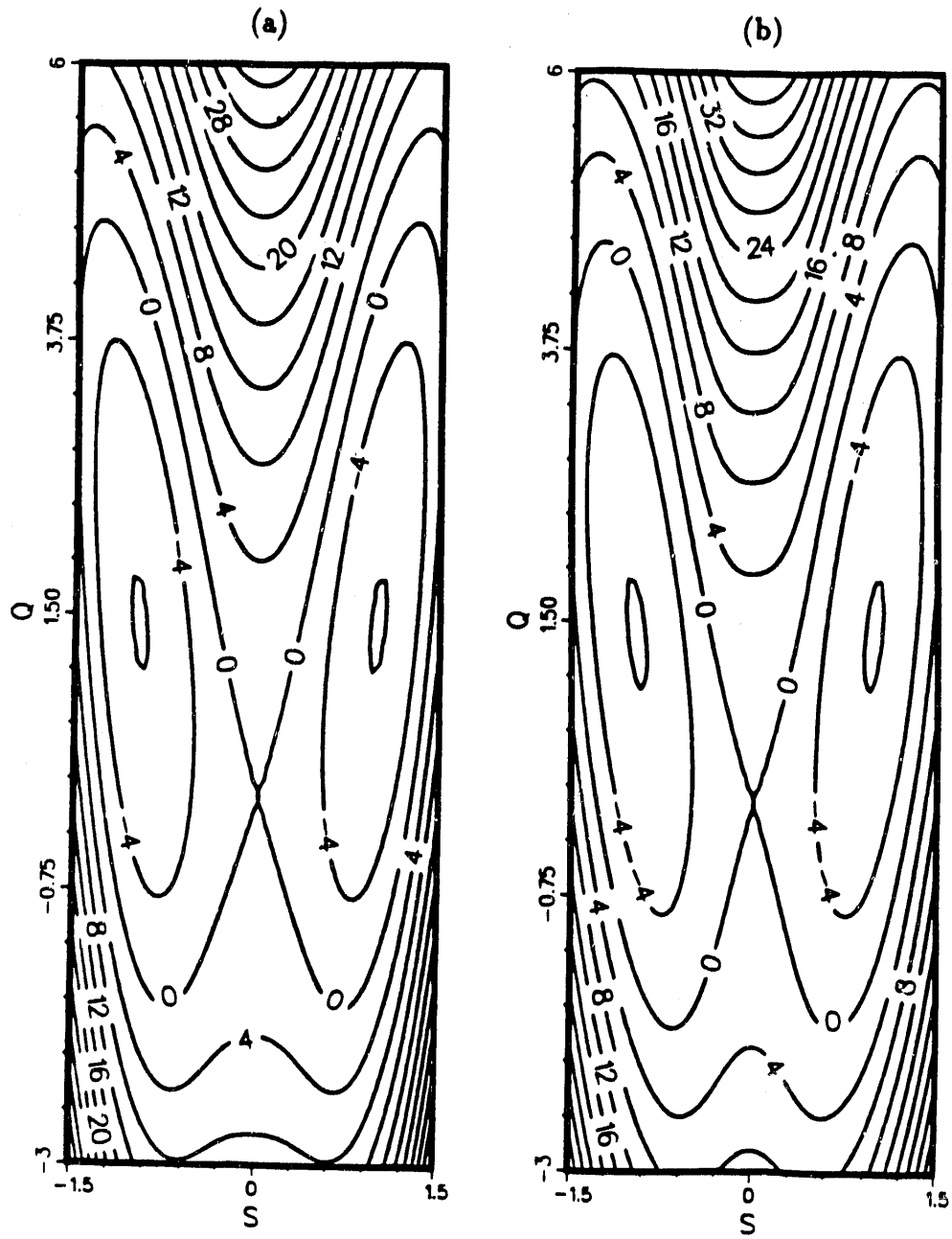

Figure 4: Same as Figure 3, but for even (n=2) coupling with the constant c = 0.005: (a) the origininal potential of Eq.(11); (b) the EVB approximation given by Eqs.(3) and (9)-(10), with the harmonic diabatic potentials of Eq.(13).

Figure 5a,b shows a similar comparison for the case odd (n=1 in Eq.(11)) coupling constant. (This example is very close to a two-dimensional potential of formic acid dimer, with the reaction coordinate coupled to the normal mode shown below.)

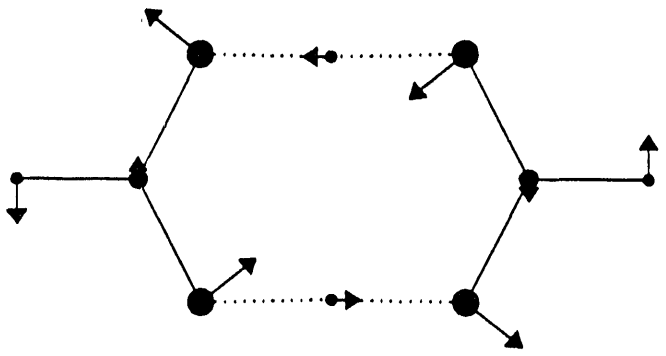

Though the coupling causes a dramatic change in the potential surface from the uncoupled case in Figure 3, one sees that EVB model again provides an excellent description of this potential surface.

Finally, for the case of even coupling we increased the coupling constant c until significant discrepancies are seen in the EVB approximation. (For the case of odd coupling, it is hard to imagine that one would even be interested in coupling any stronger than that shown in Figure 5.) Figure 6a,b shows the original potential and its EVB approximation for this very strong even coupling case. Though the EVB model reproduces the transition-state region correctly—as it must, by construction—the shoulder of the potential between the reactant and product minima is not described well. This is a serious shortcoming since one knows that the tunneling dynamics between reactants and products is sensitive to this region of the

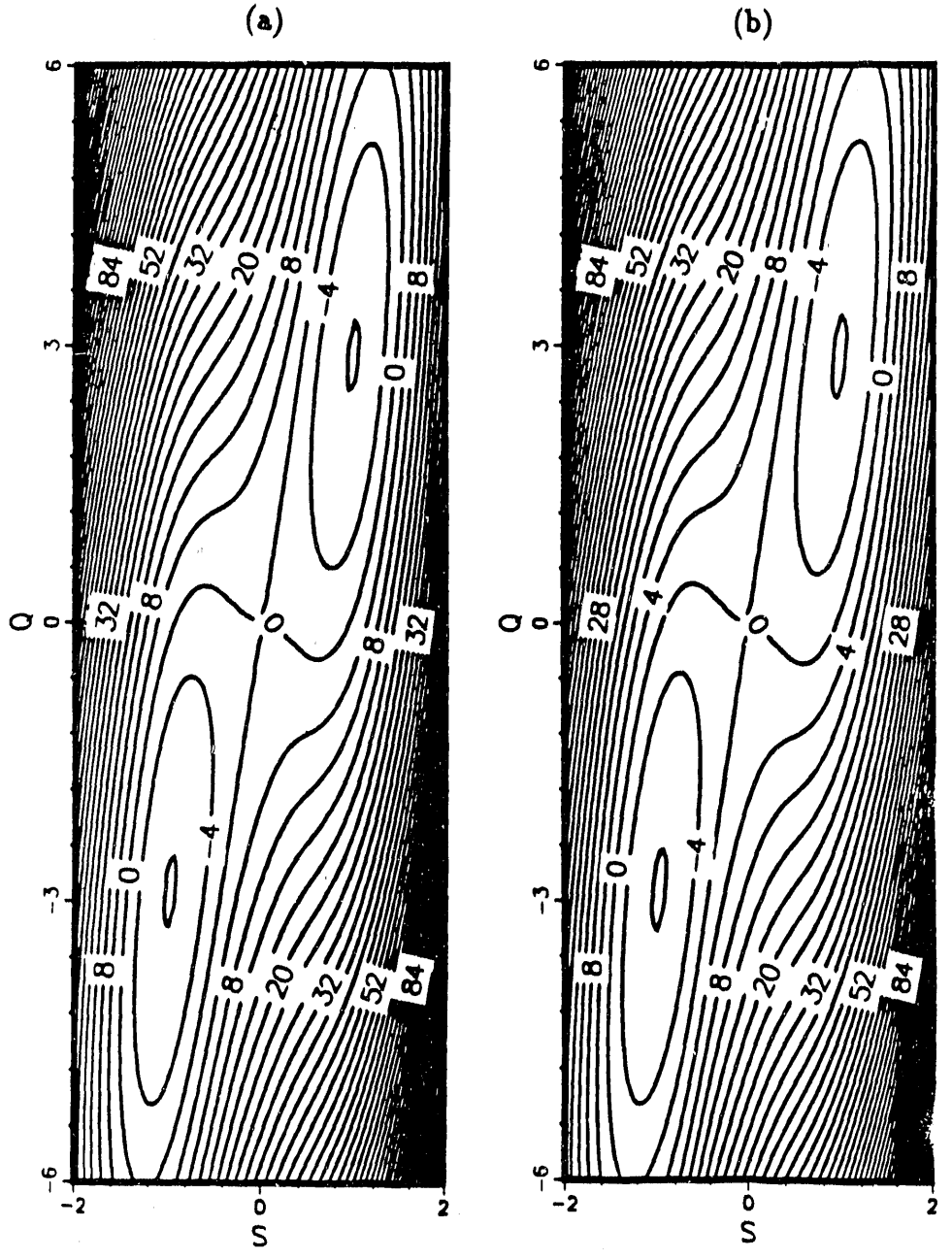

Figure 5: Same as Figure 3, but for odd (n=1) coupling with the constant c=0.01: (a) the original potential; (b) the EVB approximation (with harmonic diabatic potentials).

potential surface.

We thus tried the alternate version of the EVB model noted in section 2; namely, the point $\mathbf{q}_0$ at which the EVB potential is required to match the true potential through quadratic order was chosen not to be the transition state, the saddle point on the potential, but rather the *midpoint* between the reactant and product equilibrium geometries. (This is very much in the spirit of the straight-line reaction path model, shown as dashed line in Fig. 2, that was recently discussed in ref.7(b).) Fig.6c shows this modified EVB potential. The region of the potential between the reactant and product wells is indeed in much better agreement with the true potential (Fig.6a) than the initial EVB result (Fig.6b). Even though the transition-state region is not described as well, this modified EVB potential would probably be better for treating the tunneling motion between reactants and products.

However there is another way to improve the EVB model, and that is to use better diabatic potential functions V_{11} and V_{22}. Thus, the harmonic potentials about the reactant and product minimum were replaced by Morse potentials, as indicated in Eq.(14), which best represent the diagonal anharmonicity in the normal-mode directions. (This is really only important for the high-frequency mode; the anharmonic correction for the low-frequency mode has essentially no effect.) Figure 6d shows the EVB potential that results in this case (where the "fitting point" $\mathbf{q}_0$ for defining the exchange potential V_{12} was taken as the transition state), and one sees that it is indeed in much better agreement with the true potential (Figure 6a), in both the transition-state region and also the shoulder region directly between reactants and products. This EVB potential appears adequate for describing all important aspects of this potential surface.

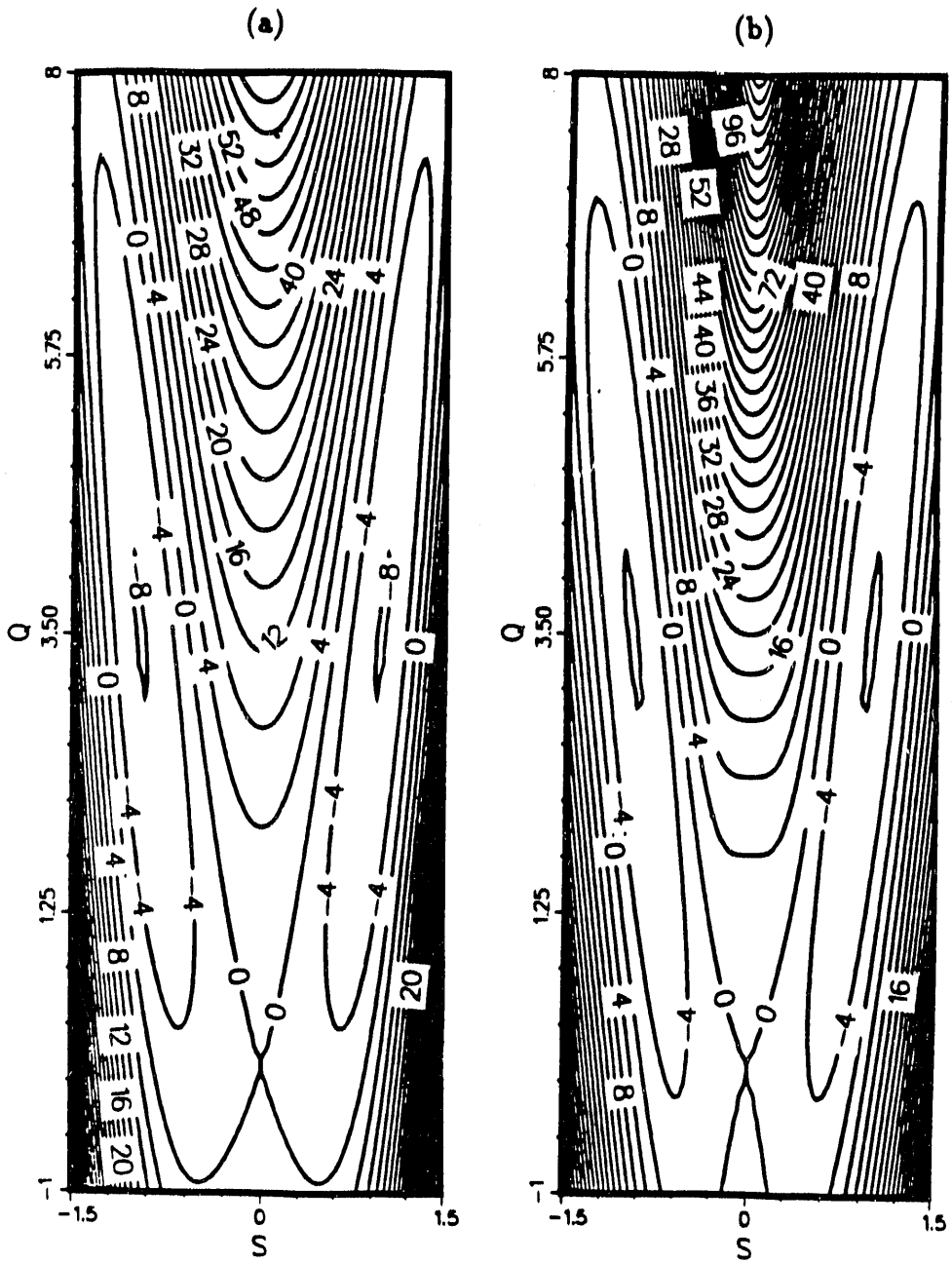

Figure 6: Same as Figure 4 (even coupling), but with the larger coupling constant $c = 0.0125$: (a)the original potential; (b) the EVB approximation with harmonic diabatic potentials.

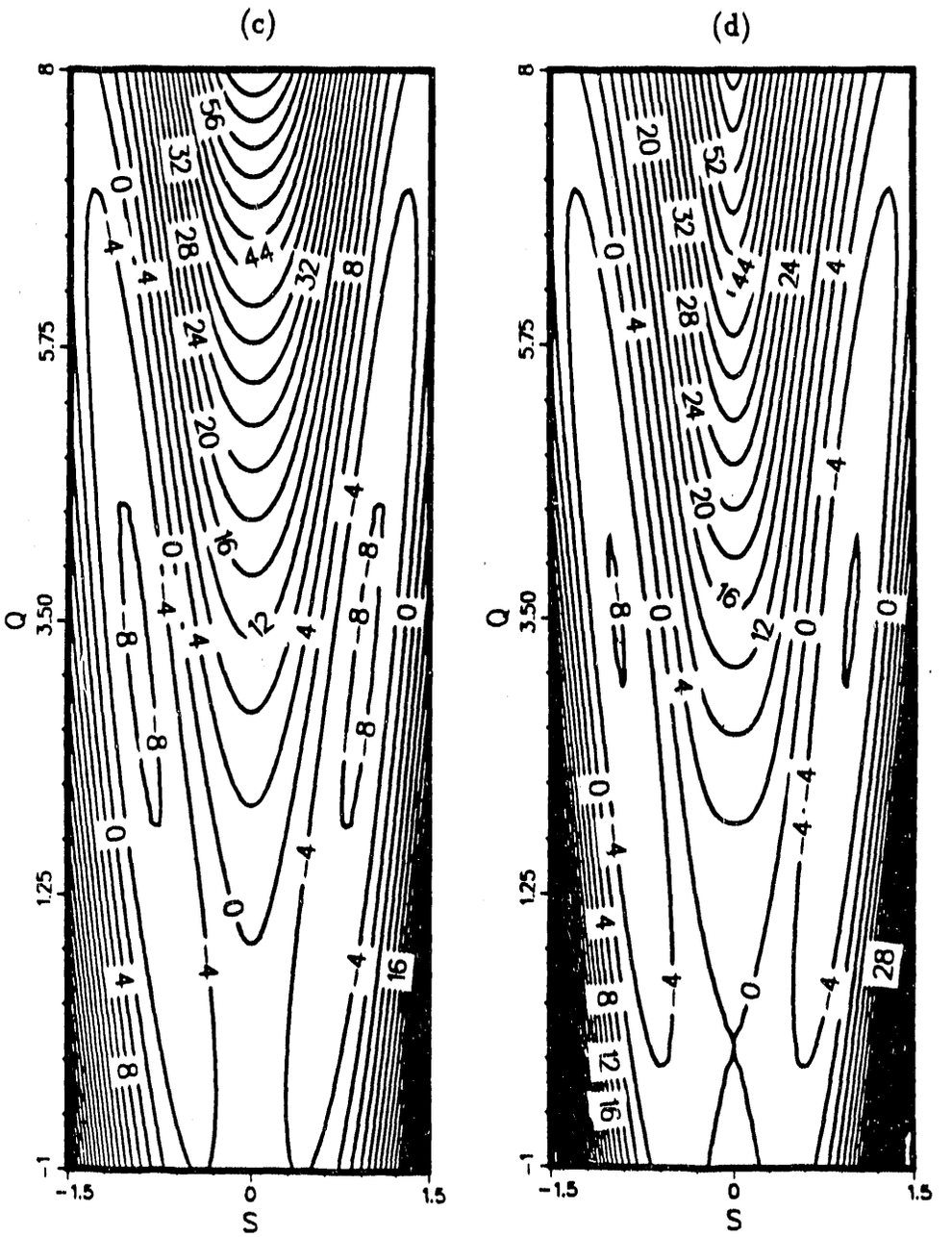

Figure 6, continued. (c) the modified EVB potential, where the matching point is the midpoint between the reactant and product minima rather than the saddle point (the transition state); (d) the EVB approximation (with the matching point at the transition state) with the anharmonic diabatic potentials of Eq.(14).

3.2 High-Frequency Bath Mode

High-frequency bath modes are usually easier to describe correctly than low-frequency ones because the steeper harmonic potential does not allow far as large excursions in such degrees of freedom. Fig.7 shows the uncoupled (c=0) double-well potential function of Eq.(11) for the case of a high-frequency (ω = 3000 cm^{-1}) bath mode. Again, the EVB model exactly reproduces the potential in the uncoupled limit, so we consider its behavior for nonzero coupling.

Figure 8, a and b, shows the original potential and its EVB approximation, respectively, for the case of even coupling, and Figure 9a,b shows a similar comparison for odd coupling, both for fairly large coupling constants. (The potential wells are displaced less drastically from their uncoupled position than for the low-frequency case because the high frequency of the bath mode makes the potential "stiffer" with regards to perturbation in the Q direction.) In both cases one sees that the EVB model provides an excellent description of the true potential.

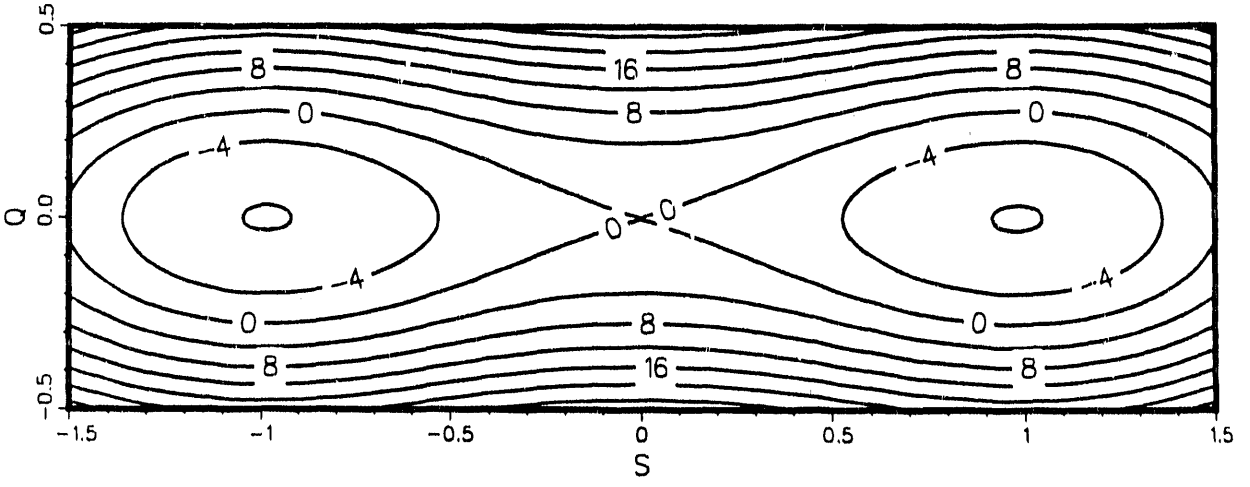

Figure 7: Te double well potential function of Eq.(11), for the uncoupled case (c = 0) and a hig-frequency (ω = 3000 cm^{-1}) bath mode Q.

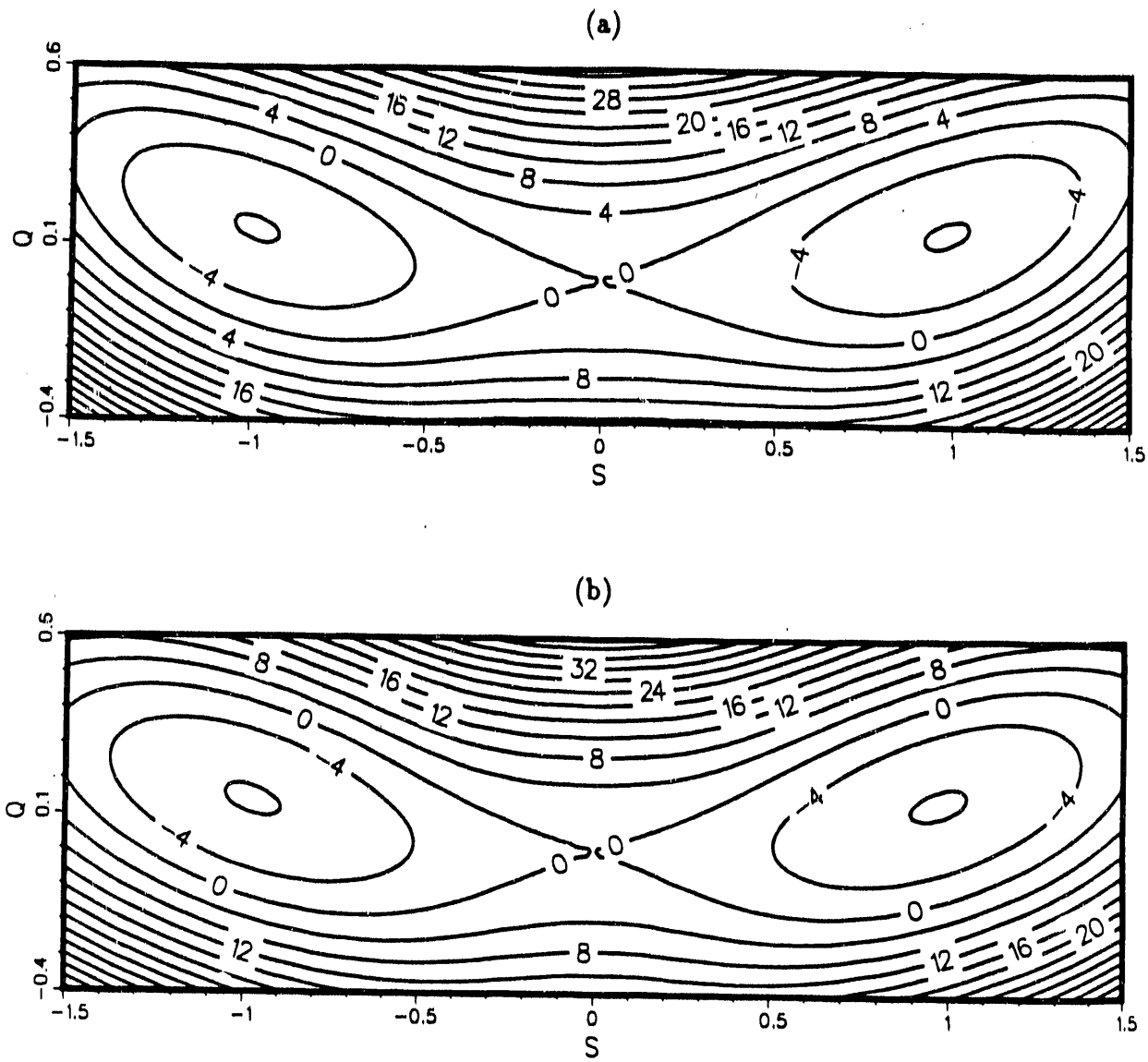

Figure 8: Same as Figure 7, but for even (n=2) coupleing with the constant c = 0.05: (a) the original potential; (b) the EVB approximation (with harmonic diabatic potentials).

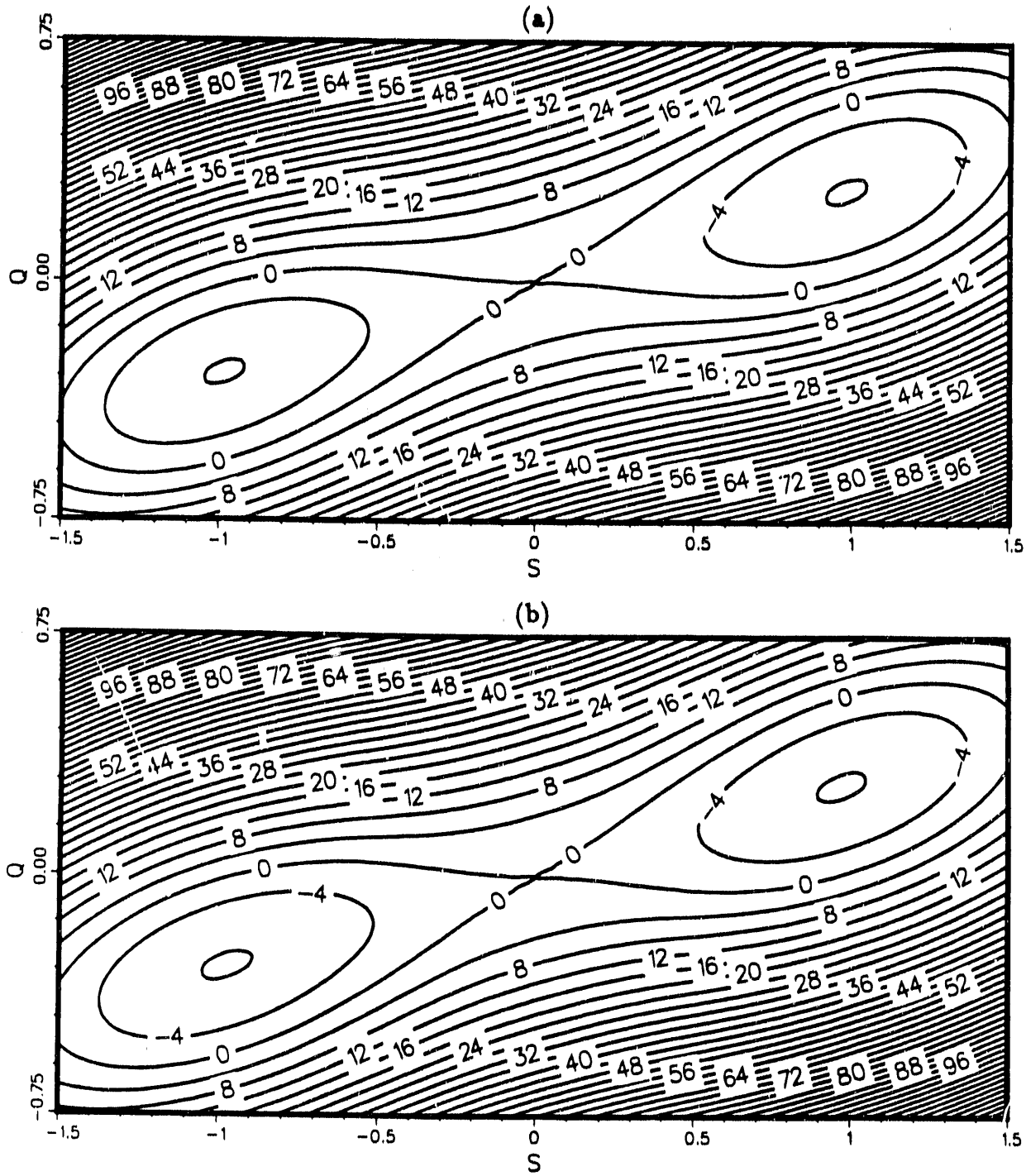

Figure 9: Same as Figure 7, but for odd (n=1) coupling with the constant c=0.01: (a) the original potential; (b) the EVB approximation (with harmonic diabatic potentials).

4 The H + H_2 → H_2 + H Collinear Reaction

Finally, this section shows that the EVB model is also applicable if the reactants and/or products are dissociative states. Application is made to the well-known H + H_2 → H_2 + H collinear potential energy surface for a demonstration.

Figure 10a shows a contour plot of the well-known LSTH[19] potential function for this reaction. Here the reactants and products are the asymptotic regions $r_1 \rightarrow \infty$ and $r_2 \rightarrow \infty$, respectively. Thus, the diabatic potential $V_{11}(r_1, r_2)$ in this case is

$$V_{11}(r_1, r_2) = v_{H_2}(r_2) + V_0(r_1), \tag{15.a}$$

where v_{H_2} is the diatomic potential function of the free H_2 molecule and $V_0(r_1)$ is a nonreactive "translational" distortion potential. For the present application we have taken

$$V_0(r_1) = V(r_1, r_0), \tag{16}$$

where V is the true LSTH potential function and r_0 is the equilibrium H_2 bond length. (We have found that $V_0(r_1)$ is well approximated by the functional form $V_0(r_1) = Ae^{-\alpha r_1^{1/4}}$.) The diabatic potential V_{22} is similarly given as

$$V_{22}(r_1, r_2) = v_{H_2}(r_1) + V_0(r_2). \tag{15.b}$$

Figure 10b shows the EVB potential that results with these diabatic potentials and the exchange potential constructed via Eqs.(9)-(10) to reproduce the transition-state region. One does see some quantitative differences between parts a and b of

Figure 10, but they are mostly in regions unimportant for the reaction. It would undoubtedly be possible to find diabatic potentials that would allow the EVB model to mimic the original potential more accurately; the point of this example, however, is to show that the EVB prescription of section 2 yields a reasonably accurate reactive potential surface even with the simplest, most obvious choice for the diabatic potentials.

5 Concluding Remarks

The object of this chapter has been to show that the EVB model, with the prescription described in section 2 for choosing the exchange potential V_{12} , provides a reasonable global approximation for reactive potential surfaces for a wide variety of situations. In many cases the model gives good results with the simplest possible choice for the diabatic potentials, namely, a harmonic normal-mode approximation about the reactant and product equilibrium positions. The results are improved, however, if anharmonicities are included in the diabatic potentials. This is presumably because in this case the diabatic potentials themselves describe the true potential over a wider region of space, so that the exchange potential is then required to describe matters in a more restricted region about the transition state.

The EVB model as put forth in this chapter can be readily applied to real polyatomic reactions. In the following chapter, this method will be proved to be successful for the construction of a 6 dimensional PES for the molecular dissociation reaction of formaldehyde.

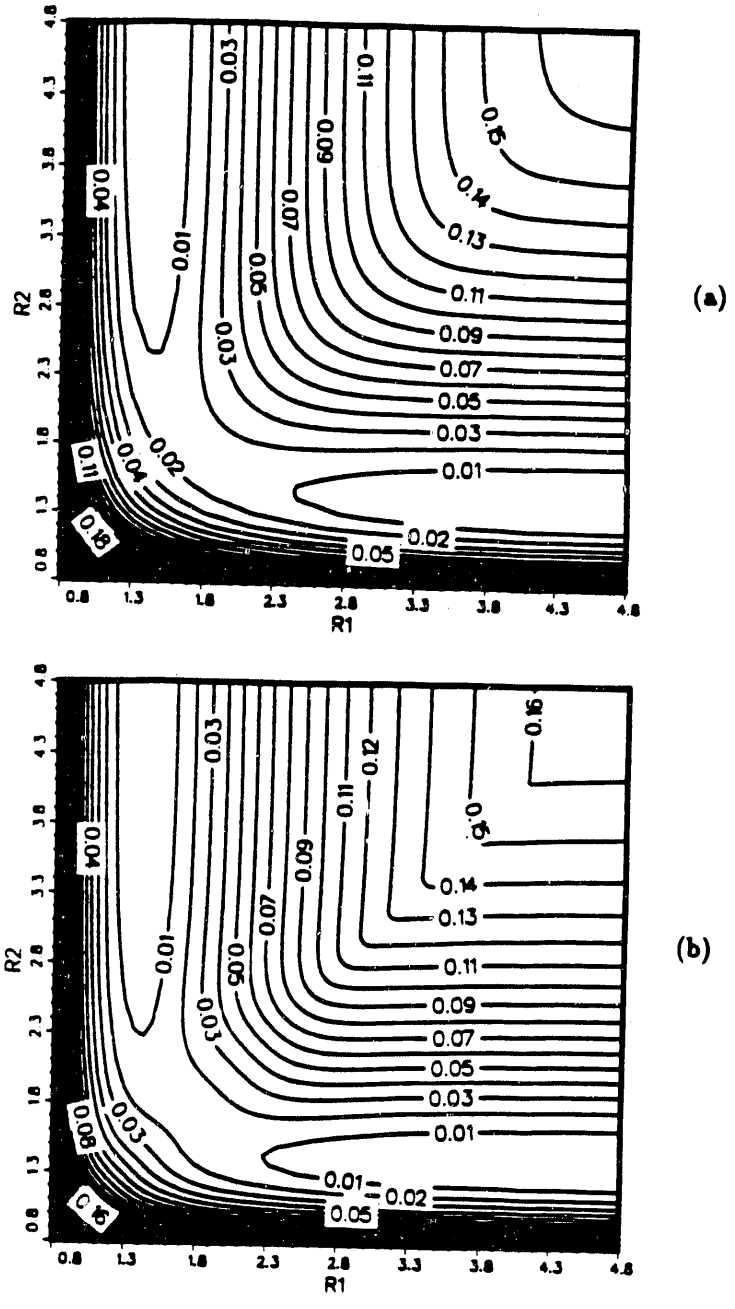

Figure 10: The LSTH potential energy surface for the collinear $H + H_2 \rightarrow H_2 + H$ reaction: (a) the original LSTH potential surface; (b) the EVB approximation, with the diabatic potentials of Eqs.(15)-(16). r_1, r_2 and the contour values are all in atomic units.

References

[1] Good overviews of the problem of representing potential energy surfaces are the reviews:
(a) D. G. Truhlar, R. Steckler, and M. S. Gordon, *Chem. Rev.* **87**, 217 (1987).
(b) G. C. Schatz, *Rev. Mod. Phys.* **61**, 669 (1989).

[2] See for example:
W. J. Hehre, L. Radom, P. v. R. Schleyer, and J. A. Pople, *Ab initio Molecular Orbital Theory*; Wiley: New York (1986).

[3] R. A. Markus, *J. Chem. Phys.* **49**, 2610 (1968).

[4] (a) W. H. Miller, N. C. Handy, and J. E. Adams, *J. Chem. Phys.* **72**, 788 (1980).
(b) W. H. Miller, *J. Phys. Chem.* **87**, 3811 (1983).

[5] K. Fukui, *Acc. Chem. Res.* **14**, 363 (1981).

[6] J. T. Hougen, P. R. Bunker, and J. W. C. Johns, *J. Mol. Spectrosc.* **34**, 136 (1970).

[7] (a) B. A. Ruf and W. H. Miller, *J. Chem. Soc., Faraday Trans. 2* **84**, 1523 (1988).
(b) W. H. Miller, B. A. Ruf, and Y.-T. Chang, *J. Chem. Phys.* **89**, 6298 (1988).

[8] (a) N. L. Allinger, *J. Am. Chem. Soc.* **99**, 8127 (1977).
(b) N. L. Allinger, Y. H. Yuh, and J.-H. Lii, *J. Am. Chem. Soc.* **111**, 8551 (1989).
(c) J.-H. Lii and N. L. Allinger, *J. Am. Chem. Soc.* **111**, 8566 (1989).
(d) J.-H. Lii and N. L. Allinger, *J. Am. Chem. Soc.* **111**, 8576 (1989).

[9] B. R. Brooks, R. E. Bruccoleri, B. D. Olafson, D. J. States, S. Swaminathan, and M. Karplus, *J. Comput. Chem.* **4**, 187 (1983).

[10] (a) P. K. Weiner and P. A. Kollman, *J. Comput. Chem.* **2**, 287 (1981).
(b) S. J. Weiner, P. A. Kollman, D. A. Case, U. C. Singh, C. Ghio, G. Alagona, S. Profeta Jr., and P. Weiner, *J. Am. Chem. Soc.* **106**, 765 (1984).
(c) S. J. Weiner, P. A. Kollman, D. T. Nguyen, and D. A. Case, *J. Comput. Chem.* **7**, 230 (1986).

[11] W. L. Jorgensen and J. Tirado-Rives, *J. Am. Chem. Soc.* **110**, 1657 (1988).

[12] (a) A. Warshel and S. Lifson, *J. Chem. Phys.* **49**, 5116 (1968).
(b) A. Warshel, in *Modern Theoretical Chemistry*; G. A. Segal, Ed.; Plenum: New York (1977); Vol. 7, p 133.

[13] (a) A. Warshel and R. M. Weiss, *J. Am. Chem. Soc.* **102**, 6218 (1980).
(b) A. Warshel, *Biochemistry* **20**, 3167 (1981).
(c) A. Warshel, *Acc. Chem. Res.* **14**, 284 (1981).

[14] A preliminary version of this work was presented at the NATO Advanced Study Institute on Computational Advances in Organic Chemistry, Altinoluk, Turkey, July 30–August 12, 1989.

[15] See, for example:
(a) T. F. George and J. Ross, *J. Chem. Phys.* **55**, 3851 (1971).
(b) G. C. Schatz and J. Ross, *J. Chem. Phys.* **66**, 1021, 1037, 2943 (1977).
(c) S. Mukamel and J. Ross, *J. Chem. Phys.* **66**, 3759 (1977).

[16] (a) J. W. Downing, J. Michl, J. Cizek, and J. Paldus, *Chem. Phys. Lett.* **67**, 377 (1979).
(b) J. W. Downing and J. Michl, In *Potential Energy Surfaces and Dynamics Calculations*; D. G. Truhlar, Ed.; Plenum: New York (1980); pp 199–212.

[17] See, for example:
R. Kubo, *J. Phys. Soc. Jpn.* **17**, 1100 (1962).

[18] N. Makri and W. H. Miller, *J. Chem. Phys.* **86**, 1451 (1987); **87**, 5781 (1987); **91**, 4026 (1989).

[19] (a) P. Siegbahn and B. Liu, *J. Chem. Phys.* **68**, 2457 (1978).
(b) D. G. Truhlar and C. J. Horowitz, *J. Chem. Phys.* **68**, 2466 (1978); **71**, 1514(E) (1979).

Chapter III
Potential and Dynamics of Formaldehyde

1 Introduction

Formaldehyde has been studied extensively during the past two decades. Its abundance and importance in the environment, such as in air pollution and in interstellar space, have stimulated macroscopic kinetic[1-3] and microscopic spectroscopic[4] studies of this molecule. Its small size and well resolved energy levels allow quantum-state specific experimental and theoretical studies of the reaction dynamics. The mechanism of the molecular dissociation of formaldehyde is well-known:[5] the electronically excited H_2CO (S_1) internally converts to highly vibrationally excited levels of the ground electronic state (S_0) which then undergo unimolecular decomposition,

$$\begin{aligned} H_2CO(S_0) + h\nu(280 - 355\text{nm}) &\rightarrow H_2CO(S_1, v, J, K_a, K_c) \\ &\rightarrow H_2CO(S_0^*) \rightarrow H_2(v,j) + CO(v,j). \end{aligned} \quad (1)$$

Stark level-crossing spectroscopy[6] studies of the 4^0 and 4^1 bands of D_2CO (S_1) has enabled the determination of the eigenstates of these highly excited vibrational levels. This in turn allows one to determine the distribution of the state-specific unimolecular decay rates, the S_1 and S_0^* internal conversion coupling, and the reaction barrier height. For H_2CO and D_2CO, the activation energies (with zero point energy correction) are estimated to be 79.2±0.8 kcal/mol and 80.6±0.8 kcal/mol,[6(c)] respectively.

Past measurement of the energy partitioning in the fragmentation products include the translational energy distribution from time-of-flight (TOF) molecular

beam experiment,[7] the *ortho* H_2(v,j) distributions[8] by coherent anti-Stokes Raman spectroscopy (CARS), and the CO(v,j) distributions[9] by laser-induced fluorescence (LIF). More recently, the technique of Doppler-resolved laser-induced fluorescence was used to study the H_2 translational and (v,j) distributions, the quantum state correlation[10] and the vector correlations.[11] These experiments have improved the understanding of the dissociation dynamics and the knowledge of some characteristics of the reaction coordinate and potential energy surface.

On the theoretical side, much effort has been spent on finding the properties of the stationary points[12–17] (i.e., the equilibrium state and the transition state) on the S_0, S_1 and T_1[18] surfaces and also on investigating the possibility of an intermediate state for the dissociation reaction. State-of-the-art *ab initio* quantum chemistry studies utilizing large basis sets and high level correlation methods such as multi-configuration self-consistent field (MCSCF),[14] Moller-Plesset perturbation theory[15,16] and coupled-cluster methods[17] have been performed. The predicted geometries, reaction barrier height, harmonic force constants and some of the anharmonicities[16(a)] agree quite well with experiments. Knowledge of the force constants and anharmonicities of the transition state region allows semiclassical calculations of the transition state tunneling probabilities.[19]

There is also some work concerning rotational excitation in the inelastic collision of H_2 + CO. Schinke and co-workers[20(a)] have used *ab initio* calculations combined with damped long range dispersion coefficients (from experimental and calculated cross sections) to obtain a rigid-rotor potential energy surface for the dissociative re$_e$. The infinite order sudden approximation (IOSA) was used to study the rotational state distributions of H_2 and CO molecules,[20(b–d)] and good agreement with experiment was obtained.

However, a complete theoretical study of the reaction which allows full comparisons with the experimental results (for instance, the product state distribution, the

vector correlations and the reaction rates) requires an accurate global potential energy surface (PES). Although it is possible to carry out selected *ab initio* quantum chemistry for certain regions of a four-atom system, the amount of work and CPU time necessary to determine the PES at all necessary geometries is prohibitive at the present time. Empirical or semi-empirical methods are the usual approaches for global PES's. In 1981, Carter and Handy[21] published an empirical surface with a many-body expansion formula:

$$V_{H_2CO} = 2V_{CH}^{(2)} + V_{HH}^{(2)} + V_{CO}^{(2)} + 2V_{OH}^{(2)}$$
$$+V_{CH_2}^{(3)} + 2V_{HCO}^{(3)} + V_{H_2O}^{(3)} + V_{H_2CO}^{(4)}. \qquad (2)$$

This surface can be used to study any possible fragmentation reaction of formaldehyde, for example, radical dissociation into H + HCO or molecular dissociation into H_2 + CO. Unfortunately, a classical trajectory study[10] using this surface did not yield correct results for the product state distributions of the molecular dissociation reaction.

Recently, we suggested an empirical valence bond model[22] for constructing global PES's for chemical reactions of polyatomic molecules. The idea is to combine useful information (either from experiments or *ab initio* studies) on different regions of the surface semi-empirically in order to obtain a 3N-6 full dimensional potential energy surface for the $H_2CO \rightarrow H_2$ + CO reaction. The validity of the surface is then tested through classical trajectory calculations of product state distributions and vector correlations. Secton 2 describes the construction of the potential surface, and the classical trajectory method is discussed briefly in section 3. Sections 4 and 5 present the product state distributions and vector correlations obtained from the trajectories and compare them with the experimental results. Section 6 concludes.

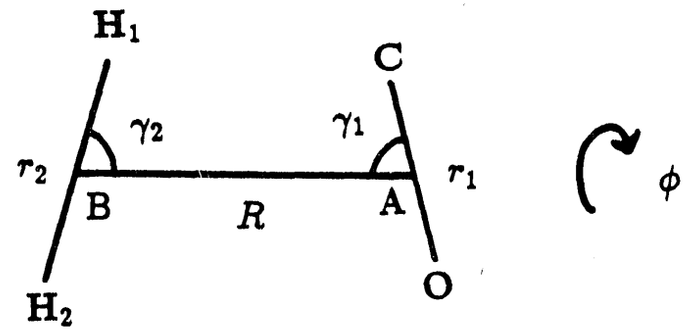

Figure 1: The 6 internal coordinates. A and B are dummy atoms representing the centers of mass of CO and H_2 molecules.

2 The Global Potential Surface

2.1 Coordinates

There are many different ways of choosing the coordinate system for constructing the global PES. Here we choose the Jacobi type internal coordinates which are obviously the right choice in the dissociation region. The 6 (i.e., 3N-6) internal coordinates $\mathbf{q} = (R, r_1, r_2, \gamma_1, \gamma_2, \phi)$ are illustrated in Figure 1.

The definitions of R, r_1 and r_2 should be transparent. γ_1 is defined as $\angle$CAB and γ_2 as $\angle H_1BA$ where A and B are the centers of mass of CO and H_2, respectively. ϕ is the out-of-plane torsional angle. To give rigorous expressions for these coordinates, let's start from the cartesians $\mathbf{x}$:

$$\mathbf{x} = (\vec{r}_c, \vec{r}_o, \vec{r}_{H_1}, \vec{r}_{H_2})$$

$$= (x_c, y_c, z_c, x_o, y_o, z_o, x_{H_1}, y_{H_1}, z_{H_1}, x_{H_2}, y_{H_2}, z_{H_2}). \tag{3a}$$

Define

$$\mathbf{X} = \left(\vec{R}, \vec{r}_1, \vec{r}_2\right), \tag{3b}$$

where

$$\vec{r}_1 = \vec{r}_c - \vec{r}_o = (x_1, y_1, z_1),$$

$$\vec{r}_2 = \vec{r}_{H_1} - \vec{r}_{H_2} = (x_2, y_2, z_2),$$

$$\vec{R} = \frac{m_{H_1}\vec{r}_{H_1} + m_{H_2}\vec{r}_{H_2}}{m_{H_1} + m_{H_2}} - \frac{m_c\vec{r}_c + m_o\vec{r}_o}{m_c + m_o} = (X, Y, Z). \tag{3c}$$

The relationships between **X** and **q** are:

$$R = \sqrt{X^2 + Y^2 + Z^2},$$

$$r_1 = \sqrt{{x_1}^2 + {y_1}^2 + {z_1}^2},$$

$$r_2 = \sqrt{{x_2}^2 + {y_2}^2 + {z_2}^2},$$

$$\gamma_1 = \cos^{-1}\left[\frac{\vec{R}\cdot\vec{r}_1}{Rr_1}\right],$$

$$\gamma_2 = \pi - \cos^{-1}\left[\frac{\vec{R}\cdot\vec{r}_2}{Rr_2}\right],$$

$$\phi = \cos^{-1}\left[\frac{R^2(\vec{r}_1\cdot\vec{r}_2) - \left(\vec{R}\cdot\vec{r}_1\right)\left(\vec{R}\cdot\vec{r}_2\right)}{\sqrt{R^2{r_1}^2 - \left(\vec{R}\cdot\vec{r}_1\right)^2}\sqrt{R^2{r_2}^2 - \left(\vec{R}\cdot\vec{r}_2\right)^2}}\right]. \tag{4}$$

2.2 Transformation of the Force Constant Matrix

One of the important requirements of a good PES is to reproduce the correct geometries and the harmonic frequencies (and anharmonicity, if it is necessary) at the stationary points, i.e., equilibrium and transition state for the reaction. *Ab initio*

quantum chemistry is capable of finding these quantities with many state-of-the-art techniques. To obtain the harmonic frequencies, calculation of the second derivatives of the potential by analytical or numerical methods has become a common routine in quantum chemistry. The results of the second derivative matrices are normally represented in the 3N cartesians or the valence-bond type internal coordinates. Since the coordinates we use for our PES is the Jacobi type internal coordinates, transformations of the geometries and force constant matrices (which are required for our EVB model) are inevitable.

Although the transformaton of the geometries is trivial (through Eq.(4)), that of the derivatives (of any order) of the potential is more tedious. Here we describe two different approaches of transforming the second derivatives.

2.2.1 Method A

(a) Let **B** (3N-6 by 3N-3) be the transformation matrix[23] which relates the displacements in **q** and **X**, and **B**′ (3N-3 by 3N) be the transformation matrix between **X** and **x**,

$$d\mathbf{q} = \mathbf{B} \cdot d\mathbf{X} = \mathbf{B} \cdot \mathbf{B}' \cdot d\mathbf{x} = \mathbf{C} \cdot d\mathbf{x}. \tag{5a}$$

(b) At the stationary points of the PES, the potential can be approximated by

$$2(V - V_0) = d\mathbf{x}^T \cdot \mathbf{K} \cdot \mathbf{x} = d\mathbf{q}^T \cdot \left(\mathbf{C}^T\right)^{-1} \cdot \mathbf{K} \cdot \mathbf{C}^{-1} \cdot d\mathbf{q}, \tag{5b}$$

where **K** is the cartesian force constant matrix.

(c) The force constant matrix **F** in **q** is obtained through

$$\mathbf{F} = \left(\mathbf{C}^T\right)^{-1} \cdot \mathbf{K} \cdot \mathbf{C}^{-1}. \tag{5c}$$

This method is quite straightforward except that there exists infinite sets of the inverse of **C** (3N-6 by 3N) and $\mathbf{C}^T$(3N by 3N-6). This is a consequence of the

non-uniqueness of the transformation from internal coordinates to cartesians. To preserve the center of mass and the orientation of the molecule upon a displacement dq, the following approach is recommended for the inversions:[24]

$$\left(\mathbf{C}^T\right)^{-1} = \left(\mathbf{C}\cdot\mathbf{M}\cdot\mathbf{C}^T\right)^{-1}\cdot\mathbf{C}\cdot\mathbf{M},$$

$$\mathbf{C}^{-1} = \left[\left(\mathbf{C}^T\right)^{-1}\right]^T, \tag{6}$$

where $\mathbf{M} = \mathbf{m}^{-1}$, and $\mathbf{m}$ is a diagonal matrix (with dimensions 3N by 3N) consisting the atomic masses.

The non-zero matrix elements of $\mathbf{B}$ and $\mathbf{B}'$ are shown in Appendix A at the end of this chapter.

2.2.2 Method B

(a) The normal mode coordinates $\mathbf{Q}$ are related to internal coordinates $\mathbf{q}$ through the following:

$$d\mathbf{q} = \mathbf{L}\cdot d\mathbf{Q}. \tag{7a}$$

(b) Let $\mathbf{L_x}$ be the eigenvector matrix of the mass-weighted cartesian force constant matrix, and Λ a diagonal matrix containing the corresponding eigenvalues. It is not difficult to show that $\mathbf{L}$ can be expressed as

$$\mathbf{L} = \mathbf{C}\cdot\mathbf{m}^{-1/2}\cdot\mathbf{L_x}. \tag{7b}$$

(c) Since $d\mathbf{q}^T\cdot\mathbf{F}\cdot d\mathbf{q} = d\mathbf{Q}^T\cdot\Lambda\cdot d\mathbf{Q}$, one gets

$$\mathbf{F} = \left(\mathbf{L}^T\right)^{-1}\cdot\Lambda\cdot\mathbf{L}^{-1}. \tag{7c}$$

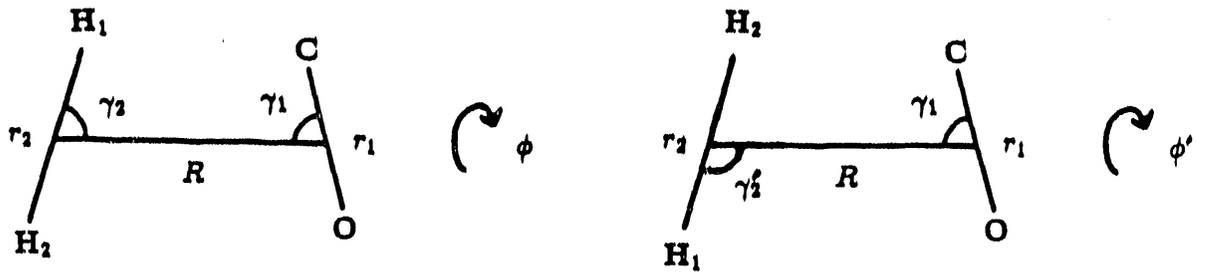

Figure 2: Two configurations with the same potential energy but different labelings on the hydrogen atoms. ($\gamma_2' = \pi - \gamma_2, \phi' = \pi + \phi$)

2.3 Symmetry of the Potential Surface

Before we construct the PES, there is another important property one should be aware of. That is, the symmetry of the potential upon exchange of the two hydrogen atoms. The potential energy stays the same when $(\gamma_2, \phi) \rightarrow (\pi - \gamma_2, \pi + \phi)$ as illustrated in Figure 2.

An appropriate analytic form of the PES using the above coordinates is

$$V(R, r_1, r_2, \gamma_1, \gamma_2, \phi) = \sum_{l_1, l_2, m>0} V_{l_1 l_2 m}(R, r_1, r_2) Y_{l_1 m}(\gamma_1, 0) Y_{l_2 m}(\gamma_2, 0) \cos m\phi. \quad (8a)$$

Since

$$V(\gamma_2, \phi) = V(\pi - \gamma_2, \pi + \phi)$$

$$= (-1)^{l_2+m}(-1)^m V(\gamma_2, \phi) = (-1)^{l_2} V(\gamma_2, \phi), \quad (8b)$$

l_2 is restricted to be an even number.

In the next section, we construct the global PES which bears the above symmetry property.

2.4 The Empirical Valence Bond Approach

A schematic one dimensional curve is plotted in Figure 3 to represent the ground electronic PES of formaldehyde. The location of the equilibrium configuration ($\mathbf{q}^{eq}$) is at the middle of the curve. There exist two transition state configurations with the same energy, and same geometry but different molecular orientations (corresponding to exchanging the two hydrogen atoms). The tails of the PES represent the dissociative region H_2 + CO.

Let $V_{11}(\mathbf{q})$, $V_{22}(\mathbf{q})$ and $V_{33}(\mathbf{q})$ be the diabatic global PES's. The exchange potential between V_{11} and V_{33} is represented by $V_{13}(\mathbf{q})$, and that between V_{22} and V_{33} is represented by $V_{23}(\mathbf{q})$. Because of the symmetry built into V_{11} and V_{22}, they are the same for all geometries. That is,

$$V_{11}(\mathbf{q}) = V_{22}(\mathbf{q}). \tag{9}$$

The secular equation which determines the adiabatic (i.e., Born-Oppenheimer) PES is

$$\begin{vmatrix} V_{11} - \Lambda & 0 & V_{13} \\ 0 & V_{22} - \Lambda & V_{23} \\ V_{13} & V_{23} & V_{33} - \Lambda \end{vmatrix} = 0, \tag{10a}$$

with the lowest root being the desired adiabatic ground state PES $V(\mathbf{q})$. It is found to have a very simple form:

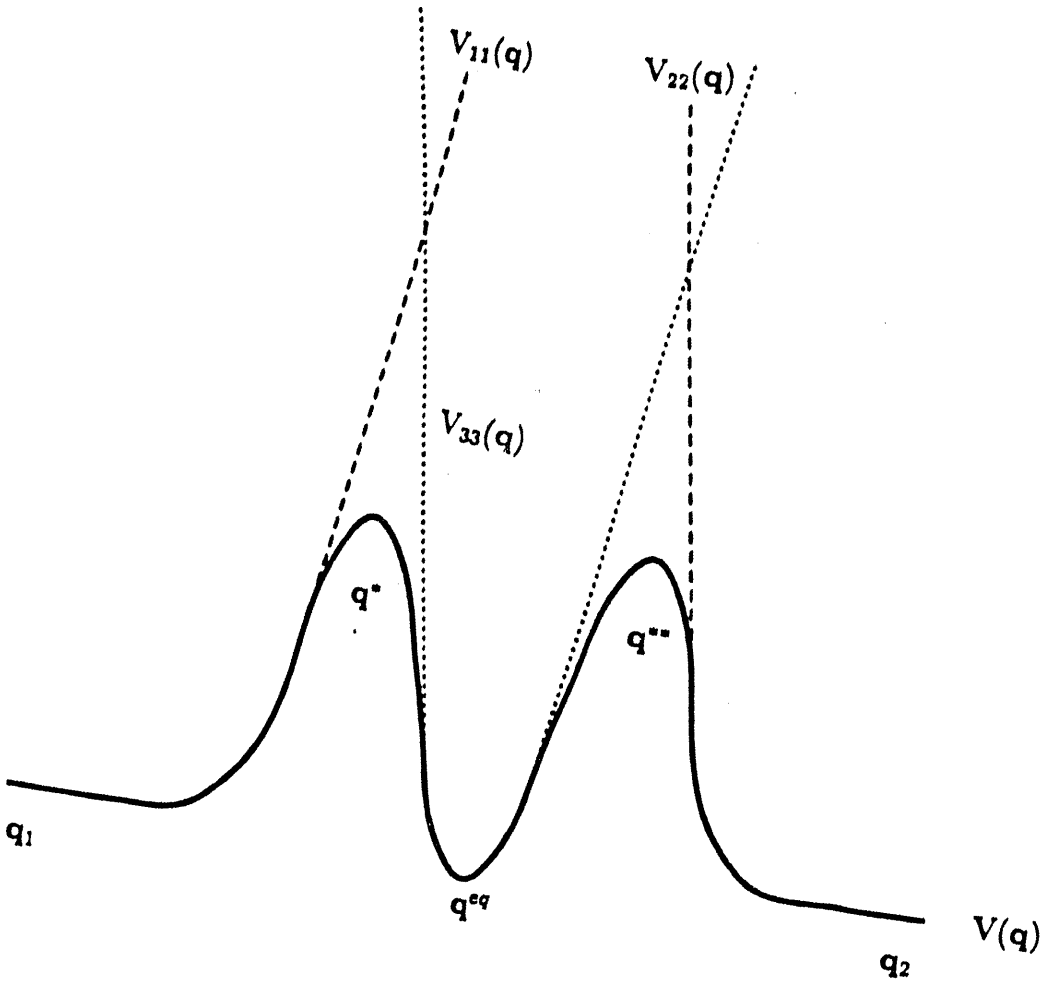

Figure 3: A schematic one dimensional diagram representing the global potential energy surface for the $H_2CO \rightarrow H_2 + CO$ reaction. q^{eq} is the equilibrium configuration. The two transition state configurations are represented by q^* and q^{**}, respectively. q_1 and q_2 are for the dissociative products' configurations. Dashed curves represent the diabatic potential $V_{11}(q)$ and $V_{22}(q)$, and dotted curve for $V_{33}(q)$. The adiabatic potential energy surfaces $V(q)$ is represented with solid line.

$$\Lambda = V(\mathbf{q}) = \frac{1}{2}(V_{11}(\mathbf{q}) + V_{33}(\mathbf{q})) - \left[\left(\frac{V_{11}(\mathbf{q}) - V_{33}(\mathbf{q})}{2}\right)^2 + V_{13}(\mathbf{q})^2 + V_{23}(\mathbf{q})^2\right]^{\frac{1}{2}}. \quad (10b)$$

The explicit expressions that we use for each term in Eq.(10b) are described in the following subsections.

2.4.1 $V_{11}(\mathbf{q})$

The three dimensional rigid-rotor (with the bond distances of CO and H_2 fixed at their equilibrium values) PES from Schinke and co-workers[20(a)] is used. The functional form of their potential is simply the expansions in terms of the Legendre polynomials,

$$V(R, \gamma_1, \gamma_2) = \sum_{l_1, l_2} V_{l_1 l_2}(R) P_{l_1}(\cos\gamma_1) P_{l_2}(\cos\gamma_2), \quad (11)$$

with l_1 = 0,1,...,8 and l_2=0 and 2. They only included l_2 up to 2 because the potential around H_2 molecule is quite spherical. There is no dependence on the out-of-plane torsional angle ϕ in the expression because the potential is not sensitive to variation of ϕ. Therefore, results from different ϕ's have been averaged over.

A simple way for obtaining our diabatic potential $V_{11}(\mathbf{q})$ is to add functional forms which depend on CO and H_2 bond distances in addition to Schinke's rigid-rotor PES. Therefore, we have included the vibrational potential energy curves of CO and H_2.[21] Our final expression is as follows:

$$V_{11}(\mathbf{q}) = \sum_{l_1, l_2} V_{l_1 l_2}(R) P_{l_1}(\cos\gamma_1) P_{l_2}(\cos\gamma_2) + v_{co}(r_1) + v_{H_2}(r_2), \quad (12)$$

where $v_{co}(r_1)$ and $v_{H_2}(r_2)$ have the same functional form:

$$v(r) = -D_e \left[1 + a_1(r - r_0) + a_2(r - r_0)^2 + a_3(r - r_0)^3\right] \exp\left[-a_1(r - r_0)\right]. \quad (13)$$

The coefficients in Eq.(13) for CO and H_2 are listed in Table I.

2.4.2 $V_{33}(\mathbf{q})$

With *ab initio* quantum chemistry, the second derivatives about the potential minimum are readily obtained and provide a harmonic potential around the equilibrium configuration. The functional form for $V_{33}(\mathbf{q})$ is same as Eq.(8a). Terms beyond quadratic order expansion have been truncated. $V_{l_1 l_2 m}$'s become constant except $V_{000}(R, r_1, r_2)$.

$$V_{33}(\mathbf{q}) = V_{000}(R, r_1, r_2) + V_{100}\cos\gamma_1 + V_{020}\cos^2\gamma_2$$
$$+V_{121}\sin\gamma_1\cos\gamma_2\sin\gamma_2\cos\phi + V_{222}\sin^2\gamma_1\sin^2\gamma_2\cos 2\phi, \quad (14)$$

where

$$2V_{000}(R, r_1, r_2) = F_{RR}(R - R^{eq})^2 + F_{r_1 r_1}(r_1 - r_1^{eq})^2 + F_{r_2 r_2}(r_2 - r_2^{eq})^2$$
$$+F_{Rr_1}(R - R^{eq})(r_1 - r_1^{eq}) + F_{Rr_2}(R - R^{eq})(r_2 - r_2^{eq}) + F_{r_1 r_2}(r_1 - r_1^{eq})(r_2 - r_2^{eq}), \quad (15a)$$

and

$$V_{100} = -\frac{1}{2}(F_{\gamma_1\gamma_1} + F_{\phi\phi}),$$
$$V_{020} = \frac{1}{2}F_{\gamma_2\gamma_2},$$
$$V_{121} = -F_{\gamma_1\gamma_2},$$
$$V_{222} = \frac{1}{4}(F_{\gamma_1\gamma_1} - F_{\phi\phi}). \quad (15b)$$

The F's are the equilibrium configuration force constants in Jabobi type internal coordinates which can be obtained through transformation from cartesian force constant matrix as described in section 2.2.

2.4.3 $V_{13}(\mathbf{q})$ and $V_{23}(\mathbf{q})$

The exchange potentials $V_{13}(\mathbf{q})$ and $V_{23}(\mathbf{q})$ are obtained as described in Chapter II. $\mathbf{q}^*$ and $\mathbf{q}^{**}$ represent the two transition state configurations. Vectors $\mathbf{b}_1$, $\mathbf{b}_2$ and matrices $\mathbf{c}_1$, $\mathbf{c}_2$ are constructed as before if the harmonic force fields around the two transition states and the functional forms of the diabatic potentials $V_{11}(\mathbf{q})$ and $V_{33}(\mathbf{q})$ are known. Higher order terms can be added if information on the anharmonicities (i.e., cubic and/or quartic force field) is available.

$$V_{13}(\mathbf{q}) = a \exp\left[\mathbf{b}_1 \cdot (\mathbf{q}-\mathbf{q}^*) - \frac{1}{2}(\mathbf{q}-\mathbf{q}^*)^T \cdot \mathbf{c}_1 \cdot (\mathbf{q}-\mathbf{q}^*) + \text{higher order term}\right]$$

$$V_{23}(\mathbf{q}) = a \exp\left[\mathbf{b}_2 \cdot (\mathbf{q}-\mathbf{q}^{**}) - \frac{1}{2}(\mathbf{q}-\mathbf{q}^{**})^T \cdot \mathbf{c}_2 \cdot (\mathbf{q}-\mathbf{q}^{**}) + \text{higher order term}\right]. \tag{16}$$

Care has to be taken to ensure the proper asymptotic behaviour of the exchange potentials. That is,

$$V_{13}(\mathbf{q}) \to 0 \qquad \text{as} \qquad \mathbf{q} \to \mathbf{q}_1, \quad \mathbf{q}^{**} \quad \text{or} \quad \mathbf{q}^{eq},$$

and

$$V_{23}(\mathbf{q}) \to 0 \qquad \text{as} \qquad \mathbf{q} \to \mathbf{q}_2, \quad \mathbf{q}^{*} \quad \text{or} \quad \mathbf{q}^{eq}.$$

2.4.4 Geometries, Harmonic Frequencies and Energetics

There are quite a few reports from high level *ab initio* quantum chemistry calculations[12-17] concerning the potential surface around the equilibrium and transition state config-

urations of formaldehyde. Table II list the total energies and reaction barriers from some of the reports and experimental observations.

The results of the geometries and harmonic force fields obtained from CCSD/TZ2P and MP2/DZP are used independently to construct two global PES's. The original cartesian data were transformed to be in Jacobi type internal coordinates. Table III gives the geometries of the equilibrium and the two transition states obtained from both CCSD/TZ2P and MP2/DZP. The C–O distance at the transition state is predicted to be longer in the MP2/DZP than in the CCSD/TZ2P. An opposite trend is predicted for the H–H distance.

The force constant matrices of the three configurations, which are required for obtaining $\mathbf{b}_1$, $\mathbf{b}_2$, $\mathbf{c}_1$ and $\mathbf{c}_2$, are shown in Tables IV, V, and VI. One can check the accuracy of these transformed force constants by using them to find the harmonic frequencies. The first step is to calculate the corresponding G-matrix through

$$\mathbf{G} = \mathbf{C} \cdot \mathbf{M} \cdot \mathbf{C}^T, \tag{17}$$

where $\mathbf{M} = \mathbf{m}^{-1}$ and $\mathbf{C} = \mathbf{B} \cdot \mathbf{B}'$.

The analytical expressions of the matrix elements of the G-matrix are listed in Appendix B. The eigenvectors and eigenvalues of the well-known Wilson's GF matrix[23(a)] is obtained with an algorithm (due to Miyazawa[23(c)]) described in ref.23(b). Table VII shows the result of the six normal modes at the CCSD/TZ2P and the MP2/DZP transition state configurations and Figure 4 gives the schematic diagrams of these vectors.

The potential bare barrier heights (for $H_2CO \rightarrow H_2CO^*$) predicted by CCSD/TZ2P (90.4 kcal/mol) and MP2/DZP (94.7 kcal/mol) methods are both higher than the commonly accepted values ($\approx$ 86 kcal/mol), we have adjusted the energies of each configuration in order to obtain a reasonable value of the barrier. With the zero of

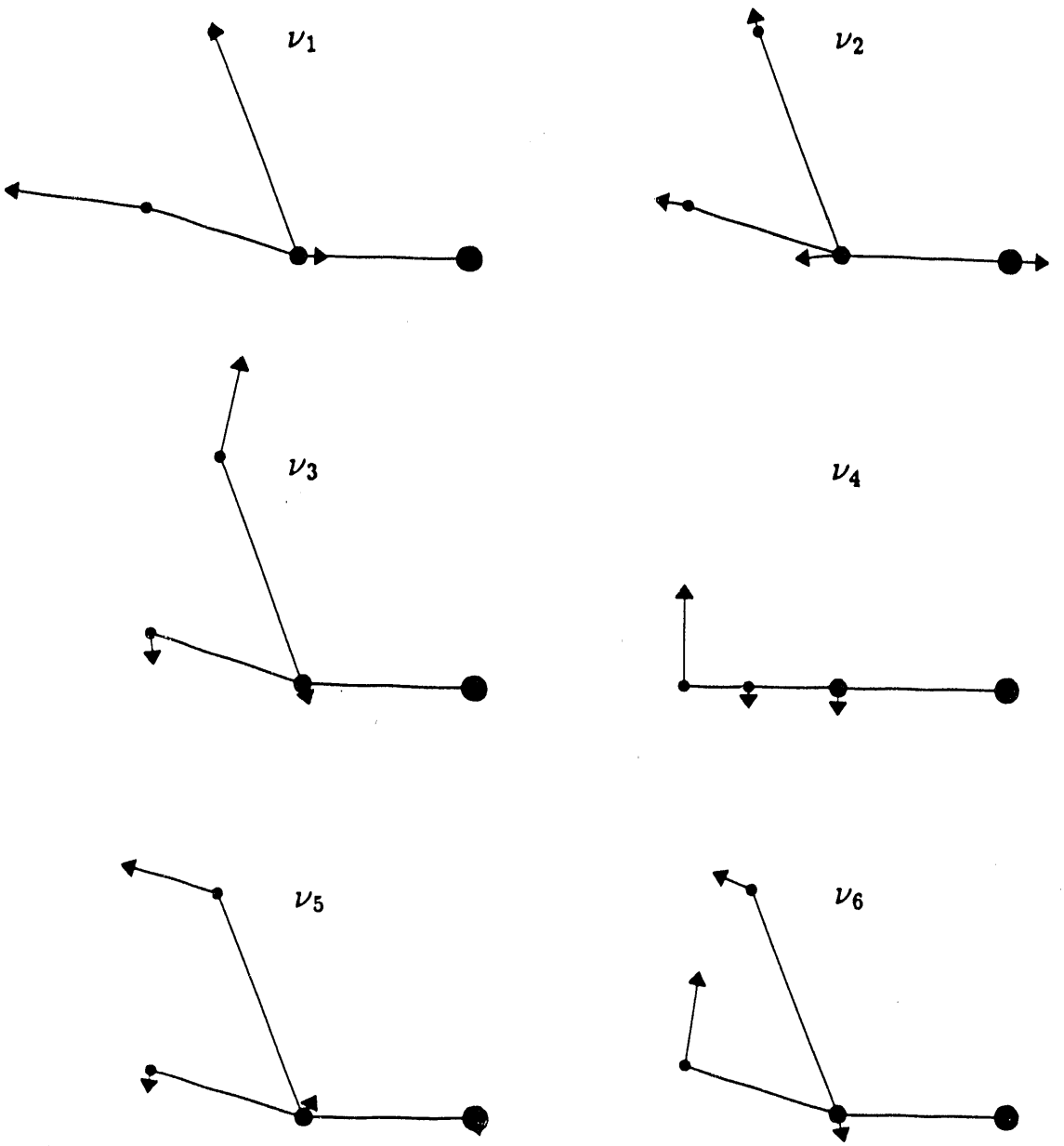

Figure 4: The normal modes of the CCSD/TZ2P optimized transition state geometry for the $H_2CO \rightarrow H_2 + CO$ reaction. The atoms are represented by solid circles of different sizes, i.e., O>C>H. Motions of C and O are exaggerated by a factor of 2. The reaction coordinate is ν_6. ν_4 is an out-of-plane bending mode. The frequencies of each modes are ν_1: 3145.3, ν_2: 1880.6, ν_3: 1359.0, ν_4: 878.3, ν_5: 811.7 and ν_6: 1935i cm^{-1}.

energy defined as:

$$V(\mathbf{q}) = 0 \qquad \text{if} \qquad R = \infty, \quad r_1 = 2.132\text{a.u.}, \quad r_2 = 1.40\text{a.u.},$$

and the potential energies at the equilibrium and transition state configurations as:

$$V(\mathbf{q} = \mathbf{q}^{eq}) = -0.0083\text{a.u.},$$

$$V(\mathbf{q} = \mathbf{q}^{*}) = V(\mathbf{q} = \mathbf{q}^{**}) = 0.13\text{a.u.},$$

the classical reaction barrier is found to be 86.8 Kcal/mol. The heat of reaction without zero point correction for $H_2CO \rightarrow H_2 + CO$ is chosen to be the same as the experimental result (5.2 kcal/mol).[17]

For the convenience of later discussions, these two global PES's are referred as CCSD PES and MP2 PES, although only part of the regions of the surfaces contain informations from these two *ab initio* methods. It is impossible to show the entire six dimensional potential energy surface on two dimensional paper. In Figure 5, we present a few two-dimensional cuts of the adiabatic CCSD PES around the transition state regions with all coordinates fixed at their transition state vaules except the two degrees of freedom chosen for the plot. Figure 6 shows those from the MP2 PES.

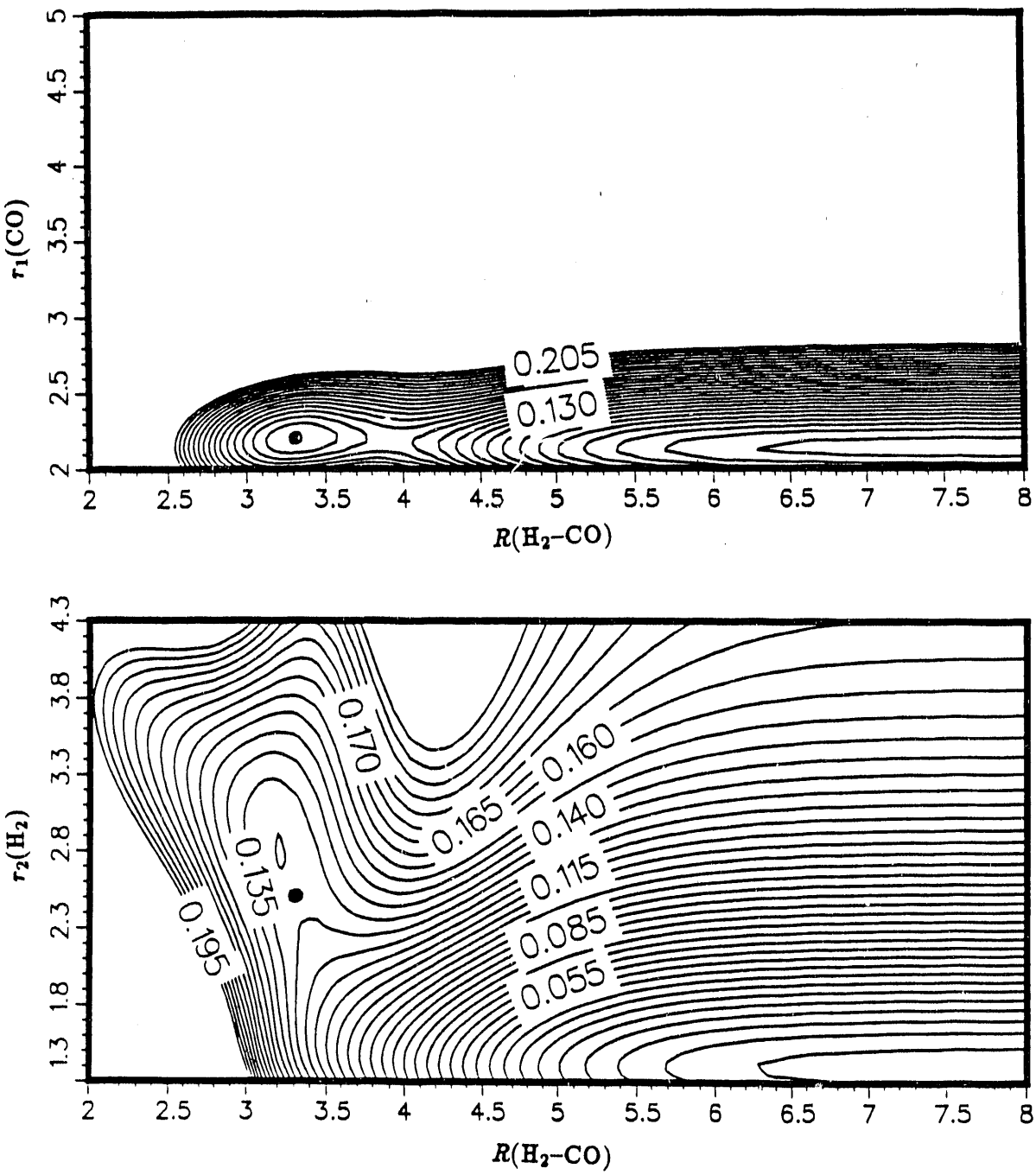

Figure 5: Two-dimensional cuts of the CCSD PES around the transition state. All coordinates are fixed at their transition state values except those two chosen for the plot. Bond distrances are in bohr, angles in degree and potential energy in hartree. Location of the transition state is indicated by the dot. The spacing between contour lines is 0.005 hartree.

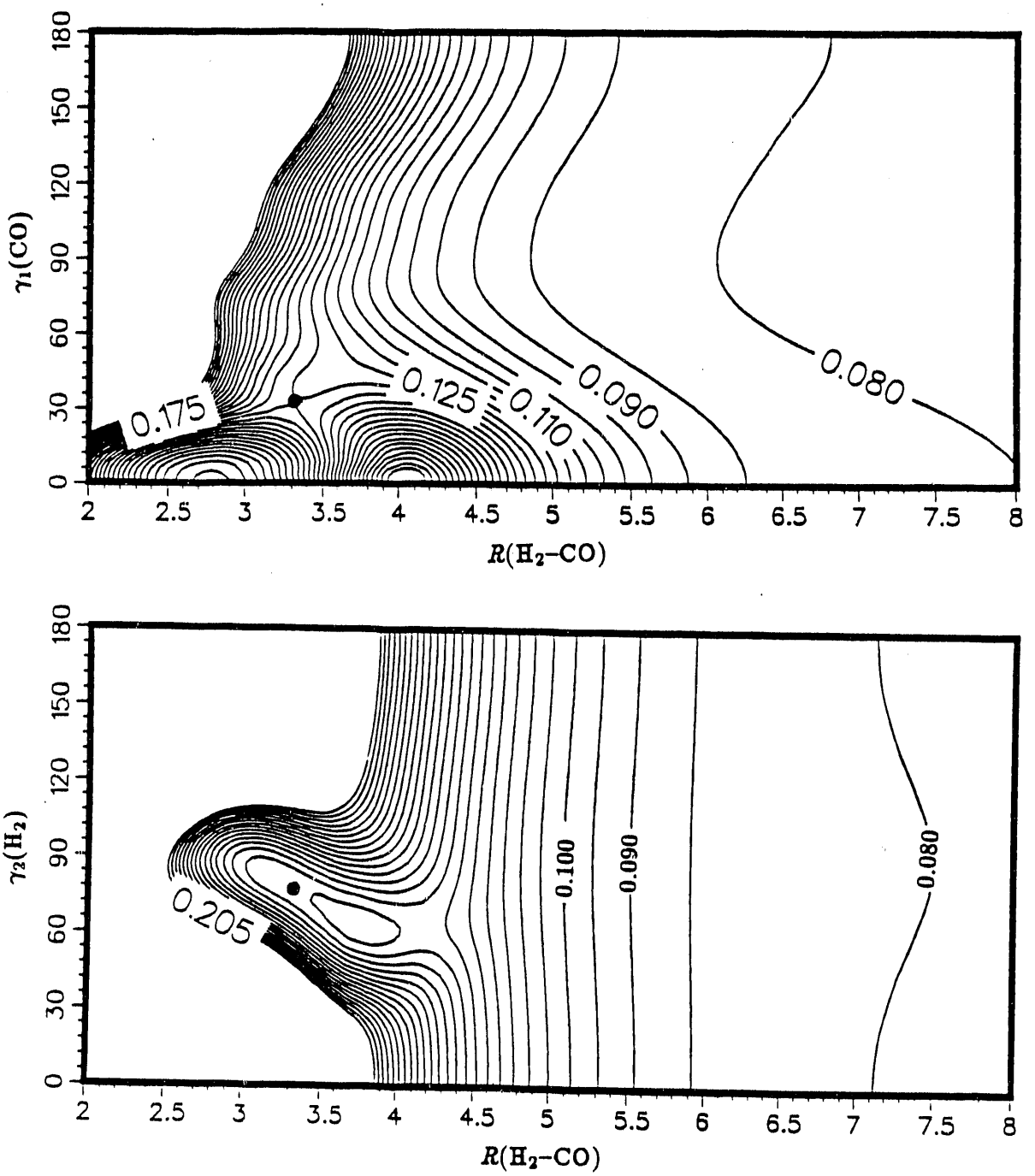

Figure 5, CCSD PES continued.

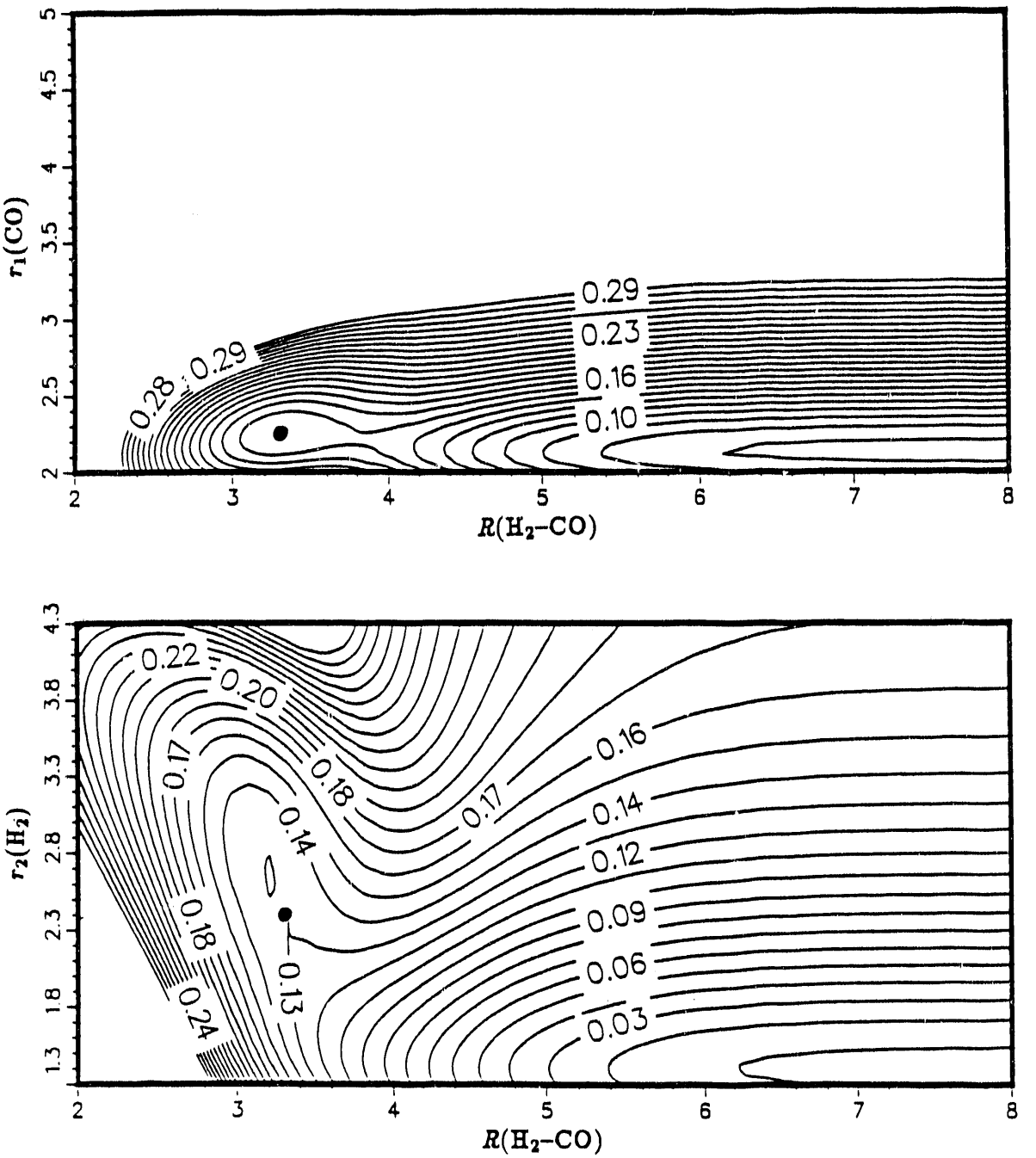

Figure 6: Same as Figure 5, except these are 2D cuts of the MP2 PES. Spacing between contour lines is 0.01 hartree.

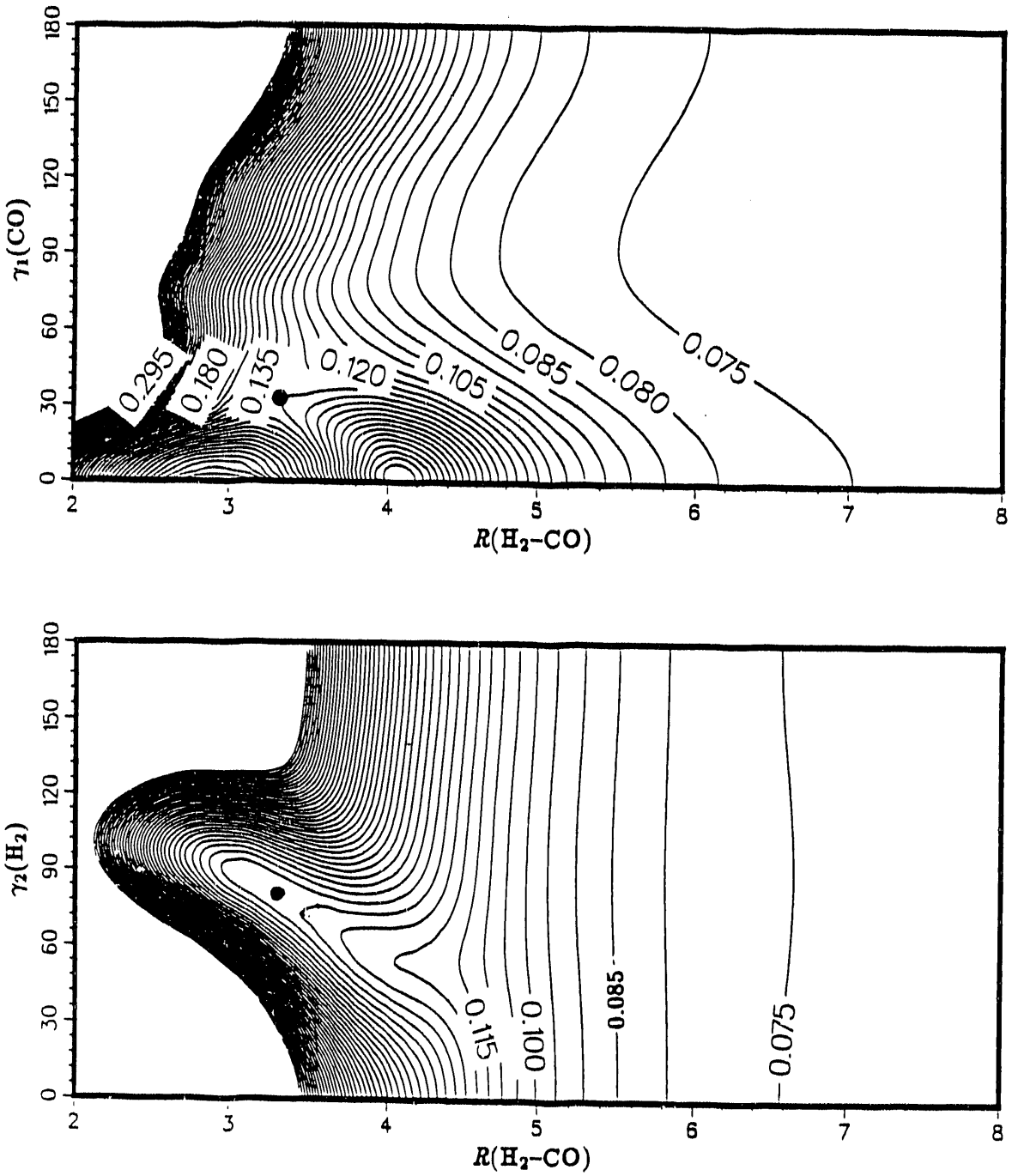

Figure 6, MP2 PES continued. Same as figure 5. Spacing between contour lines is 0.005 hartree.

3 Classical Trajectory Calculation

With the global potential energy surface, one can use classical trajectory calculations to study the reaction dynamics. Since the EVB model gives an analytical expression for the PES, calculation of the first derivatives is a simple task. The Hamiltonian appropriate for a dissociative process should include all degrees of freedom, for example,

$$H = \frac{1}{2m_c}(p_{x_c}^2 + p_{y_c}^2 + p_{z_c}^2) + \frac{1}{2m_o}(p_{x_o}^2 + p_{y_o}^2 + p_{z_o}^2)$$
$$+\frac{1}{2m_{H_1}}(p_{x_{H_1}}^2 + p_{y_{H_1}}^2 + p_{z_{H_1}}^2) + \frac{1}{2m_{H_2}}(p_{x_{H_2}}^2 + p_{y_{H_2}}^2 + p_{z_{H_2}}^2) + V(R, r_1, r_2, \gamma_1, \gamma_2, \phi). \quad (18)$$

However, without external force, there should be no overall translations. In this case, one can furthur reduce the Hamiltonian from 3N to 3N-3 degrees of freedom. The Jacobi coordinates defined in section 2 are most suitable for our calculations,

$$\mathbf{X} = (X, Y, Z, x_1, y_1, z_1, x_2, y_2, z_2).$$

The corresponding Hamiltonian and the equations of motion are

$$H = \frac{1}{2\mu}(P_X^2 + P_Y^2 + P_Z^2) + \frac{1}{2\mu_1}(P_{x_1}^2 + P_{y_1}^2 + P_{z_1}^2)$$
$$+\frac{1}{2\mu_2}(P_{x_2}^2 + P_{y_2}^2 + P_{z_2}^2) + V(R, r_1, r_2, \gamma_1, \gamma_2, \phi), \quad (19a)$$

$$\dot{X}_i = \frac{\partial H}{\partial P_i}, \quad (19b)$$

$$\dot{P}_i = -\frac{\partial H}{\partial X_i} = -\frac{\partial V}{\partial X_i} = -\sum_j \frac{\partial V}{\partial q_j}\frac{\partial q_j}{\partial X_i} = -\sum_j \frac{\partial V}{\partial q_j} \cdot \mathrm{B}_{ji}, \quad (19c)$$

where

$$\mu = \frac{(m_c + m_o)(m_{H_1} + m_{H_2})}{m_c + m_o + m_{H_1} + m_{H_2}},$$

$$\mu_1 = \frac{m_c m_o}{m_c + m_o},$$

$$\mu_2 = \frac{m_{H_1} m_{H_2}}{m_{H_1} + m_{H_2}}. \qquad (19d)$$

3.1 Initial Conditions

In the experiments, formaldehyde is excited from the ground electronic state (S_0) to a specific rovibrational state (v,J,K_a,K_c) near the origin of the S_1 surface. Usually, the 4^n and 2^m4^n bands[7-10] of the S_1 surface are probed. For example, a frequency around 29,500 cm^{-1} of the UV pulse excites a group of lines in the 2^14^1 band.

We mimic the experiments by choosing the total energy to be close to the experimental values. The total energy is set to be 0.153 a.u. (= 96 kcal/mol = 33,580 cm^{-1}) with the zero of energy defined previously. The excitation frequency and the total available energy (total energy - zero point energies of CO and H_2) are calculated and found to be close to the experimental ones. In the following, we describe how we choose the initial conditions for a given parent total angular momentum J.

3.1.1 For Total Angular Momentum J ~ 0

If the anharmonicity and rotation-vibration couplings around the transition state are weak, partitioning energy into the six normal modes should make the the total angular momentum to be near zero. So, the strategy is as follows:

(a) Diagonalize the force constant matrix at the transition state to find the normal modes (Q) and the harmonic frequencies.

(b) Use random number generator to pick the initial coordinates and momenta of the 5 normal modes which are orthogonal to the reaction coordinate such that

$$P_i^2 + \nu_i^2 Q_i^2 = \hbar\nu_i. \tag{20}$$

(c) Let $Q_{reaction} = Q_6 = 0$

(d) Extra energy (total energy - V - kinetic energy) is put into the momentum along the reaction coordinate.

(e) Transform the coordinates and momenta from normal modes into the cartesians.

(f) Find the initial total angular momentum by

$$| \mathbf{X} \times \mathbf{P} | = [J(J+1)]^{\frac{1}{2}}\hbar, \tag{21}$$

and assign J to the nearest integer.

(g) Start the trajectory.

With the above total energy, about 50% of the trajectories are found to have J=1, the other half of the trajectories are split between J=0 and J=2. Obviously, this strategy does not give a completely well defined initial rotational state. Effort can be made to find a different way of choosing the initial conditions so that all of the trajecotries have the same J and K_a, but we feel that the current approach is reasonable if the product state distributions do not depend too strongly on J and K_a, and it has the great virtue of simplicity.

3.1.2 For Higher Total Angular Momentum

(a) Find the coordiantes and momenta in cartesians as for the case J=0.

(b) Find the three principal moments of inertia I_a, I_b and I_c[25] of the transition state geometry.

(c) Randomly choose the three angular velocities ω_a, ω_b and ω_c such that

$$J(J+1)\hbar = M^2 = (I_a\omega_a)^2 + (I_b\omega_b)^2 + (I_c\omega_c)^2. \quad (22a)$$

(d) Find the extra velocity of each atom from the rotations about the three principal axes.

$$(\vec{v}_{rot})_{atom} = \vec{\omega} \times \vec{x}_{atom}. \quad (22b)$$

(e) The total velocity of each atom is the sum of velocities from vibrational and rotational motion.

$$\vec{v}_{atom} = (\vec{v}_{vib})_{atom} + (\vec{v}_{rot})_{atom}. \quad (22c)$$

Then the corresponding momenta can be obtained with proper mass factor.

(f) Check the total angular momentum, and run the trajectory.

3.2 Tajectory Propagation

The trajectories are propagated with either a fixed-step-size sixth order GEAR routine[26(a)] or a variable-step-size Runge-Kutta-Merson routine in the NAG library[26(b)] until $R \geq 20$ a.u. Conservation of total energy and of total angular momentum are checked at the end of each trajectory. The accuracy of the total energy is required to be within 10^{-6} hartree. The product states are binned for each trajectory in the usual quasi-classical fashion:

3.2.1 Determination of Translational Energies

(a) Total translational energy T:

$$T = \frac{1}{2\mu}(P_X^2 + P_Y^2 + P_Z^2). \quad (23a)$$

(b) From conservation of linear momentum,

CO translational energy T_{co}:

$$T_{co} = \frac{m_{H_1} + m_{H_2}}{m_c + m_o + m_{H_1} + m_{H_2}} \times T. \tag{23b}$$

H_2 translational energy T_{H_2}:

$$T_{H_2} = \frac{m_c + m_o}{m_c + m_o + m_{H_1} + m_{H_2}} \times T. \tag{23c}$$

3.2.2 Determination of Rotational States

The rotational quantum numbers are obtained from the following equations, and assigned to the nearest integers.

(a) Orbital angular momentum quantum number L:

$$| \vec{R} \times \vec{P}_R | = [\mathrm{L}(\mathrm{L}+1)]^{\frac{1}{2}} \hbar. \tag{24a}$$

(b) CO rotational quantum number j_{co}:

$$| \vec{r_1} \times \vec{P}_{r_1} | = [j_{co}(j_{co}+1)]^{\frac{1}{2}} \hbar. \tag{24b}$$

(c) H_2 rotational quantum number j_{H_2}:

$$| \vec{r_2} \times \vec{P}_{r_2} | = [j_{H_2}(j_{H_2}+1)]^{\frac{1}{2}} \hbar. \tag{24c}$$

3.2.3 Determination of Vibrational States

There are two methods of getting the product vibrational quantum numbers.

(a) From Bohr-Sommerfeld quantitation rule:

$$\int_{r<}^{r>} P_{r_i}\, dr = (\mathrm{v} + \frac{1}{2})\pi, \tag{25a}$$

where

$$P_{r_i} = \frac{x_i}{r_i} p_{x_i} + \frac{y_i}{r_i} p_{y_i} + \frac{z_i}{r_i} p_{z_i}, \qquad i = 1, 2. \tag{25b}$$

(b) From the known energy level expression of a rotating anharmonic oscillator with first order correction for centrifugal distortion and rotational interaction,

$$\frac{E(\mathrm{v,j})}{hc} = \omega_e(\mathrm{v}+\frac{1}{2}) - \omega_e x_e(\mathrm{v}+\frac{1}{2})^2 + \tilde{B}_e\mathrm{j}(\mathrm{j}+1) - \tilde{D}_e j^2(\mathrm{j}+1)^2 - \alpha_e(\mathrm{v}+\frac{1}{2})\mathrm{j}(\mathrm{j}+1). \tag{26}$$

The spectroscopic constants[27] of the H_2, D_2 and CO molecules are listed in Table VIII. Both of the above methods are implemented in the program and used to check against each other.

3.2.4 Determination of the Impact Parameter

The dissociative impact parameter b can be obtained at the end of each trajecotry by:

$$\mathrm{b} = R\sin\alpha \tag{27}$$

where α is the angle between $\vec{P}$ and $\vec{R}$.

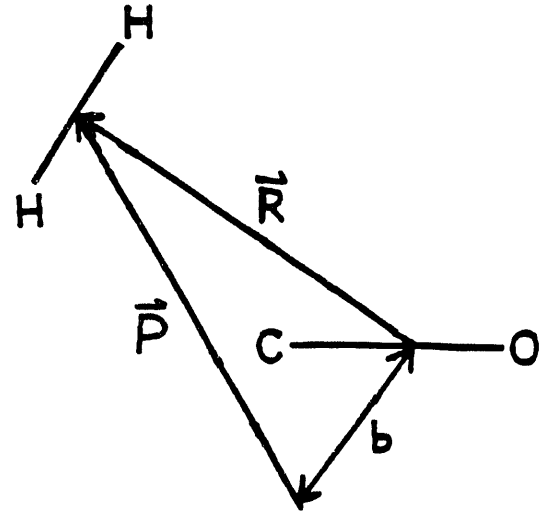

Figure 7: The dissociative impact parameter b.

4 Product State Distributions

In this section, the product state distributions from classical trajectory calculations using the CCSD PES and the MP2 PES are presented and compared with available experimental observations. The total angular momentum of the parent molecule is chosen to be ~ 0 if not noted otherwise.

4.1 H_2CO Parent Molecule

4.1.1 Translational Energy Distributions

In 1981, Ho and co-workers studied the velocity distribution of CO molecules from the fragmentation of H_2CO by time-of-flight (TOF) mass spectroscopy.[7] Individual ro-vibrational states in the $2^1 4^1$ and 4^1 vibrational bands (339 and 353 nm) were excited. The TOF spectra for the $2^1 4^1$ and 4^1 bands were found to be superimposable within experimental error. The distribution from their work is reproduced in Figure 8(a). The total product translational energy is quite high. The maximum is at 55 kcal/mol, which corresponds to 65% of the total available energy.

Figure 8(b) shows the same distribution obtained from classical trajectory calculations using the CCSD PES with total angular momentum J$\sim$0. It is normalized to have an area equal to 1. The average total translational energy is found to be 60.0 kcal/mol or 70% of the available energy. The average translational energies of H_2 and CO are 56.0 and 4.0 kcal/mol, respectively. As expected, most of the translational energy is in the H_2 degrees of freedom.

The result using the MP2 PES is shown in Figure 8(c). The average total translational energy, H_2 and CO translational energies are found to be 64.3, 60.0, and 4.3 kcal/mol, respectively. Comparisons of the two PES's shows a steeper exit channel on the MP2 PES. This causes more energy to flow into the translational degrees of freedom and a larger deviation from the experiments.

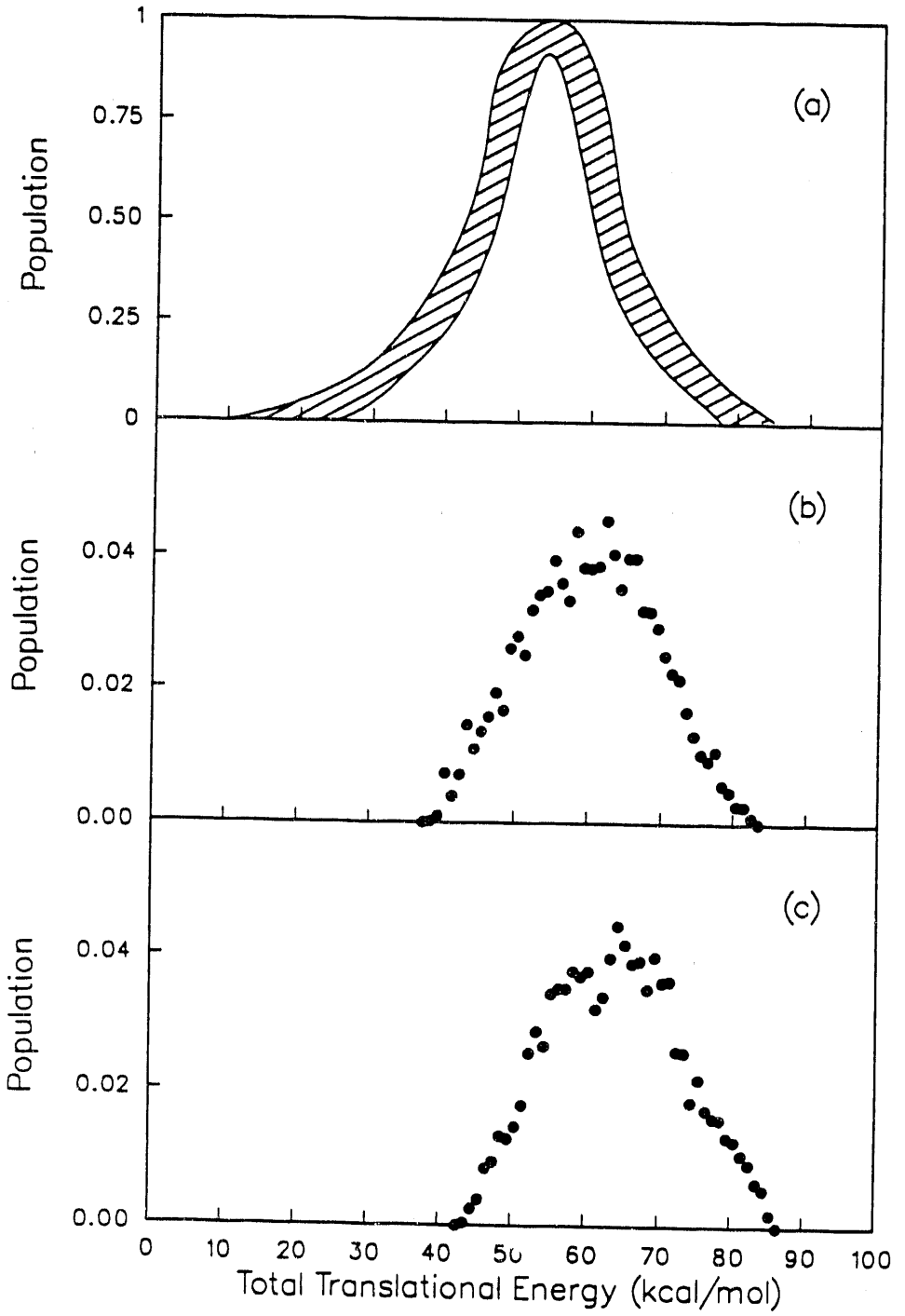

Figure 8: The distribution of the total translational energy for H_2CO parent molecule with J$\sim$ 0. (a) Result of TOF experiment. (b) Classical trajectory calculations using the CCSD PES. (c) Classical trajectory calculations using the MP2 PES.

4.1.2 H_2 Vibrational and Rotational State Distributions

The H_2(v,j) distributions were studied in 1983 (v=1-3)[8(a)] and in 1985 (v=0-4, j=1-9)[8(b)] with coherent anti-Stokes Raman spectroscopy and also in 1989 (rotational distributions of v=1 and v=3)[10] with Doppler-resolved laser-induced-fluores cence spectroscopy. The vibrational distribution was concluded to be non-statistical with the peak at v=1. The rotational distribution peaks at $j_{H_2} \sim 3$ and behaves approximately Boltzmann-like with T_{rot} = 1730° for v=1 and T_{rot} = 1240° for v=3.

Comparisons of the vibrational distributions are shown in Figure 9(a-c). The CCSD PES reproduces the experimental distributions extremely well. Not only does it peak at v=1, but it also reproduces the shape of the distribution. The MP2 PES predicts a slightly higher population in v=0 than in v=1, and near zero population in v=3. The source of this disagreement comes from the fact that the H–H distance at the transition state obtained from the MP2/DZP calculation is slightly too short.

The calculated rotational distributions for each vibrational state are shown in Figure 10(b-c). The long-dashed, dashed, dotted, and chain-dotted curves are for v=0, 1, 2, and 3, respectively. The areas under each curves reflect the relative populations in each vibrational states. Using the CCSD PES, the peak positions are at j=2 for v=0 and 1 and at j=3 for v=2 and 3. With the MP2 PES, one obtains peak positions at j=2 for v=0 and j=3 for v=1 and 2. These results agree quite well with the experiments.

The above calculated rotational distributions can be roughly fit with Boltzmann distributions. But the warmer distribution for lower H_2 vibrational states, as was found in experiment, is not seen here.

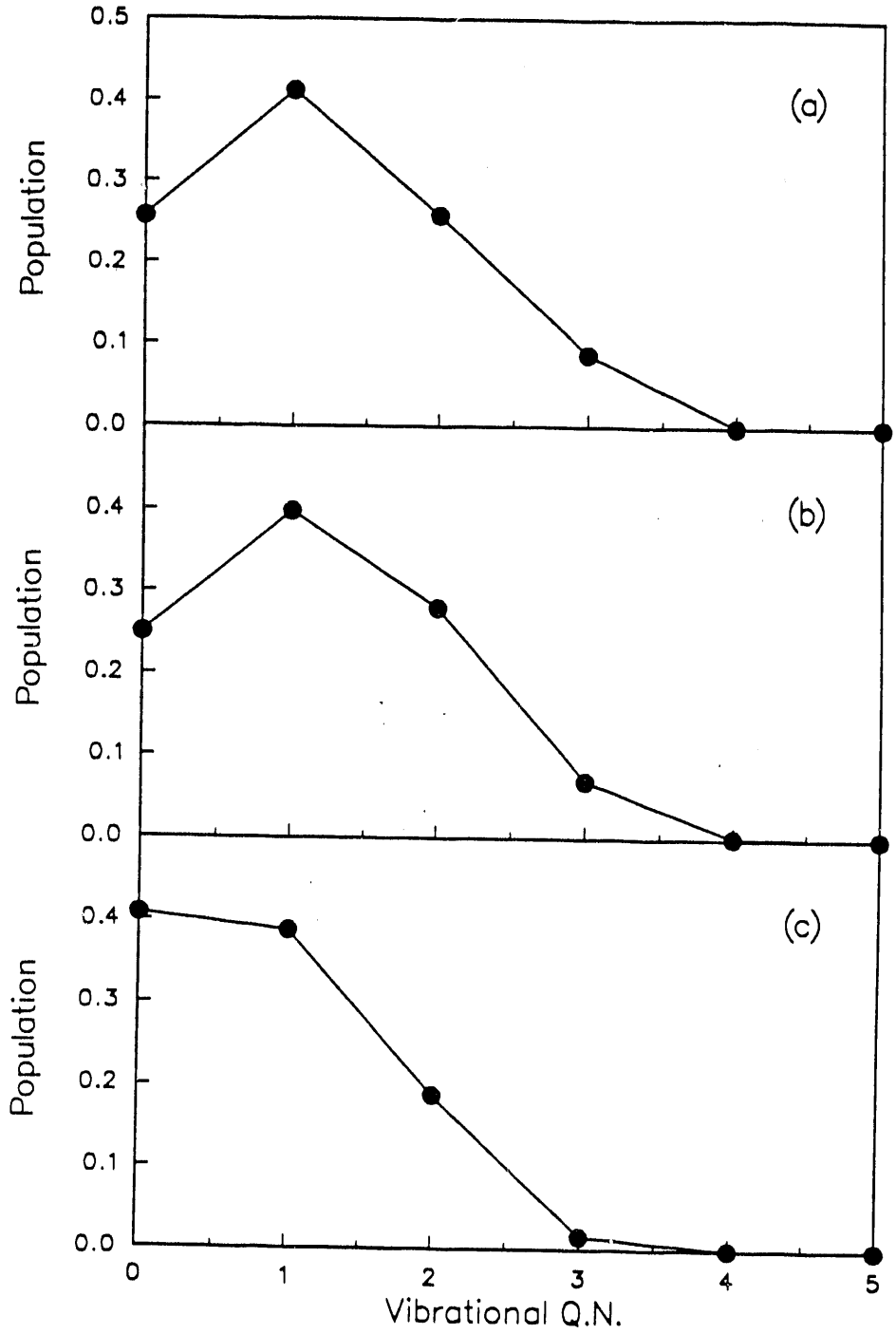

Figure 9: The populations of H_2 vibrational state. (a) Experiments. (b) Classical trajectory calculations using the CCSD PES. (c) Classical trajectory calculations using the MP2 PES.

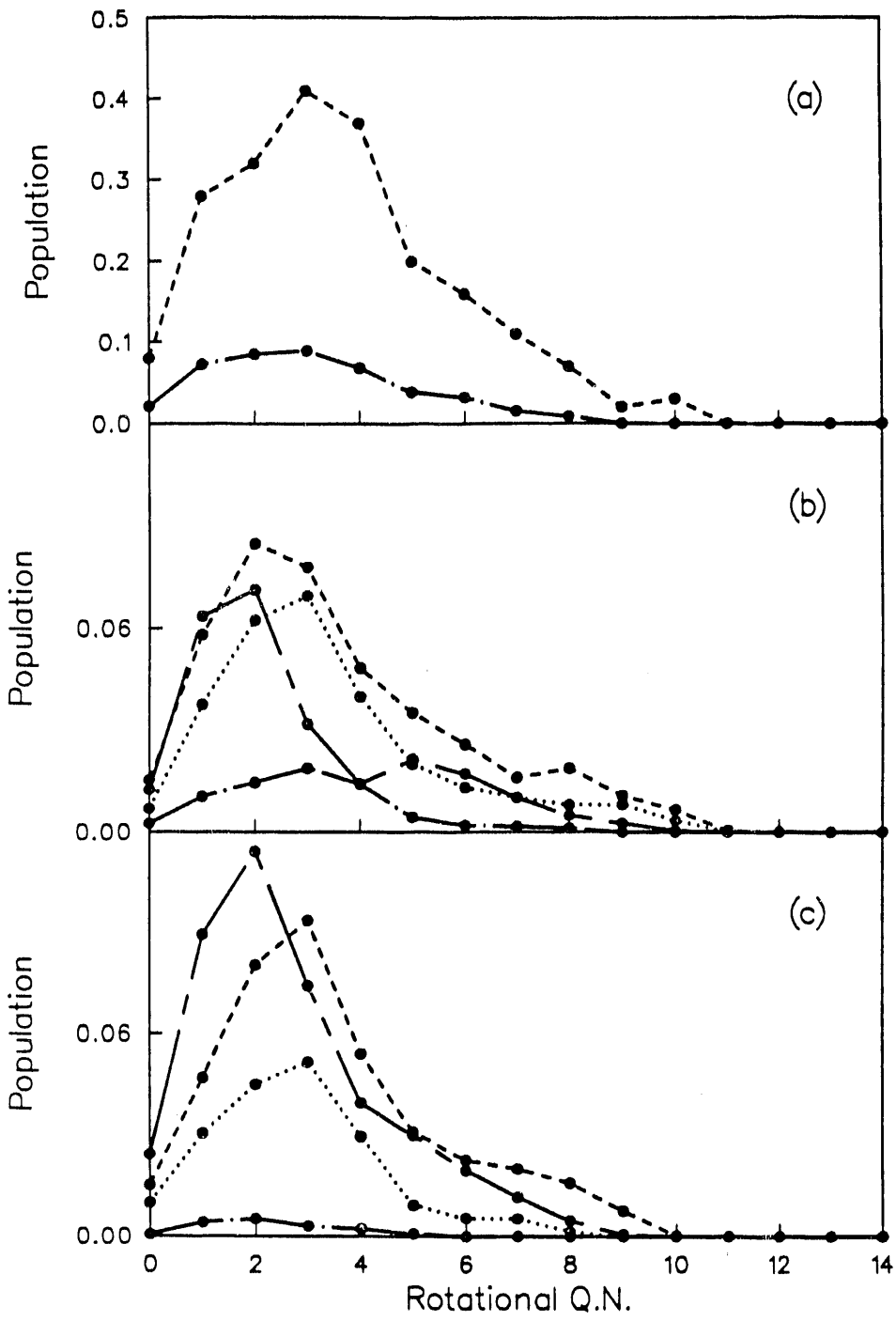

Figure 10: The populations of H_2 rotational states. The long-dashed, dashed, dotted and chain-dotted curves are for v=0, 1, 2 and 3, respectively. (a) Experiments. (b) Classical trajectory calculations using the CCSD PES. (c) Classical trajectory calculations using the MP2 PES.

4.1.3 CO Vibrational and Rotational State Distributions

In the early 1970s, the dissociation pathway and dynamics of H_2CO was not clear. It was argued that the T_1 state or a long-lived intermediate state[2] might be involved before dissociation takes place. These postulates were based, most importantly, on the observation of CO product appearance rate being much slower than the decay rate of the formaldehyde first excited singlet state. It is not until 1982, when highly rotationally excited ($j_{co} > 25$) CO molecules were observed by vacuum UV measurements, that the matter was solved. These high j CO molecules played the role of the long-lived intermediate in the earlier experiments where only CO with low j were monitored.[9(a)]

Moore and co-workers[9(b)] reported in 1984 the vibrational and rotational distributions of CO obtained from vacuum UV LIF experiments. Only the v=0 and v=1 states of CO were found and the ratio of populations was about 8 to 1 (see Figure 11(a)). The photodissociation of H_2CO with the pump laser frequency at 29512 cm^{-1} showed a large amount of rotational excitation of CO. The distribution, shown in Figure 12(a), was highly inverted with a maximum at 42 , and the full-width-at-half-maximum (FWHM) about 20-22 j units. The rotational distributions for v=0 and v=1 of CO were found to be nearly the same.

Results of the vibrational distribution from our calculations are shown in Figure 11(b-c). In agreement with the experimental results, essentially no population is found for v>1. Again, the calculation based on the CCSD PES gives excellent agreement with the experimental distribution. Calculations based on the MP2 PES, however, show that the v=0 state has smaller population (68%) and the v=1 has larger population (31%) than the experiments. This results because of a slightly longer C–O distance in the transition state predicted by the MP2/DZP calculation which causes more vibrational excitation in the product CO.

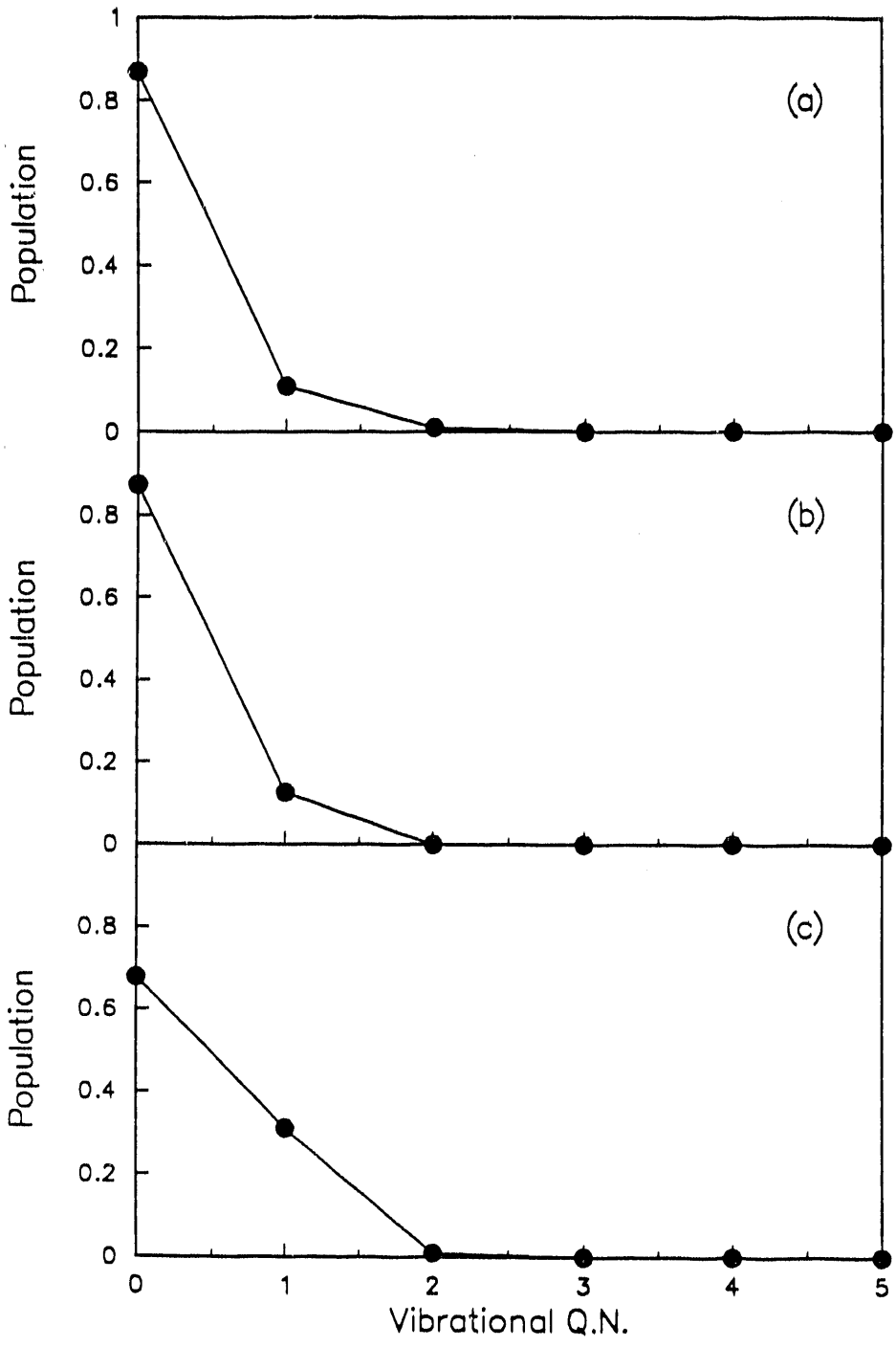

Figure 11: The populations of the CO vibrational states from H_2CO parent molecule. (a) Experiments. (b) Classical trajectory calculations using the CCSD PES. (c) Classical trajectory calculations using the MP2 PES.

The calculated CO rotational distributions for H_2CO dissociations using the two PES's are shown in Figure 12(b) and Figure 12(c). Solid dots, open circles and open squares represent the rotational distributions for v=0, 1, and 2 of CO molecules. Each distributions are then fit with Gaussians. The mean values and the FWHM are as follows:

From CCSD PES:	CO(v=0)	$< j_{co} > = 40.4$	FWHM = 15.0,
	CO(v=1)	$< j_{co} > = 41.5$	FWHM = 14.8,
From MP2 PES:	CO(v=0)	$< j_{co} > = 40.8$	FWHM = 15.1,
	CO(v=1)	$< j_{co} > = 40.3$	FWHM = 15.8.

The peak positions seem to agree reasonably well with the experiments (j=42), but the widths are found to be slightly narrower.

4.1.4 Impact Parameter Distribution

Several approximate dynamical models[10,20] have been employed to reproduce the experimental product state distributions. The impulsive model, for example, should be reasonable under the conditions that the exit valley is highly repulsive and the product vibrations are stiff. Butenhoff *et al.*[10] had used such a model, which combined an impulsive force betwen H_2 and CO and the normal mode vibrations of H_2CO, to explain the highly non-thermal rotational distribution of CO and to reproduce the experimental distributions. The results were encouraging despite the simplicity of the model.

This treatment suggested that H_2 pushes away from a point about 0.3Å outside the C nucleus of the CO molecule when the fragmentation occurs. This corresponds to an averaged impact parameter of ~0.9Å. This large impact parameter gives a strong torque on the CO molecule and thus the high rotational excitation.

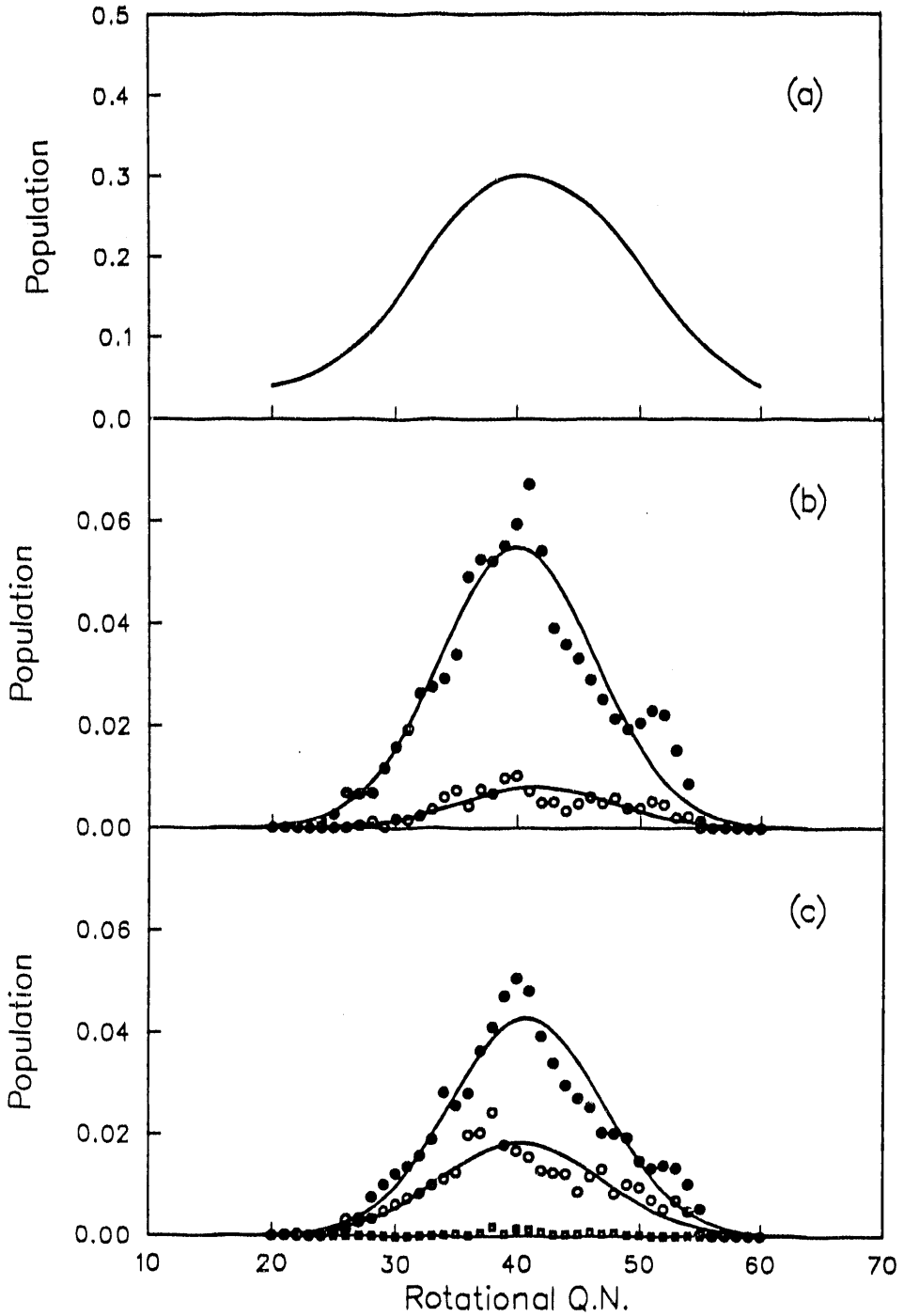

Figure 12: The populations of the CO rotational states. (a) Experiments. (b) Classical trajectory calculations using the CCSD PES. (c) Classical trajectory calculations using the MP2 PES.

In Figure 13, the distribution of the impact parameter out of 5000 trajectories shows an averaged value b=0.89Å and a spread over ± 0.4Å for H_2CO parent molecules using the CCSD PES. Since the motions of the molecules can be easily monitored as a function of time from trajectory calculations, one can get a clear picture of how and when the dissociation occurs. Figure 14 shows the behaviors of a few dynamical quantities as a function of time from one single trajectory. Figures 14(a), (b) and (c) give the distances of $r_2(H_2)$, $r_1(CO)$ and R. Figure 14(d) shows the change of the impact parameter and Figure 14(e) is the potential that the molecule 'feels' along the trajectory. One can see that within less than one vibration of the H_2 and CO molecules (roughly 10 fs after passing the transition state), the parent molecule is ready to dissociate and the dissociative impact parameter quickly becomes a constant. For this particular trajectory, we find b=0.83Å. A closer look at the motions of the two fragments clearly demonstrate that it is the C side of the CO molecule which is pushed away. This proves that the impulsive force is indeed acting outside the C atom.

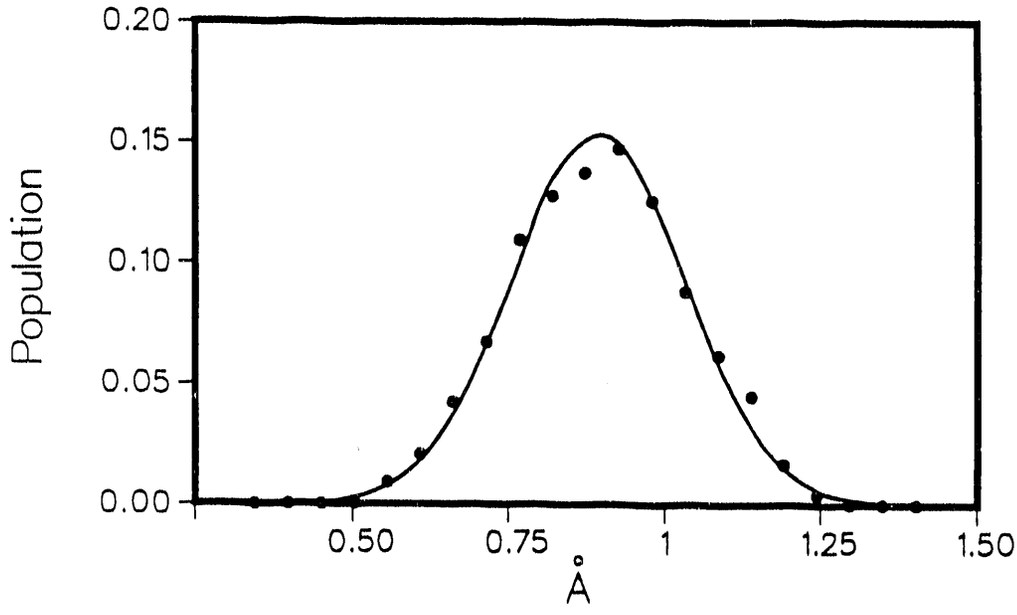

Figure 13: Distribution of the impact parameter in units of Å.

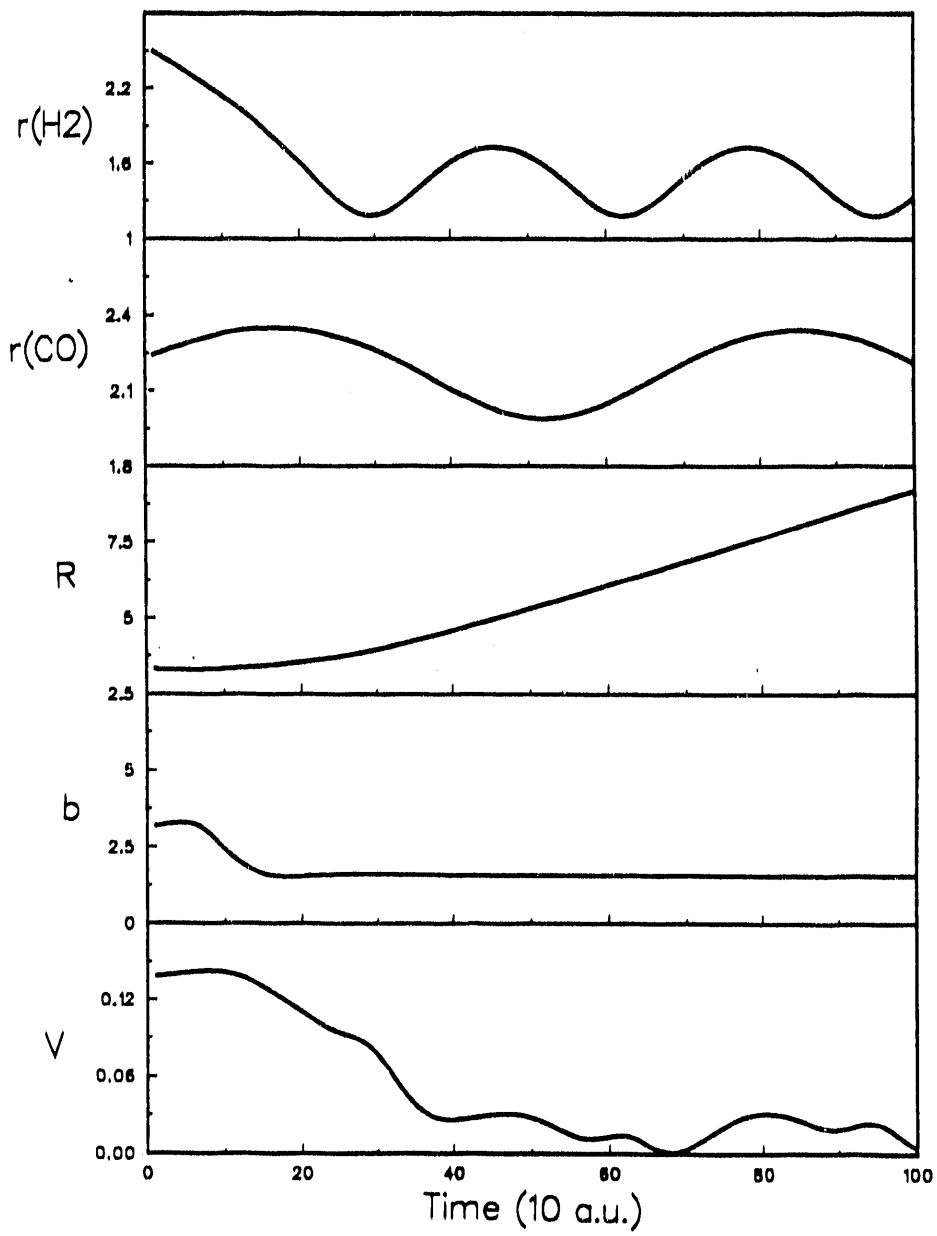

Figure 14: Some dynamical variables as a funtion of time in a typical trajectory. Atomic units are used for each variable. (a) The bond distance of H_2. (b) The bond distance of CO. (c) The center of mass distance between H_2 and CO. (d) The dissociative impact parameter. (e) The potential energy curve along the trajectory.

4.1.5 Product Quantum State Correlation

Butenhoff *et al.*[10] had also observed the correlation between the product quantum states. Namely, the higher vibrational states of H_2 are correlated with the lower rotational states of CO. This was explained through conservation of total energy, total angular momentum and the constraint of the impact parameter distribution. With the parent total angular momentum J~0, and the H_2 rotational angular momentum much smaller than that of the CO, the following equations are reasonable approximations,

$$\mathbf{J} = \mathbf{L} + \mathbf{j}_{co} + \mathbf{j}_{H_2} \simeq 0, \tag{28a}$$

$$\mathrm{L} = \mu v \mathrm{b} \simeq |\mathbf{j}_{co} + \mathbf{j}_{H_2}| \simeq |\mathbf{j}_{co}|, \tag{28b}$$

where μ is the H_2-CO reduced mass, v is the relative velocity and b is the impact parameter. When H_2 is produced in higher vibrational state, the relative velocity decreases as a result of conservation of total energy. And if the impact parameter is constrained to be within a narrow range, the orbital angular momentum L will decrease and so will j_{co}.

This correlation also appears in our results and it is summarized as follows:

	ref. 10	this work
H_2	$< j_{co} >$	$< j_{co} >$
v=0	~ 45	44.8
v=1	~ 41	40.9
v=2	~ 37	37.2
v=3	~ 35	36.1

4.1.6 Effect of Parent Total Angular Momentum

The effect of the parent rotation was studied in the Moore group.[9(b)] From the comparison of two excitations, one to J=3,4, K_a=2 and the other to J=16, K_a=0, they found that the increased parent total angular momentum is only partially transfered to CO molecule. But it also causes a slightly wider CO rotational distribution. Figure 15(a) is reproduced from their paper, and it shows a 3 unit wider distribution for the J=16, K_a=0 case.

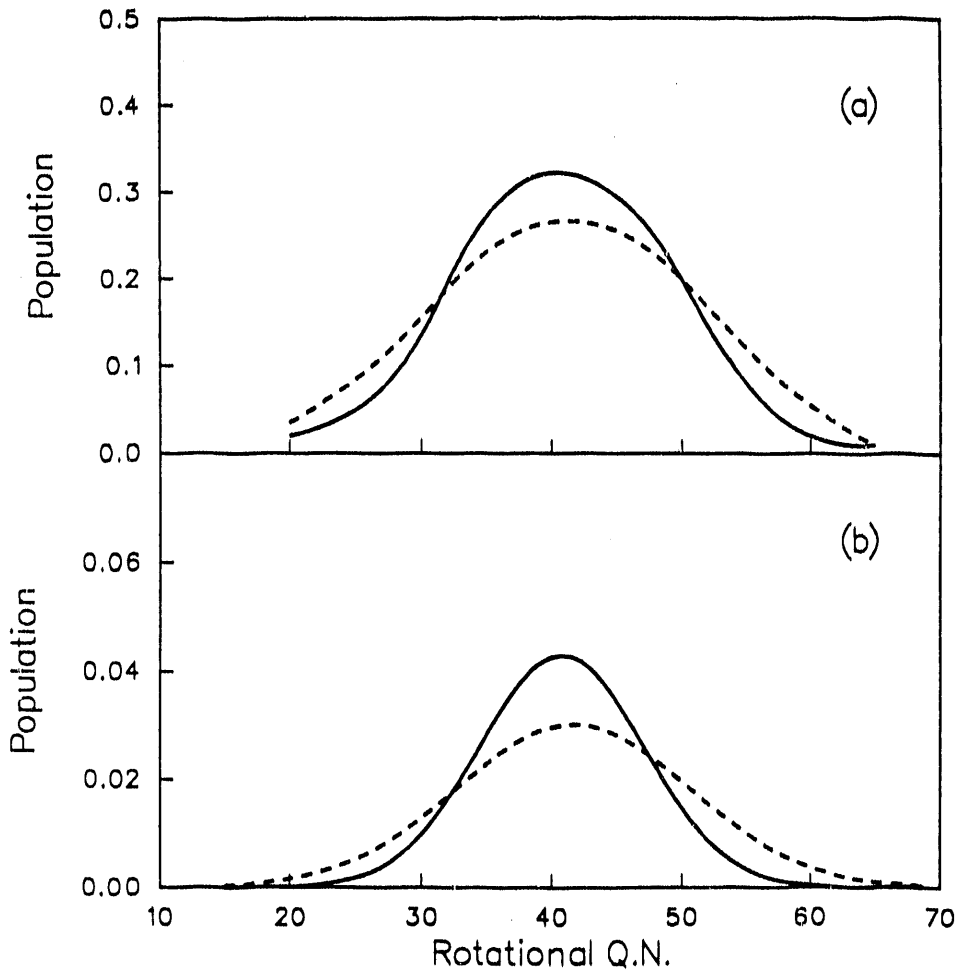

Figure 15: Rotational state distributions of CO(v=0) with different parent angular momentum. (a) Experimental results. Solid curve is for H_2CO J=3,4 K_a=2 and dashed curve is for H_2CO J=16, K_a=0. (b) Results from classical trajectory calculations. Solid curve is for H_2CO J~0 and dashed curve is for H_2CO J~15.

To verify this conclusion, we also ran classical trajectories with a higher total J(=15) for the H_2CO. The three principal axes at the transition state are found through diagonalization of the moment of inertia matrix. For initial condition with $K_a = 0$, the parent rotational energy is randomly partitioned into motion about the b and c axes. Compared to the J $\sim$ 0 calculation, a 6 units wider distribution with almost no change of the mean value is found. Figure 15(b) shows the comparison, and the result is summarized:

H_2CO J=15, K_a=0 CO(v=0) $< j_{co} >$=41.7 FWHM=21.1

H_2CO J=15, K_a=0 CO(v=1) $< j_{co} >$=41.1 FWHM=21.1 .

A further investigation is performed to look at the effect of rotation about a single principal axis. With all the parent angular momentum along the a axis, i.e., J=K_a=15, $\omega_b = \omega_c = 0$, the width of the distribution is unchanged, but the mean value $< j_{co} >$ is shifted from $\sim$41 to $\sim$44. We also find that the peak of H_2 rotational state distribution is also increased (from $j_{H_2} = 3$ to $j_{H_2} = 6$). On the other hand, if all the rotational energy is about the out-of-plane c axis, i.e., ω_a=0, ω_b=0, a much wider j_{co} distribution with no change in the peak position is obtained. The FWHM is increased by 9-10 units (from 15 to 25). For rotation merely about the b axis, we see no change on either the peak position or the FWHM.

4.2 D_2CO Parent Molecule

Experimental information of the product state distributions with D_2CO parent molecules is limited. An LIF study[9(b)] of the $rQ_0(8)e$ transition of D_2CO at 29545 cm^{-1} showed higher rotational excitation of CO in the D_2CO dissociation (peak at j$\sim$ 53) than in the H_2CO dissociation (peak at j$\sim$ 42). As shown in Figure 16(a-b), the same behavior is seen from our calculations. An earlier study[2] showed photolysis at 337.1 nm of D_2CO yields the same CO vibrational state distribution within

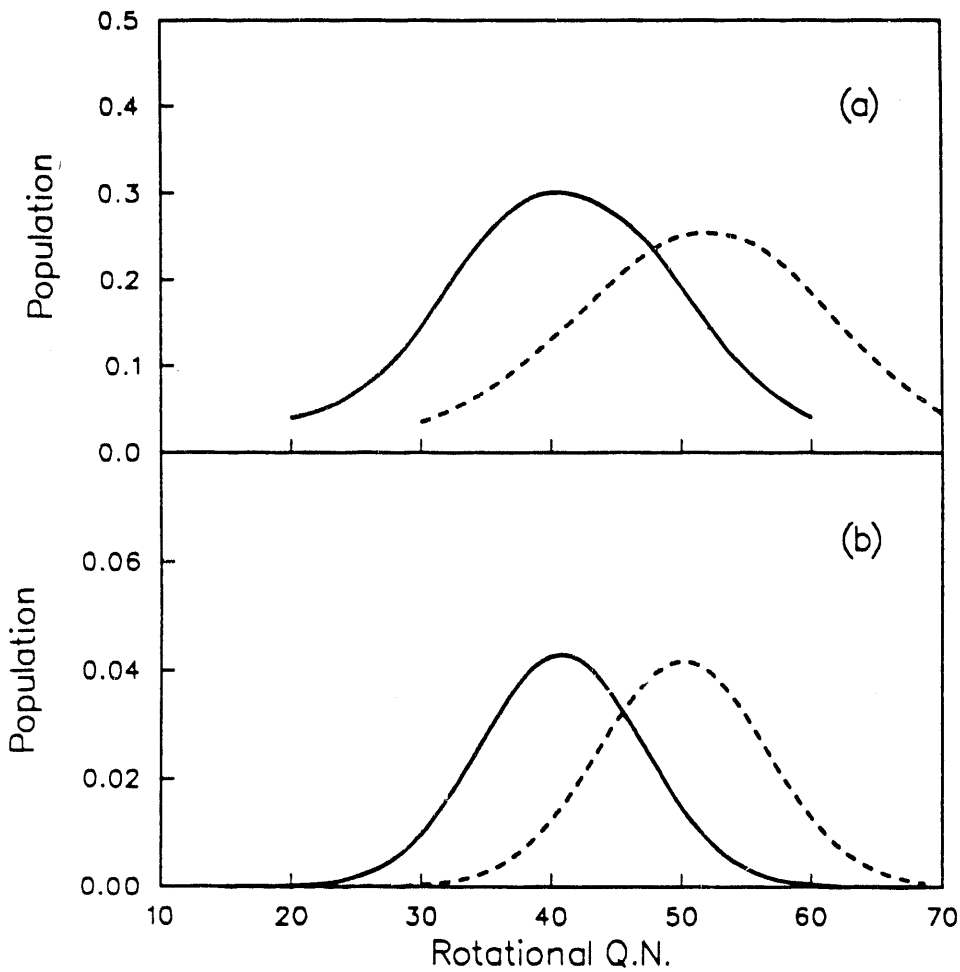

Figure 16: Rotational state distribution of CO from H_2CO and D_2CO. (a) Experimental results. Solid curve is for H_2CO J=3,4 K_a=2 and dash curve is for D_2CO J=8. (b) Results from classical trajectory calculations. Solid curve is for H_2CO J$\sim$0 and dash curve is for D_2CO J$\sim$0.

experimental error as photolysis of H_2CO. This observation is also well reproduced from our calculations using the CCSD PES.

The results (using the CCSD PES) of the product state distributions from classic al trajectory calculations with same amount of total energy (96 kcal/mol) and total angular momentum J~0 are summarized as follows:

(a) The averaged total translational energy, CO translational energy and D_2 translational energies are 54.8, 6.9 and 47.9 kcal/mol, respectively.

(b) The populations in the vibrational state of D_2 are 3.8% for v=0, 29.5% for v=1, 32.6% for v=2, 25.4% for v=3 and 8.3% for v=4.

(c) $< j_{D_2} >$ is ~ 4 for every vibrational state of D_2.

(d) The vibrational distribution of CO is same as in the H_2CO case.

(e) $< j_{co} >$ is at $\sim$ 50 to 51.

(f) The averaged impact parameter is about 0.86Å.

5 Vector Correlations

A more thorough understanding of the photofragmentation dynamics can be obtained from not only the product scalar properties, but also the vector correlations.[28] Typical vector correlations that are investigated include (1) the polarization vector E of the photolysis laser, (2) the transition dipole moment $\vec{\mu}$ of the parent molecule, (3) the fragment recoil velocity v, and (4) the fragment rotational angular momentum j.

The correlation of E with the other vectors come from the fact that the transition probability is proportional to $(\vec{\mu} \cdot \mathbf{E})^2$. Thus those parent molecules whose transition dipole moment lies parallel to E are more likely to be excited. The consequence is

an anisotropic distribution of the dissociating parent molecules. In the limit when the molecules dissociate promptly after excitation, the angular relation between the transition dipole moment and the recoil velocity **v** is preserved, and one observes the velocity anisotropy (characterized as β) in the laboratory frame. However, rotation of the parent molecule prior to dissociation destroys the alignment between $\vec{\mu}$ and **E**. Therefore, if the lifetime of the parent molecule is much longer than the rotational period, which is true for many predissociation reactions[28(i)], one expects the spatial distribution of the fragments to be less anisotropic even though the correlation between $\vec{\mu}$ and **v** still exists in the molecular frame. Similar arguments apply to the alignment (characterized as $A_0^{(2)}$) of the fragment rotational angular momentum. On the other hand, the vector correlation between **v** and **j** will not be washed out by parent rotational motion. This is because the **v-j** correlation occurs at the moment when the parent molecule is about to dissociate.

5.1 Angular Distribution and Dissociation Mechanism

The excitation of formaldehyde from the ground electronic state to the $2^1 4^1$ band of the excited state is a b-type transition.[11,29] This implies the transition dipole moment is parallel to the b axis in the molecular frame. At the transition state, this axis is almost perpendicular to the CO bond and lies on the molecular plane. Figure 17(a) illustrates the axes. The convention used here is (c,a,b)=(x,y,z). Notice that the z axis in the molecular frame is defined to be along the parent transition dipole moment.

Since our trajectory study mimics the case of a prompt dissociation, the fragment spatial distributions give direct information about the dissociation dynamics in the molecular frame. In our calculation, the polar angle and azimuthal angle of **v** are defined in Figure 17(b) as θ_v and ϕ_v. Those of fragments' **j** are θ_j and ϕ_j. The angle

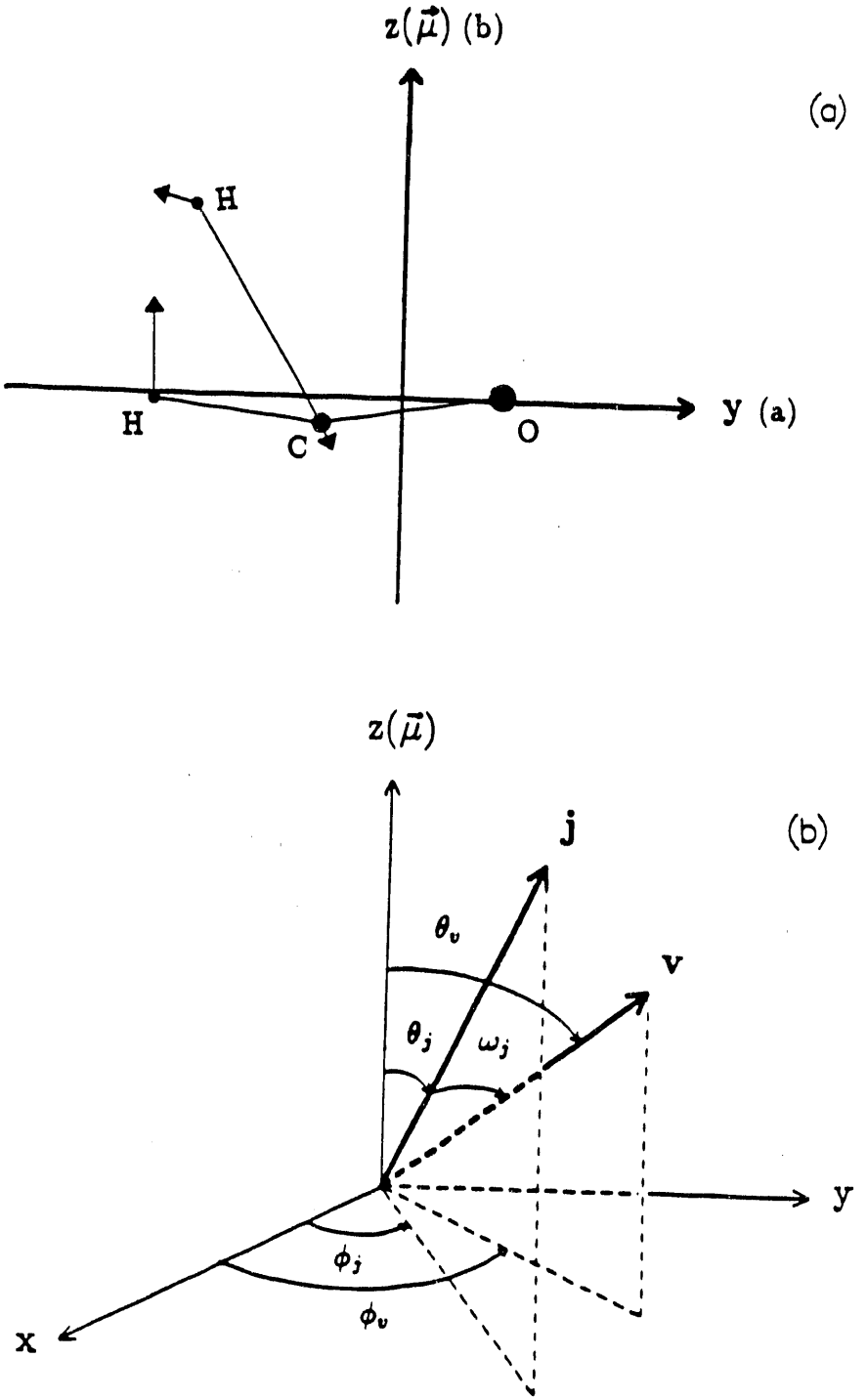

Figure 17: (a) The three principal axes at the transition state geometry. c axis is pointing out of paper. (b) Definition of the polar and azimuthal angles of v and j.

between **v** and **j** is represented by ω_j. The spatial distributions using the CCSD PES are discussed in detail below. Results using the MP2 PES are found to be almost identical except for the distribution of θ_v.

5.1.1 Spatial Distribution of Recoil Velocity

The distributions , using the CCSD PES, of θ_v and ϕ_v from 5000 trajectories are shown in Figure 18(a-b). A planar dissociation of H_2CO corresponds to ϕ_v=270°. The narrow distribution (with the maximum deviation $\sim$ 10°) of ϕ_v in Figure 18(b) indicates a near-planar (ab-plane) dissociation. The distribution of θ_v lies between $\sim$ 20° and 40° using the CCSD PES and between 30° and 60° using the MP2 PES.

5.1.2 Spatial Distribution of CO Angular Momentum

Figure 19(a-c) shows the distributions of θ_{j_1},ϕ_{j_1} and ω_{j_1} for the CO molecule. One sees narrow distributions peaking at 90° for θ_{j_1}, at 0° for ϕ_{j_1} and at 90° for ω_{j_1}. A closer look at the vector $\mathbf{j}_{co}$ from each trajectory verifies that $\mathbf{j}_{co}$ is usually parallel to the c axis and is always a counterclockwise motion according to Figure 17(a). Three in-plane normal modes at the transition state contribute to the rotation of CO about the c axis, ν_3, ν_5, and ν_6 (shown in Figure 4). But the phases of ν_3 and ν_5 can cause either clockwise or counterclockwise rotation. Therefore, one concludes that the most important contribution to the CO rotation is the repulsive impulsive force between CO and H_2, which causes the counterclockwise rotation of CO ($\phi_{j_1} \sim 0°$) and the perpendicular vector relationship ($\omega_{j_1} \sim 90°$) between the recoil velocity and the rotational angular momentum of CO.

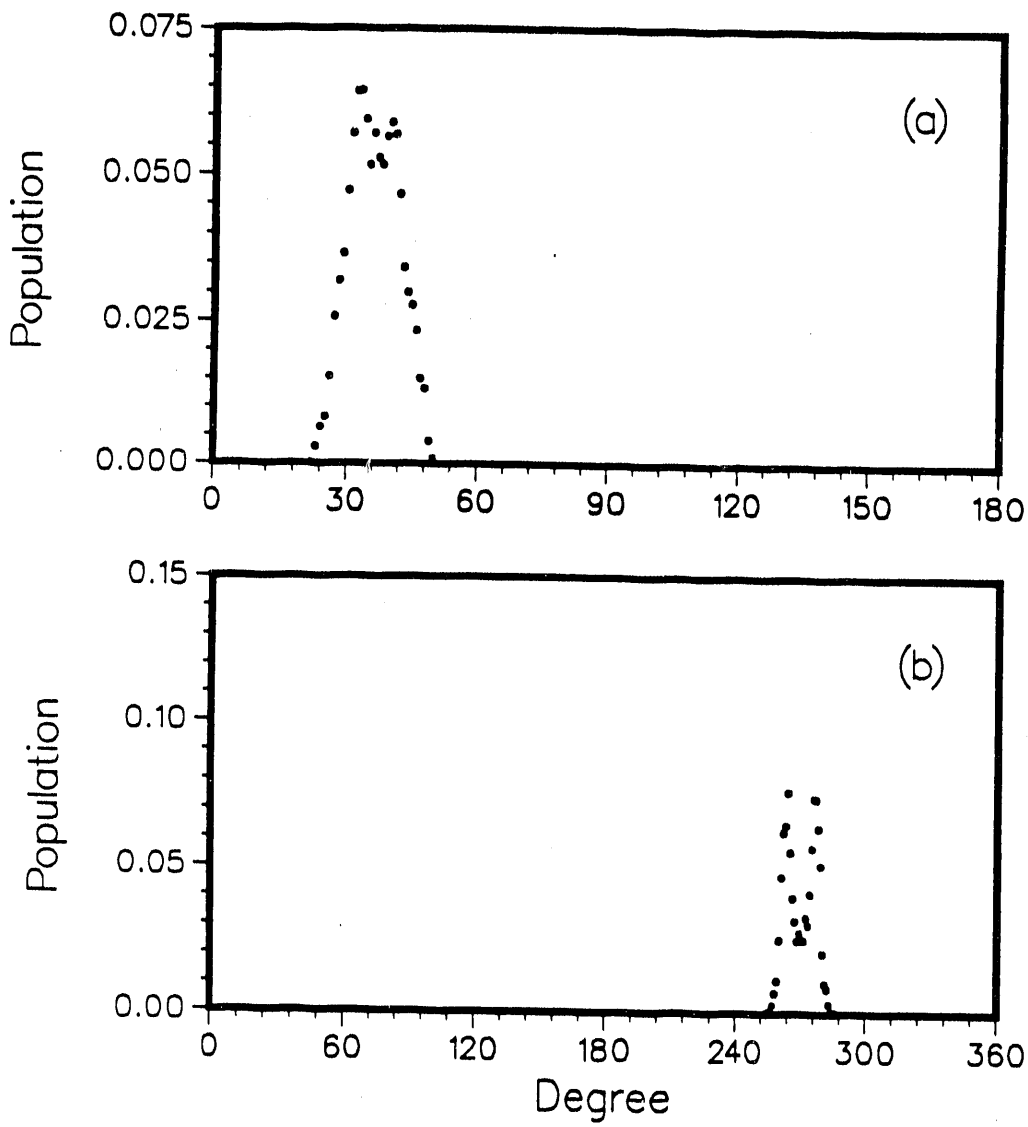

Figure 18: Spatial distribution of the recoil velocity. (a) θ_v. (b) ϕ_v.

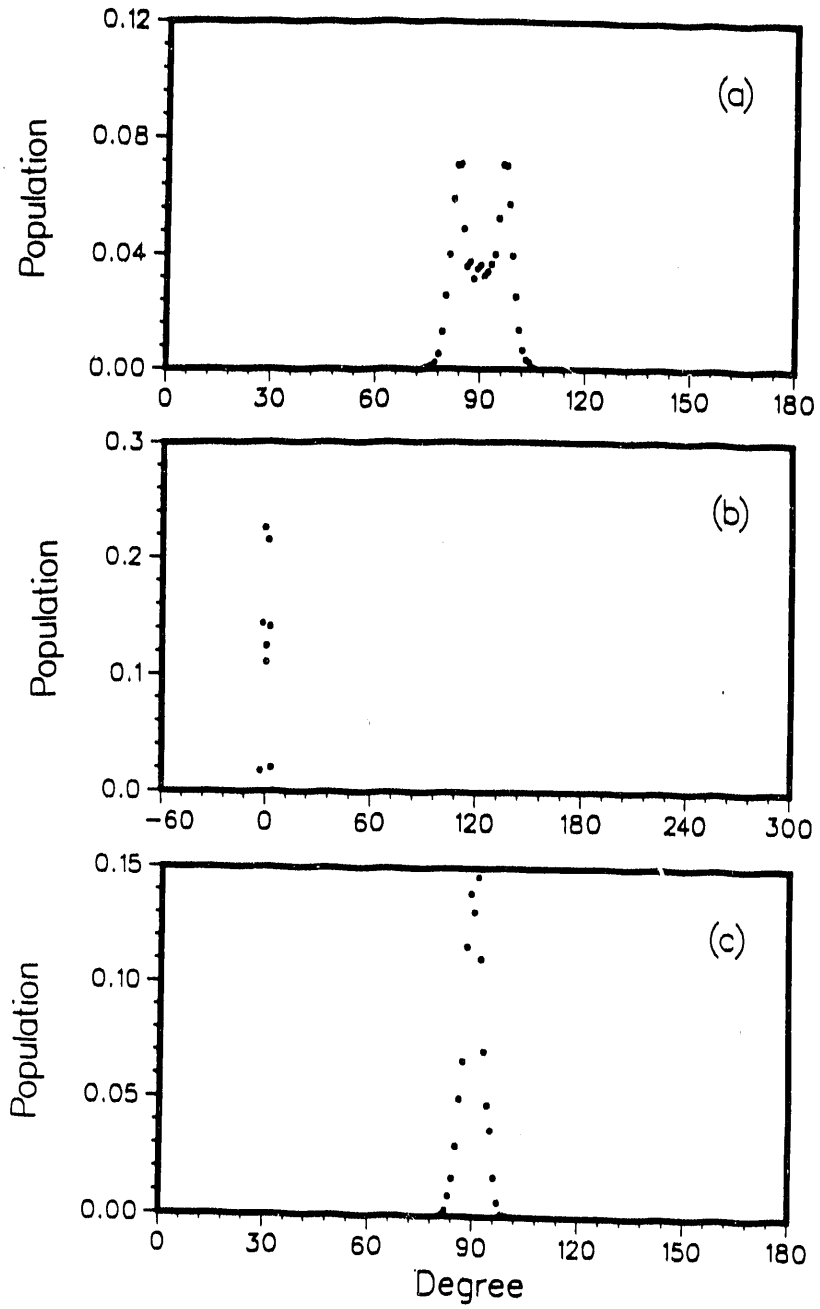

Figure 19: Spatial distribution of CO angular momentum $\mathbf{j}_{co}$. (a) θ_{j_1}. (b) ϕ_{j_1}. (c) ω_{j_1}.

5.1.3 Spatial Distribution of H_2 Angular Momentum

Figure 20(a-c) gives the distributions of θ_{j_2}, ϕ_{j_2},and ω_{j_2} for H_2. Unlike the CO molecule, the angular momentum of H_2 has a much wider spatial distribution. The ranges of the angles are roughly $60° < \theta_{j_2} < 120°$, $0° < \phi_{j_2} < 360°$ and $30° < \omega_{j_2} < 150°$. An ab-planar rotation (i.e., rotation about the c axis) of $\mathbf{j}_{H_2}$ will have $\phi_{j_2} = 0°$ (counterclockwise) or 180° (clockwise), whereas rotation about the a or b axis results in $\phi_{j_2} = 90°$ or 270°. By inspecting the three components of the vector $\mathbf{j}_{H_2}$, we found that there is little contribution from rotation about the b axis. This is easy to understand since the b axis is almost parallel to the H_2 bond.

The different behavior between $\mathbf{j}_{co}$ and $\mathbf{j}_{H_2}$ can be understood from the normal mode vibrational motions at the transition state. All of the normal modes have very little character of CO rotational motion. But the amplitudes of H_2 motions are usually large. The out-of-plane mode ν_4 contributes to the rotation of H_2 mostly about the a axis. The phase of this normal mode determines the angle of ϕ_{j_2} to be close to either 90° or 270°. The in-plane vibrational modes, especially ν_1, ν_5 and ν_6(the reaction coordinate) contribute to the rotation about the c axis. The net result is the wide spatial distribution of $\mathbf{j}_{H_2}$ in the ac-plane.

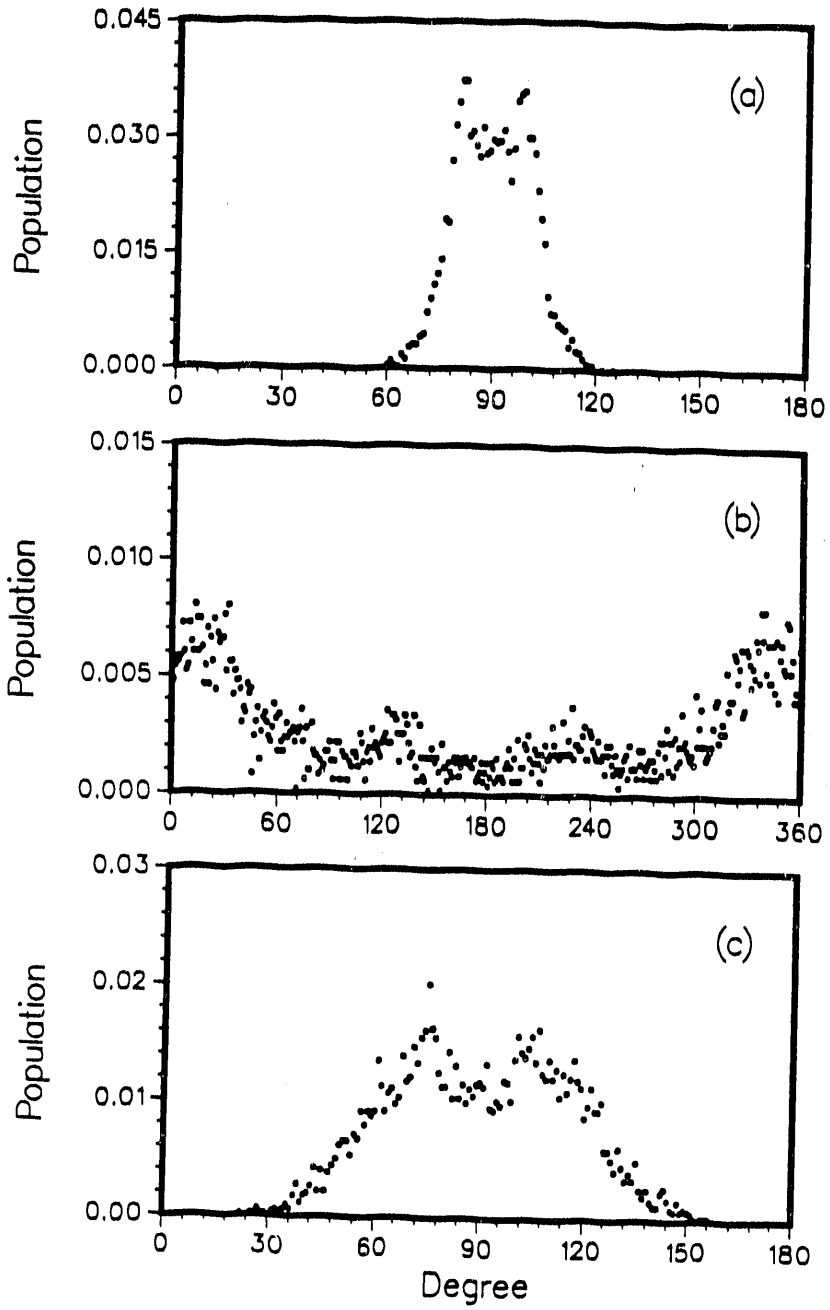

Figure 20: Spatial distribution of H_2 angular momentum j_{H_2}. (a) θ_{j_2}. (b) ϕ_{j_2}. (c) ω_{j_2}.

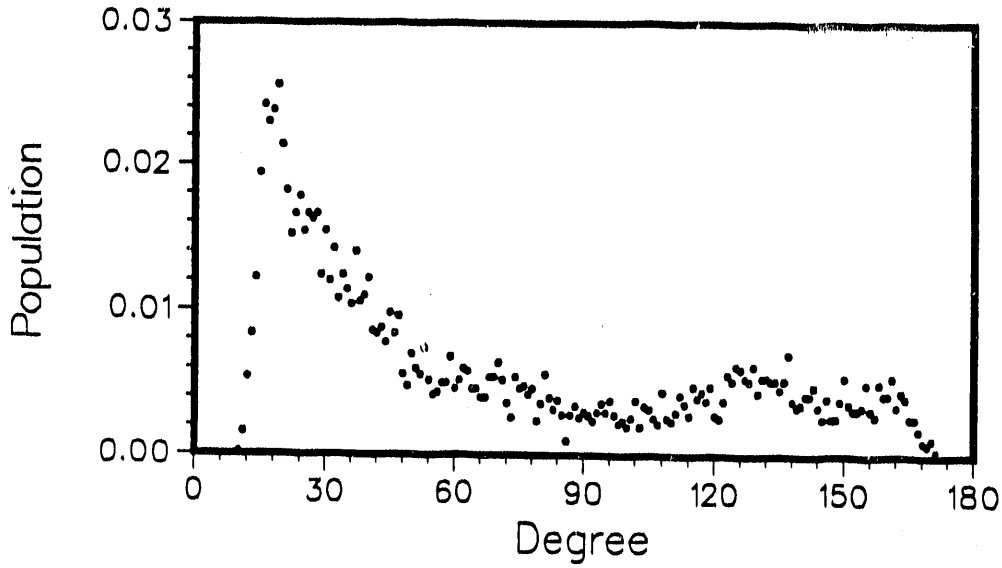

Figure 21: Distribution of angle χ between j_{co} and j_{H_2}.

5.1.4 Angular Relationship between j_{co} and j_{H_2}

The reaction coordinate at the transition state indicates co-rotation (both clockwise or both counterclockwise) between CO and H_2 molecules. It is interesting to know to what extent this co-rotation behavior will be preserved. If the angle between j_{co} and j_{H_2} is defined as χ, a co-rotation motion will have χ close to 0°, whereas a counter-rotation (one clockwise, the other counterclockwise) has χ close to 180°. The distribution of χ is shown in Figure 21. One sees a larger probability of co-rotation than counter-rotation. But there are many trajectories in regions where $j_{H_2} \perp j_{co}$. These trajectories result from a combination of CO in-plane rotation and H_2 out-of-plane motion.

5.1.5 Dissociation Mechanism

From the results of the product state distributions and the above analysis of the vectors of the fragments, a clear picture of the dissociation process is obtained. After H_2CO passes through the transition state, the steep repulsive potential causes instantaneous dissociation to occur in a time shorter than one vibration of H_2 and CO, resulting in the high translational energies in the fragments. Since H_2 is much lighter than CO, most of the translational energy is in the H_2 degrees of freedom. If there is not much energy in the out-of-plane vibrational mode ν_4, the fragmentation is a near-planar process with the recoil velocity lying mainly in the molecular plane.

The CO vibration is quite stiff along the exit valley. Therefore, the vibrational population of CO is mainly in v=0. The impulsive force acting on the carbon side of CO molecule causes high rotational excitation (and thus the highly non-thermal rotational distribution) of CO and counterclockwise rotation about the c axis. Since the recoil velocity lies mainly in the molecular plane, the vectors v and j_{co} are almost perpendicular to each other.

The potential for H_2 motion around the transition state region is more anharmonic. The H_2 distance at the saddle point corresponds to the v$\sim$3 outer turning point of free H_2. Therefore, the vibrational distribution of H_2 spans v=0–3. Contributions from the impulsive force and the vibrational motions make a wide spatial distribution (in the ac-plane) of the H_2 angular momentum.

5.2 State Resolved Anisotropy

For products produced in the ground state, as is the case for the dissociation of formaldehyde on the S_0 surface, the technique of Doppler-resolved laser-induced-flourescence (LIF) is used to probe the quantum state resolved anisotropy. The influence of the vector correlations on the line profiles has been formulated with

classical[28(c)] and quantum mechanical[28(d)] methods. Dixon[28(f)] has developed a useful method which extracts the vector correlations from the measured Doppler line shapes

$$g(\bar{\nu}) \sim \frac{1}{2\triangle\bar{\nu}_D}\left[1 + \beta_{eff} \mathrm{P}_2(\cos\theta)\mathrm{P}_2(\chi_D)\right], \tag{29}$$

where $\triangle\bar{\nu}_D = \bar{\nu}_0 v/c$ is the maximum Doppler shift, χ_D is the ratio of the displacement from line center to $\triangle\bar{\nu}_D$, $[\chi_D = \bar{\nu} - \bar{\nu}_0/\triangle\bar{\nu}_D]$, $\mathrm{P}_2(\mathrm{x}) = 1/2(3\mathrm{x}^2\text{-}1)$ is the second Legendre polynomial, θ is the angle between the photolysis vector and the probed laser propagation axis, and β_{eff} is the effective anisotropy parameter which is related to a set of bipolar moments $\beta_0^k(k_1 k_2)$ and bipolar moment multipliers $\mathrm{b}_0, \cdots, \mathrm{b}_4$[11(d)] (these are constants which depend on the fragment's j, the probed rotational transition, and the experimental geometry) by:

$$\beta_{eff} = \left[\frac{b_2\beta_0^2(20) + b_3\beta_0^0(22) + b_4\beta_0^2(22)}{(b_0 + b_1\beta_0^2(02))\,\mathrm{P}_2(\cos\theta)}\right]. \tag{30}$$

The quantity $A_0^{(2)}$ is equal to 4/5 $\beta_0^2(02)$ and β is equal to $2\beta_0^2(20)$ in Dixon's analysis. $\beta_0^0(22)$ characterizes the **v-j** correlation and $\beta_0^2(22)$ is for the $\vec{\mu}$-**v**-**j** triple vector correlation. In the limit of high fragment j and prompt dissociation, the expectation values of these bipolar moments are

$$A_0^{(2)} = \frac{2}{5} < \mathrm{P}_2(\cos\theta_j) >, \tag{31.a}$$

$$\beta = 2\beta_0^2(20) = 2 < \mathrm{P}_2(\cos\theta_v) >, \tag{31.b}$$

$$\beta_0^0(22) = < \mathrm{P}_2(\cos\omega_j) >, \tag{31.c}$$

$$\beta_0^2(22) =< -\mathrm{P}_2(\cos\theta_v)\mathrm{P}_2(\cos\theta_j) - \frac{3}{8}\sin 2\theta_v \sin 2\theta_j \cos(\phi_v - \phi_j)$$
$$+\frac{3}{4}\sin^2\theta_v \sin^2\theta_j \cos[2(\phi_v - \phi_j)] > . \qquad (31.d)$$

Table IX lists the values of the bipolar moments for a few extreme orientations of v and j with respect to $\vec{\mu}$ in the case of high fragment j and prompt dissociation. If the vectors involved are perpendicular (parallel or antiparallel) to each oth er, the corresponding anisotropy is usually negative (positive). The limits are

$$-0.4 < A_0^{(2)} < 0.8 \qquad (32.a)$$

$$-1 < \beta < 2 \qquad (32.b)$$

$$-0.5 < \beta_0^0(22) < 1 \qquad (32.c)$$

$$-0.5 < \beta_0^2(22) < 1 \qquad (32.d)$$

Moore and co-workers[11] have used Dixon's method to analyze the LIF profiles of the H_2 molecule as a function of parent vibrational states ($2^1 4^1$ and 4^3), parent rotational states (through ${}^{p}P_1(1)$, ${}^{p}P_1(2)$, ${}^{r}R_0(0)$,$\cdots$, ${}^{r}R_0(3)$, and ${}^{r}Q_0(1)$, $\cdots$, ${}^{r}Q_0(3)$ transitions), H_2 vibrational states (v=1 or 3), and H_2 rotational states (j_{H_2}=0 to 8). In general, their results showed negative $A_0^{(2)}$ (in one case, $A_0^{(2)} = -0.31$ for H_2(v=3,j=2)) which suggests a more perpendicular than parallel relation between $\vec{\mu}$ and $\mathbf{j}_{H_2}$. Our distribution of θ_{j_1} centers at 90°, which agrees with this indication. The anisotropy of β is found to depend sensitively on both the parent's and the fragment's rovibrational states. Values of β as large as 0.85 (from the ${}^{r}R_0(0)$ transition to $2^1 4^1$ band of $H_2CO(S_1)$, H_2(v=3,j=0)) and as small as -0.41 (${}^{r}R_0(0)$ transition to the 4^3 band, H_2(v=1,j=2)) are reported. The corresponding θ_v's for these two cases

($\sim$ 38° for β=0.85 and $\sim$ 64° for $\beta = -0.41$) are within the two limits of our θ_v distribution (from ~30 to ~60°) using the MP2 PES. The $\beta_0^0(22)$ values for the v-j correlation are found in the experiments to be constant (within error bars) as a funtion of the H_2(v,j) and photolysis transition. The weighted average for all of the H_2(v,j) is $\beta_0^0(22) = -0.23 \pm 0.02$, which is closer to the limit of $\mathbf{v} \perp \mathbf{j}_{H_2}$ than $\mathbf{v} \| \mathbf{j}_{H_2}$. The average values of $\beta_0^0(22)$ using the CCSD PES and the MP2 PES are found to be -0.25 and -0.20, respectively.

A direct comparison of the quantum-state resolved anisotropy between the experiments and our classical trajectory calculations may lead to false conclusions for the following reasons: (1) Our study prepares initial conditions which leads to prompt dissociation. However, the experiment prepares S_1 H_2CO molecule with a long lifetime, which diminishes the anisotropy for many of the quantum states. (2) Well defined parent ro-vibrational states are excited in the experiments. The observed anisotropy depends strongly on these initial states. However, the initial parent states in our calculation are mixed with many rotational states (from J=0 to 3, and the K_a is not resolved) and vibrational states (random distribution of the energy into the 6 normal modes at the transition state geometry). (3) The direction of the transition dipole moment to the 4^3 band of H_2CO is argued to be slightly deviated from the b axis.[11] In our calculation, we assume that $\vec{\mu}$ is always parallel to the b axis. A more meaningful comparison can be made if one can prepare identical initial conditions as in the experiment and if the parent rotation is treated more rigorously.

6 Discussion and Conclusion

The molecular dissociation dynamics of formaldehyde on the ground state potential energy surface has been studied through classical trajectory calculations. The

overall picture of the dissociation process is the same as that predicted from experiments. Yet, the motion of the two fragments, H_2 and CO, are easily monitored from the trajectories and give a better view of how and when dissociation occurs. The vibrational state distributions obtained from using the CCSD PES give better agreement with experiments than those from the MP2 PES. This demonstrates that these distributions are governed by the transition state geometry and the shape of the potential around the transition state. The rotational state distribution of CO is determined mainly by the impulsive force between H_2 and CO.

A complete vector analysis is performed for both H_2 and CO fragments in this work, while the experiments were performed only for H_2. A near-planar dissociation, observed from the distribution of the recoil velocity, is seen using both the CCSD PES and MP2 PES. The vectors $\mathbf{v}$ and $\mathbf{j}_{co}$ are found to be almost perpendicular to each other due to the impulsive force. On the other hand, the angular momentum of H_2 has a much wider spatial distribution due to combination of the impulsive force, the in-plane normal mode vibration and the out-of-plane bending motion.

The inability to prepare identical parent ro-vibrational states as in the experiments prevents the study of the effect of parent internal state and the direct comparison of the quantum state resolved anisotropy. However, the prompt dissociation conditions used in our trajectory calculation gives a clear description of the dissociation dynamics in the molecular frame. The experimental vector correlations are a convolution of those in the molecular frame with the rotational motion of H_2CO before dissociation.

It is encouraging that the PES's constructed from the EVB model reproduce most of the experimental observations. The simplicity of the model allows reasonable PES to be obtained from a limited amount of *ab initio* calculations. Yet, from the comparison among the experimental results and our calculations, some improvements on the surface are suggested: (1) The steeper potential along the exit valley on

the MP2 PES results in too much energy being partitioned into the translational degrees of freedom. The CCSD PES , which is less steep, gives better agreement for the translational distribution but it is still a few kcal too high. It appears that one needs to flatten the potential along the exit valley. (2) The experimental study[11(c)] of the effect of parent rotational states on the anisotropy β for H_2(v=1,j=0) suggests, with some approximation, that the recoil velocity **v** is about 23° off from the molecular plane. Although more experimental evidence is required to verify this argument, the out-of-plane torsional potential should be improved in order to obtain a less planar dissociation. Harding's *ab initio* calculation[30] of a few points around the transition state region shows sharper variation of the potential in the out-of-plane angle than our current PES's. Lester's intrinsic reaction coordinate (IRC) calculation[31] shows an imaginary frequency in the out-of-plane mode at geometries about 40 kcal/mol below their MC4/DZP transition state. These two studies support the important role of the out-of-plane motion in the dissociation dynamics.

It is obvious that the crucial region that controls the reaction is region aboutthe transition state configuration. Previous studies showed that the energies of the T_1, and S_1 origins, the S_0 transition state and the H+HCO threshold all lie within a range of 10–15 kcal/mol. The coupling among these configurations makes the PES around the transition state extremely anharmonic. More *ab initio* calculations for this region of the surface would thus still be useful.

Appendix A: B Matrix

Define $d\mathbf{q} = \mathbf{B} \cdot d\mathbf{X}$, where $\mathbf{q}$ represents the 3N-6 internal coordinate vector and $\mathbf{X}$ the 3N-3 Jacobi coordinate vector. The elements of $\mathbf{q}$ and $\mathbf{X}$ are defined in section 2.1. The derivation of the matrix element of $\mathbf{B}$ is straightforword except th\ se involve the out-of-plane torsional angle ϕ. The results are shown as follows:

$$B_{11} = X/R$$

$$B_{12} = Y/R$$

$$B_{13} = Z/R$$

$$B_{24} = x_1/r_1$$

$$B_{25} = y_1/r_1$$

$$B_{26} = z_1/r_1$$

$$B_{37} = x_2/r_2$$

$$B_{38} = y_2/r_2$$

$$B_{39} = z_2/r_2$$

$$B_{41} = -\frac{1}{\sqrt{1-\cos\gamma_1{}^2}} \times \left[\frac{x_1}{Rr_1} - \frac{X\left(\vec{R}\cdot\vec{r}_1\right)}{R^3 r_1}\right]$$

$$B_{42} = -\frac{1}{\sqrt{1-\cos\gamma_1{}^2}} \times \left[\frac{y_1}{Rr_1} - \frac{Y\left(\vec{R}\cdot\vec{r}_1\right)}{R^3 r_1}\right]$$

$$B_{43} = -\frac{1}{\sqrt{1-\cos\gamma_1{}^2}} \times \left[\frac{z_1}{Rr_1} - \frac{Z\left(\vec{R}\cdot\vec{r}_1\right)}{R^3 r_1}\right]$$

$$B_{44} = -\frac{1}{\sqrt{1-\cos\gamma_1{}^2}} \times \left[\frac{X}{Rr_1} - \frac{x_1\left(\vec{R}\cdot\vec{r}_1\right)}{Rr_1{}^3}\right]$$

$$B_{45} = -\frac{1}{\sqrt{1-\cos\gamma_1{}^2}} \times \left[\frac{Y}{Rr_1} - \frac{y_1\left(\vec{R}\cdot\vec{r}_1\right)}{Rr_1{}^3}\right]$$

$$B_{46} = -\frac{1}{\sqrt{1-\cos\gamma_1{}^2}} \times \left[\frac{Z}{Rr_1} - \frac{z_1\left(\vec{R}\cdot\vec{r}_1\right)}{Rr_1{}^3}\right]$$

$$B_{51} = \frac{1}{\sqrt{1-\cos\gamma_2{}^2}} \times \left[\frac{x_2}{Rr_2} - \frac{X\left(\vec{R}\cdot\vec{r}_2\right)}{R^3r_2}\right]$$

$$B_{52} = \frac{1}{\sqrt{1-\cos\gamma_2{}^2}} \times \left[\frac{y_2}{Rr_2} - \frac{Y\left(\vec{R}\cdot\vec{r}_2\right)}{R^3r_2}\right]$$

$$B_{53} = \frac{1}{\sqrt{1-\cos\gamma_2{}^2}} \times \left[\frac{z_2}{Rr_2} - \frac{Z\left(\vec{R}\cdot\vec{r}_2\right)}{R^3r_2}\right]$$

$$B_{57} = \frac{1}{\sqrt{1-\cos\gamma_2{}^2}} \times \left[\frac{X}{Rr_2} - \frac{x_2\left(\vec{R}\cdot\vec{r}_2\right)}{Rr_2{}^3}\right]$$

$$B_{58} = \frac{1}{\sqrt{1-\cos\gamma_2{}^2}} \times \left[\frac{Y}{Rr_2} - \frac{y_2\left(\vec{R}\cdot\vec{r}_2\right)}{Rr_2{}^3}\right]$$

$$B_{59} = \frac{1}{\sqrt{1-\cos\gamma_2{}^2}} \times \left[\frac{Z}{Rr_2} - \frac{z_2\left(\vec{R}\cdot\vec{r}_2\right)}{Rr_2{}^3}\right]$$

$$B_{61} = -\frac{1}{\sqrt{1-\cos\phi^2}} \times \left\{\frac{2X\left(\vec{r}_1\cdot\vec{r}_2\right) - x_1\left(\vec{R}\cdot\vec{r}_2\right) - x_2\left(\vec{R}\cdot\vec{r}_1\right)}{\sqrt{R^2r_1{}^2 - \left(\vec{R}\cdot\vec{r}_1\right)^2}\sqrt{R^2r_2{}^2 - \left(\vec{R}\cdot\vec{r}_2\right)^2}}\right.$$

$$-\frac{\left[R^2\left(\vec{r}_1\cdot\vec{r}_2\right) - \left(\vec{R}\cdot\vec{r}_1\right)\left(\vec{R}\cdot\vec{r}_2\right)\right]\left[Xr_2{}^2 - x_2\left(\vec{R}\cdot\vec{r}_2\right)\right]}{\sqrt{R^2r_1{}^2 - \left(\vec{R}\cdot\vec{r}_1\right)^2}\left[R^2r_2{}^2 - \left(\vec{R}\cdot\vec{r}_2\right)^2\right]^{3/2}}$$

$$\left.-\frac{\left[R^2\left(\vec{r}_1\cdot\vec{r}_2\right) - \left(\vec{R}\cdot\vec{r}_1\right)\left(\vec{R}\cdot\vec{r}_2\right)\right]\left[Xr_1{}^2 - x_1\left(\vec{R}\cdot\vec{r}_1\right)\right]}{\left[R^2r_1{}^2 - \left(\vec{R}\cdot\vec{r}_1\right)^2\right]^{3/2}\sqrt{R^2r_2{}^2 - \left(\vec{R}\cdot\vec{r}_2\right)^2}}\right\}$$

The expressions for B_{62} and B_{63} are identical to B_{61} except (X, x_1, x_2) should be replaced by (Y, y_1, y_2) or (Z, z_1, z_2), respectively.

$$B_{64} = -\frac{1}{\sqrt{1-\cos\phi^2}} \times \left\{ \frac{x_2 R^2 - X\left(\vec{R}\cdot\vec{r}_2\right)}{\sqrt{R^2 {r_1}^2 - \left(\vec{R}\cdot\vec{r}_1\right)^2}\sqrt{R^2 {r_2}^2 - \left(\vec{R}\cdot\vec{r}_2\right)^2}} \right.$$
$$\left. - \frac{\left[R^2\left(\vec{r}_1\cdot\vec{r}_2\right) - \left(\vec{R}\cdot\vec{r}_1\right)\left(\vec{R}\cdot\vec{r}_2\right)\right]\left[x_1 R^2 - X\left(\vec{R}\cdot\vec{r}_1\right)\right]}{\left[R^2 {r_1}^2 - \left(\vec{R}\cdot\vec{r}_1\right)^2\right]^{3/2}\sqrt{R^2 {r_2}^2 - \left(\vec{R}\cdot\vec{r}_2\right)^2}} \right\}$$

$$B_{67} = -\frac{1}{\sqrt{1-\cos\phi^2}} \times \left\{ \frac{x_1 R^2 - X\left(\vec{R}\cdot\vec{r}_1\right)}{\sqrt{R^2 {r_1}^2 - \left(\vec{R}\cdot\vec{r}_1\right)^2}\sqrt{R^2 {r_2}^2 - \left(\vec{R}\cdot\vec{r}_2\right)^2}} \right.$$
$$\left. - \frac{\left[R^2\left(\vec{r}_1\cdot\vec{r}_2\right) - \left(\vec{R}\cdot\vec{r}_1\right)\left(\vec{R}\cdot\vec{r}_2\right)\right]\left[x_2 R^2 - X\left(\vec{R}\cdot\vec{r}_2\right)\right]}{\sqrt{R^2 {r_1}^2 - \left(\vec{R}\cdot\vec{r}_1\right)^2}\left[R^2 {r_2}^2 - \left(\vec{R}\cdot\vec{r}_2\right)^2\right]^{3/2}} \right\}$$

Again, the expressions for B_{65}, B_{66}, B_{68} and B_{69} can be obtained by proper substitutions of X, x_1, x_2.

The transformation between the 3N cartesian coordiantes and 3N-3 Jacobi coordinates are very simple. Only the non-zero matrix elements are shown here.

$$B'_{11} = B'_{22} = B'_{33} = -\frac{m_c}{m_c + m_o}$$
$$B'_{14} = B'_{25} = B'_{36} = -\frac{m_o}{m_c + m_o}$$
$$B'_{17} = B'_{28} = B'_{39} = \frac{m_{H_1}}{m_{H_1} + m_{H_2}}$$
$$B'_{1,10} = B'_{2,11} = B'_{3,12} = \frac{m_{H_2}}{m_{H_1} + m_{H_2}}$$
$$B'_{41} = B'_{52} = B'_{63} = B'_{77} = B'_{88} = B'_{99} = 1$$
$$B'_{44} = B'_{55} = B'_{66} = B'_{7,10} = B'_{8,11} = B'_{9,12} = -1$$

Appendix B: G Matrix

The definition of the G matrix in 3N-6 internal coordinates is given as[23(a)]

$$G_{tt'} = \sum_{i=1}^{3N} \frac{1}{m_i} C_{ti} C_{t'i'} \qquad t, t' = 1, 2, \ldots, 3N-6$$

or in matrix notation

$$\mathbf{G} = \mathbf{C} \cdot \mathbf{M} \cdot \mathbf{C}^T$$

where

$$\mathbf{M} = \mathbf{m}^{-1}$$

and

$$\mathbf{C} = \mathbf{B} \cdot \mathbf{B}'$$

The formulae of the non-zero matrix element are:

$$G_{11} = \frac{1}{\mu}$$

$$G_{22} = \frac{1}{\mu_1}$$

$$G_{33} = \frac{1}{\mu_2}$$

$$G_{44} = \frac{1}{\mu_1 {r_1}^2} + \frac{1}{\mu R^2}$$

$$G_{45} = -\frac{\cos\phi}{\mu R^2}$$

$$G_{46} = \frac{\sin\phi \cot\gamma_2}{\mu R^2}$$

$$G_{55} = \frac{1}{\mu_2 {r_2}^2} + \frac{1}{\mu R^2}$$

$$G_{56} = \frac{\sin\phi \cot\gamma_1}{\mu R^2}$$

$$G_{66} = \frac{G_{44}}{\sin^2\gamma_1} + \frac{G_{55}}{\sin^2\gamma_2} - \frac{2\left[1 - \cos\phi \cot\gamma_1 \cot\gamma_2\right]}{\mu R^2}$$

References

[1] R. D. McQuigg and J. G. Calvert, *J. Am. Chem. Soc.* **91**, 1590 (1969).

[2] P. L. Houston and C. B. Moore, *J. Chem. Phys.* **65**, 757 (1976).

[3] C.-K. Cheng, P. Ho, C. B. Moore, and M. B. Zughul, *J. Phys. Chem.* **88**, 296 (1983).

[4] (a) K. Yamada, T. Nakagawa, K. Kuchitsu, and Y. Morino, *J. Mol. Spectrosc.* **38**, 70 (1971).
(b) D. J. Clouthier and D. A. Ramsay, *Ann. Rev. Phys. Chem.* **34**, 31 (1983).
(c) D. E. Reisner, R. W. field, J. L. Kinsey, and H.-L. Dai, *J. Chem. Phys.* **80**, 5968 (1984).
(d) K. Nakagawa, R. H. Schwendeman, and J. W. C. Johns, *J. Mol. Spectrosc.* **122**, 462 (1987).
(e) S.-C. Hsu, R. H. Schwendeman, and G. Magerl, *J. Mol. Spectrosc.* **136**, 157 (1989).

[5] C. B. Moore and J. C. Weisshaar, *Ann. Rev. Phys. Chem.* **34**, 525 (1983).

[6] (a) D. R. Guyer, W. F. Polik, and C. B. Moore, *J. Chem. Phys.* **84**, 6519 (1986).
(b) H. Bitto, D. R. Guyer, W. F. Polik, and C. B. Moore, *Faraday Discuss. Chem. Soc.* **82**, 149 (1986).
(c) W. F. Polik, D. R. Guyer, and C. B. Moore, *J. Chem. Phys.* **92**, 3453 (1990).

[7] P. Ho, D. J. Bamford, R. J. Buss, Y. T. Lee, and C. B. Moore, *J. Chem. Phys.* **76**, 3630 (1982).

[8] (a) M. Pealat, D. Debarre, J. M. Marie, J. P. E. Taran, A. Tramer, and C. B. Moore,*Chem. Phys. Lett.* **98**, 299 (1983).
(b) D. Debarre, M. Lefebvre, M. Pealat, J. P. E. Taran, D. J. Bamford, and C. B. Moore, *J. Chem. Phys.* **83**, 4476 (1985).

[9] (a) P. Ho and A. V. Smith,*Chem. Phys. Lett.* **90**, 407 (1982).
(b)D. J. Bamford, S. V. Filseth, M. F. Foltz, J. W. Hepbun, and C. B. Moore, *J. Chem. Phys.* **82**, 3032 (1984).

[10] T. J. Butenhoff, K. L. Carleton, and C. B. Moore, *J. Chem. Phys.* **92**, 377 (1990).

[11] (a) T. J. Butenhoff, K. L. Carleton, M.-C. Chuang, and C. B. Moore, *J. Chem. Soc., Faraday Trans.* **85**, 1155 (1989).
(b) K. L. Carleton, T. J. Butenhoff, and C. B. Moore, *J. Chem. Phys.* **93**, 3907 (1990).

(c) T. J. Butenhoff, K. L. Carleton, R. D. van Zee, and C. B. Moore, *J. Chem. Phys.* **94**, 1947 (1990).
(d) T. J. Butenhoff, Ph. D. Thesis, U. C. Berkeley (1990).

[12] J. D. Goddard and H. F. Schaefer III, *J. Chem. Phys.* **70**, 5117 (1979).

[13] J. D. Goddard, Y. Yamaguchi, and H. F. Schaefer III, *J. Chem. Phys.* **75**, 3459 (1981).

[14] M. Dupuis, W. A. Lester Jr., B. H. Lengsfield III, and B. Liu, *J. Chem. Phys.* **79**, 6167 (1983).

[15] M. J. Frisch, J. S. Binkley, and H. F. Schaefer, *J. Chem. Phys.* **81**, 1882 (1984).

[16] (a) W. H. Green Jr., A. Willetts, D. Jayatilaka, and N. C. Handy, *Chem. Phys. Lett.* **169**, 127 (1990).
(b) N. C. Handy, private communication.

[17] G. E. Scuseria and H. F. Schaefer III, *J. Chem. Phys.* **90**, 3629 (1989).

[18] R. L. Jaffe, D. M. Hayes, and K. Morokuma, *J. Chem. Phys.* **60**, 5108 (1974).

[19] W. H. Miller, R. Hernandez, N. C. Handy, D. Jayatilaka, and A. Willetts, *Chem. Phys. Lett.* , **172**, 62 (1990).

[20] (a) R. Schinke, H. Meyer, U. Buck, and G. H. F. Diercksen, *J. Chem. Phys.* **80**, 5518 (1984).
(b) Z. Bačić, R. Schinke, and G. H. F. Diercksen, *J. Chem. Phys.* **82**, 236 (1985).
(c) Z. Bačić, R. Schinke, and G. H. F. Diercksen, *J. Chem. Phys.* **82**, 245 (1985).
(d) R. Schinke, *Chem. Phys. Lett.* **120**, 129 (1985).
(e) R. Schinke, *J. Chem. Phys.* **84**, 1487 (1986).

[21] N. C. Handy and S. Carter, *Chem. Phys. Lett.* **79**, 118 (1981).

[22] Y. T. Chang and W. H. Miller, *J. Phys. Chem.* **94**, 5884 (1990).

[23] (a) E. B. Wilson, Jr., J. C. Decius, and P. C. Cross, *Molecular Vibrations*; Dover : New York, 1955.
(b) S. Califano, *Vibrational States*, Wiley: London, New York, 1976.
(c) T. Miyazawa, *J. Chem. Phys.* **29**, 246 (1958)

[24] P. Pulay, *Mol. Phys.* **17**, 197 (1969).

[25] J. B. Marion, *Classical Dynamics*; Harcourt Brace Jovanovich (1970).

[26] (a) C. W. Gear, *Siam. J. Num. Anal., Ser. B,* **2**, 69 (1965).
(b) NAG fortran library , Mark 14 (1990) was developed by the Numerical Algorithms Group.

[27] The spectroscopic constants are from: G. Hertzberg, *Spectra of Diatomic Molecules*; Van Nostrand Reinhold : New York (1950), Table 39.

[28] (a) C. H. Greene and R. N. Zare, *Ann. Rev. Phys. Chem.* **33**, 119 (1982).
(b) C. H. Greene and R. N. Zare, *J. Chem. Phys.* **78**, 6741 (1983).
(c) G. E. Hall, N. Sivakumar, D. Chawla, P. L. Houston, and I. Burak, *J. Chem. Phys.* **88**, 3682 (1988).
(d) G. E. Hall, N. Sivakumar, P. L. Houston, and I. Burak, *Physical Review Letters*, **56**, 1671 (1986).
(e) P. L. Houston, *J. Phys. Chem.* **91**, 5388 (1987).
(f) R. N. Dixon, *J. Chem. Phys.* **85**, 1866 (1986).
(g) K.-H. Gericke, S. Klee, F. J. Comes, and R. N. Dixon, *J. Chem. Phys.* **85**, 4463 (1986).
(h) S.-C. Yang and R. Bersohn, *J. Chem. Phys.* **61**, 4400 (1974).
(i) T. Nagata, T. Kondow, K. Kuchitsu, G. W. Loge, and R. N. Zare, *Mol. Phys.*, **50**, 49 (1983).

[29] J Michael Hollas, *High Resolution Spectroscopy*; Butterworths :London, Boston (1982).

[30] Lawrence B. Harding, private communication.

[31] William A. Lester,Jr., private communication.

Table I. Coefficients for H_2 and CO vibrational potentials[a,b]

	D_e	r_0	a_1	a_2	a_3
H_2	0.17456	1.402	2.0532	1.0476	0.4823
CO	0.41248	2.132	1.9537	0.4329	0.2279

[a] From ref 21.
[b] Units are in atomic units.

Table II. Summary of total (in hartrees) and relative (in kcal/mol) energies of the formaldehyde

	MP2[a]	MP4SDTQ[b]	CCSD[c]	experiment
H_2		-1.171916	-1.17088	
CO		-113.16245	-113.12497	
H_2CO		-114.33949	-114.31822	
H_2CO^*		-114.20255	-114.17418	
$\triangle E(H_2CO \rightarrow H_2CO^*)$	94.7	85.94	90.4 (86.8)[e]	86
Excitation Energy[d]			(81.4)[e]	78–81.1[f]
				79.2±0.8[g]
$\triangle E(H_2CO \rightarrow H_2 + CO)$		3.22	(0.9)[e]	5.2[h]

[a] ref 16(b), MP2/DZP optimized geometries.
[b] ref 15, MP2/6-31G(d) optimized geometries, 6-311 + + G(3df,3pd) basis set.
[c] ref 17, CCSD/TZ2P optimezed geometries.
[d] Excitation energy = classical barrier height + zero-point energy correction.
[e] ref 17, data based on CCSDT-1 calculations with CCSD/TZ2P optimization geometries.
[f] ref 6(a). JCP 84, 6519 (1986) D_2CO 79.1–82.2 kcal/mol.
[g] ref 6(c). JCP 92, 3453 (1990) D_2CO 80.6±0.8 kcal/mol.
[h] ref 17.

Table III. Geometries in Jacobi type internal coordinates of formaldehyde at equilibrium and transition states[a,b]

	CCSD/TZ2P optimized			MP2/DZP optimized		
	$\mathbf{q}^{eq}$	$\mathbf{q}^{*}$	$\mathbf{q}^{**}$	$\mathbf{q}^{eq}$	$\mathbf{q}^{*}$	$\mathbf{q}^{**}$
R	2.391	3.321	3.321	2.421	3.310	3.310
r_1	2.274	2.198	2.198	2.311	2.248	2.248
r_2	3.528	2.467	2.467	3.537	2.342	2.342
γ_1	0°	32.04°	32.04°	0°	31.25°	31.25°
γ_2	90.0°	77.73°	102.27°	90.0°	80.14°	99.86°
ϕ		0°	180°		0°	180°

[a] $\mathbf{q}^{eq}$ is the equilibrium geometry. $\mathbf{q}^{*}$ and $\mathbf{q}^{**}$ are the two transition state geometries. They are obtained by transforming geometries from refs. 16(b) and 17.
[b] Bond distances in bohr, angles in degree.

Table IV. Force constant matrix for formaldehyde at the equilibrium geometry[a,b]

CCSD/TZ2P						
		R	r_1	r_2	γ_1	γ_2	ϕ
	R	0.28853					
	r_1	-0.08058	0.85647				
	r_2	0.09876	-0.04058	0.13539			
	γ_1	0.0	0.0	0.0	1.37680		
	γ_2	0.0	0.0	0.0	0.26004	0.78097	
	ϕ	0.0	0.0	0.0	0.0	0.0	0.45623
MP2/DZP							
		R	r_1	r_2	γ_1	γ_2	ϕ
	R	0.29993					
	r_1	-0.09274	0.82859				
	r_2	0.10438	-0.04879	0.14190			
	γ_1	0.0	0.0	0.0	1.45490		
	γ_2	0.0	0.0	0.0	-0.31447	0.81596	
	ϕ	0.0	0.0	0.0	0.0	0.0	0.47416

[a] Units of force constant are hartree/bohr^2, hartree/bohr*radian , hartree/radian^2.
[b] Only the lower triangle of this symmetric matrix is shown.

Table V. Force constant matrix for formaldehyde at transition state 1[a,b]

CCSD/TZ2P						
	R	r_1	r_2	γ_1	γ_2	ϕ
R	0.20305					
r_1	-0.07646	1.02710				
r_2	0.08712	-0.03098	0.00726			
γ_1	-0.22791	0.13621	0.18648	-0.26308		
γ_2	0.36905	-0.27888	0.02932	0.10174	0.58706	
ϕ	0.0	0.0	0.0	0.0	0.0	0.04807
MP2/DZP						
	R	r_1	r_2	γ_1	γ_2	ϕ
R	0.21839					
r_1	-0.09636	1.00330				
r_2	0.10064	-0.03955	0.01302			
γ_1	-0.25214	0.15286	0.21961	-0.29644		
γ_2	0.38297	-0.28989	0.03121	0.12814	0.56742	
ϕ	0.0	0.0	0.0	0.0	0.0	0.04859

Table VI. Force constant matrix for formaldehyde at the transition state 2[a,b]

CCSD/TZ2P						
	R	r_1	r_2	γ_1	γ_2	ϕ
R	0.20305					
r_1	-0.07646	1.02710				
r_2	0.08712	-0.03098	0.00726			
γ_1	-0.22791	0.13621	0.18648	-0.26308		
γ_2	-0.36905	0.27888	-0.02932	-0.10174	0.58706	
ϕ	0.0	0.0	0.0	0.0	0.0	0.04807
MP2/DZP						
	R	r_1	r_2	γ_1	γ_2	ϕ
R	0.21839					
r_1	-0.09636	1.00330				
r_2	0.10064	-0.03955	0.01302			
γ_1	-0.25214	0.15286	0.21961	-0.29644		
γ_2	-0.38297	0.28989	-0.03121	-0.12814	0.56742	
ϕ	0.0	0.0	0.0	0.0	0.0	0.04859

[a] Units of force constant are hartree/bohr^2, hartree/bohr*radian , hartree/radian^2.
[b] Only the lower triangle of this symmetric matrix is shown.

Table VII. Normal modes and harmonic frequencies[a] at the transition state q*

CCSD/TZ2P							
		1	2	3	4	5	6
	R	0.62344	0.47111	0.06882	0.00000	0.74300	-0.41340
	r_1	-0.16801	0.74828	-0.05632	0.00000	-0.06208	0.04011
	r_2	0.34609	0.44800	0.97200	0.00000	0.26449	0.86322
	γ_1	-0.08861	0.02853	0.13148	0.00000	-0.26309	-0.19697
	γ_2	0.67489	0.12893	-0.17328	0.00000	-0.55221	0.20866
	ϕ	0.00000	0.00000	0.00000	-1.00000	0.00000	0.00000
	ν	3145.3	1880.6	1359.0	878.3	811.7	i1934.6
MP2/DZP							
		1	2	3	4	5	6
	R	0.42666	0.22213	0.04202	0.00000	0.39740	-0.37518
	r_1	-0.11103	0.34944	-0.09519	0.00000	-0.03023	0.03794
	r_2	0.26333	0.31335	1.10090	0.00000	0.14682	0.76382
	γ_1	-0.05392	0.02991	0.14695	0.00000	-0.14249	-0.17808
	γ_2	0.46998	0.03965	-0.22275	0.00000	-0.31183	0.20270
	ϕ	0.00000	0.00000	0.00000	-0.80007	0.00000	0.00000
	ν	3266.6	1848.7	1506.5	907.4	861.5	i2064.8

[a] Harmonic frequencies are in cm^{-1}.

Table VIII. Spectroscopic constants for H_2, D_2 and CO[a,b]

	ω_e	$\omega_e x_e$	$\tilde{B}_e$	$\tilde{D}_e$	α_e
H_2	4395.20	117.91	60.81	0.04648	2.993
D_2	3118.50	64.10	30.492	0.01159	1.0492
CO	2170.21	13.461	1.9314	6.43×10^{-6}	0.01749

[a] From ref 27.
[b] Units in cm^{-1}.

Chapter IV
IR, Raman Spectra and Dynamics of Formic Acid Dimer

1 Introduction

The formic acid dimer is one of the simplest examples of a molecular entity held together by two hydrogen bonds.[1-5] As such, it has been the subject of a rather large number of experimental[6-20] and theoretical[21-37] studies. Particularly noteworthy are the classic 1958 infrared study of Millikan and Pitzer[10] and two definitive investigations (1982, 1986) of the Raman spectrum by Bertie and co-workers.[15,16] Some of these previous studies investigated the geometrical changes[9,34] between monomer and dimer and the energetic stabilization[17,18,20,23,28,34] of the dimer due to hydrogen bond formation. Others were primarily concerned with the double hydrogen atom transfer in formic acid dimer along the double well potential.[21,22,27,29-33] Since hydrogen atom transfer plays an important role in many chemical and biological systems, the knowledge of the total energies and geometries, as well as the vibrational frequencies of the equilibrium and transition state, is indeed very important to the understanding of such dynamical processes.

Among the experimental studies, the geometry of the monomer has been thoroughly investigated with various techniques such as infrared[38,39] and microwave[40,41] spectroscopy and electron diffraction.[9] The experimental determination of the equilibrium dimer structure is based on electron-diffraction measurements. Infrared and Raman spectra pertaining to the equilibrium between monomer and dimer have also been reported.[10-16] Some of these vibrational motion investigations of the dimer were restricted to the study of the O–H stretching mode[13,14,16] since this stretching mode is subject to a double minimum potential and has evoked siginificant research

interest.

On the other hand, numerous theoretical studies with *ab initio* quantum chemical methods have been carried out at various levels to predict the structures of the dimer and the potential surface for the double-hydrogen-atom-transfer process. However, most of the geometries used in the potential surface calculation were deduced from experimental[21] data or not fully optimized.[22,27,31] For example, Mijoule[36] and his co-workers reported the equilibrium and transition-state structures at the 6-31G level with gradient optimization, but they assumed the O–H···O bond angle to be 180°.

Here, we use various levels of quantum chemistry methods to perform a more thorough investigation which covers some of the interesting aspects of the formic acid dimer. Particularly, three different basis sets, i.e., minimum (STO-3G), double–ζ (DZ), and doubl–ζ plus polarization (DZ+P) are used within the Self-Consistent-Field (SCF) level of theory to study the following: (1) the change of the geometry and the shift of vibrational frequencies from formic acid monomer to the equilibrium dimer due to the formation of the two hydrogen bonds, (2) the stabilization energy of the dimerization process, (3) the variation of the vibrational frequencies and Infrared intensities among a few isotopomers of the equilibrium formic acid dimer, (4) the Raman intensities. The comparisons with the experiments are also presented if they are available. Section 2 briefly describes the theoretical approach of the SCF method and sections 3 to 6 present the results.

Ab initio calculations pertaining to the study of the double-hydrogen-atom-transfer reaction are presented in section 7. The optimized geometry and vibrational frequencies at the transition state are obtained also with the SCF method and the results are shown in section 7.1. Since the tunneling dynamics (a pure quantum mechanical phenomenon which is important at lower temperature) depends very much on the potential barrier height, higer level *ab initio* calculations which include electron correlation energies have to be performed. In section 7.2, we recalculate the

optimized geometries, frequencies and total energies of the equilibrium and transition state dimer with MP2/DZP approach. In section 8, a few preliminary studies of the tunneling dynamics of double hydrogen transfer process are presented. A new version of the empirical valence bond approach which uses normal mode harmonic potentials is also suggested in section 8 for describing global potential surfaces of systems such as formic acid dimer. Section 9 concludes.

2 Theoretical Approach with SCF Method

The geometries of the formic acid monomer (C_s structure), equilibrium dimer (C_{2h} structure), and dimer transition state (D_{2h} structure) have been fully optimized by the energy gradient method without setting any constraints on the bond angles and bond lengths. As demonstrated by the vibrational analyses, all three structures turn out to be planar. The basis sets used were minimum (STO-3G), double-ζ (DZ), and double-ζ plus polarization (DZ+P). The DZ basis set is that of Huzinaga and Dunning,[42] which consists of (9s5p/4s2p) on carbon and oxygen and (4s/2s) on hydrogen. For the DZ+P basis set polarization functions, a single set of d functions for each heavy atom and a single set of p functions for each hydrogen atom were added to the corresponding DZ basis set. The polarization function exponents were $\alpha_d(\mathrm{C}) = 0.75$, $\alpha_d(\mathrm{O}) = 0.85$, and $\alpha_p(\mathrm{H}) = 0.75$. The DZ+P basis set for the formic acid dimer includes 116 constracted Gaussian functions.

With use of analytic SCF second-derivative techniques,[43] all quadratic force constants and the resulting harmonic vibrational frequencies were determined. The presence of a single imaginary vibrational frequency for the D_{2h} structure proves that it is a true transition state.

3 Molecular Structures from SCF Method

The optimized geometries for monomer, equilibrium dimer, and dimer transition state are illustrated in Figures 1–3. Table I reproduces the theoretical geometries of the monomer at all three levels of theory together with the most reliable experimental structure. As shown in Table I, the theoretical geometries are all in reasonable agreement with experiment. Perhaps the only major structural error occurs at the SCF/DZ level of theory. There the C–O–H bond angle(115.3°) is predicted to be 9.0 deg larger than experiment. This is a common failure of the SCF/DZ method, occuring regularly for angles about oxygen.[44]

The theoretical geometries for the equilibrium dimer as well as that from electron-diffraction measurements[9] are listed in Table II. Comparisons between Table I and Table II show that there are some structural changes due to the formation of hydrogen bonds. For examples, the C=O double bond is longer in the dimer than in the monomer, whereas the C–O single bond shows opposite trend. Comparing theoretical geometries for the dimer with data from electron diffraction measurements, one sees generally good agreement. Specifically, the differences between the SCF/DZ+P structure and the experimental bond distances are as follows: –0.018 Å (C=O), –0.020 Å (C–O), –0.067 Å (O–H), +0.083 Å (O–H···O). The bond angle differences are –0.3° (O–C=O) and +0.25° (C–O–H).

Since the experimental structure of the transition state dimer is not obtainable, only theoretical results are available. As expected, the previously single bonded C–O distance is shorter for the transition state than for the equlibrium dimer. Comparison between this transition state bond length and the C=O and C–O bond lengths shows that it is characteristic of bond order one and a half. Interestingly, the O···O and C···C distances are found to be shorter for the D_{2h} structures.

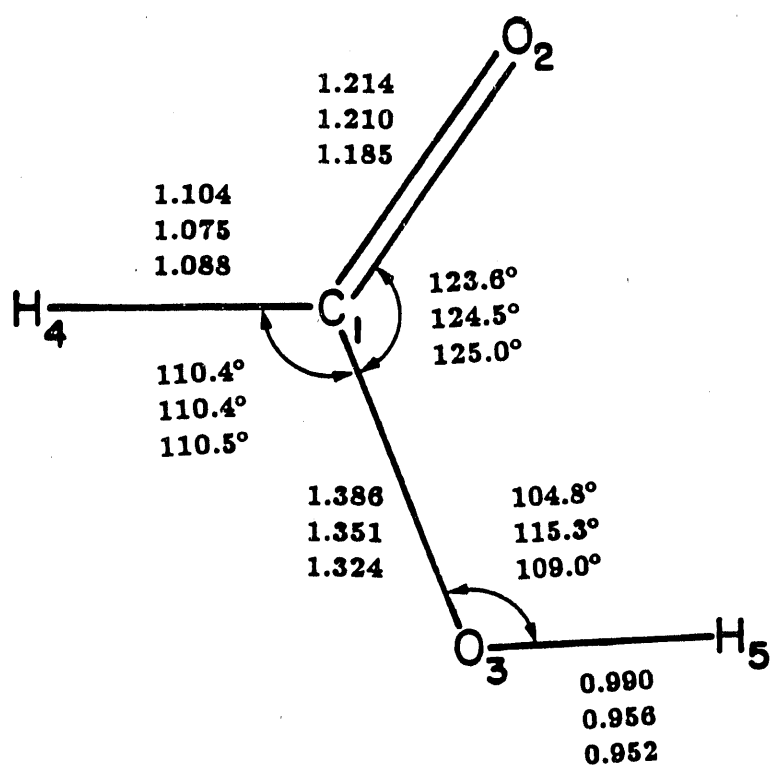

Figure 1: Predicted equilibrium geometries for the formic acid monomer. Bond distances are given in Å. Three levels of self-consistent-field theory are reported for each geometrical parameter.

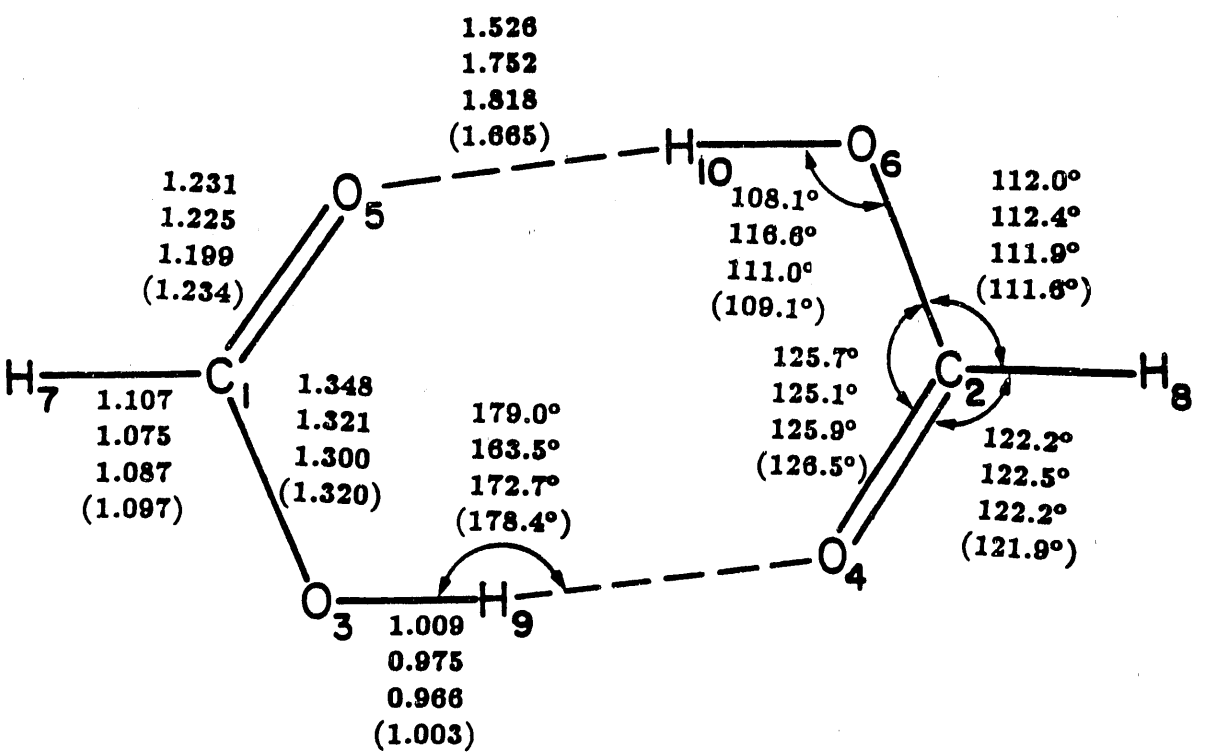

Figure 2: Same as Figure 1, except it is for the predicted geometries for the formic acid equilibrium dimer and the results from the MP2/DZP are shown with parentheses.

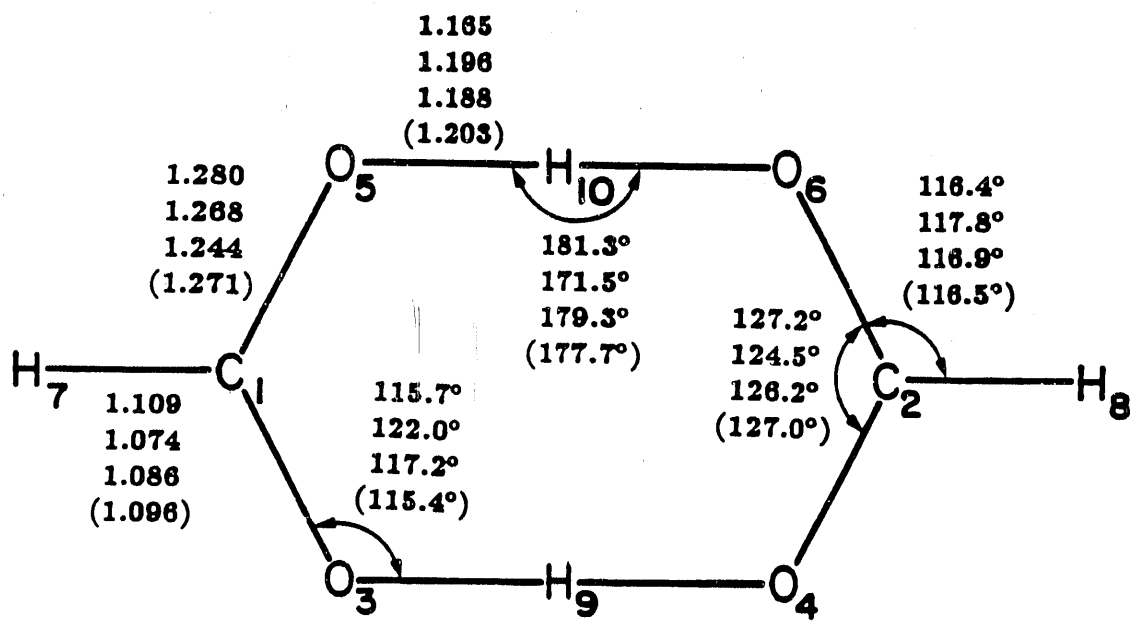

Figure 3: Same as Figure 1, except it is for the predicted geometries for the formic acid transition state dimer and the results from the MP2/DZP are shown with parentheses.

4 Vibrational Frequencies and IR Intensities

4.1 $(HCOOH)_2$ Molecule

Table III–V give the harmonic vibrational frequencies, IR intensities, and normal mode assignments of the molecules studied here. The conventions of Bertie[15,16] were adopted in describing the normal modes. The designations "oop" and "ip" refer to out-of-plane bending and in-plane bending.

It is not surprising[45] that the predicted frequencies from DZ and DZ+P for the monomer and C_{2h} dimer are consistently higher than the observed data. The absolute and relative difference between SCF/DZ+P harmonic frequencies ω and the observed monomer fundamentals ν are 547 cm^{-1} = 15.3% (ν_1), 351 cm^{-1} = 11.9% (ν_2), 238 cm^{-1} = 13.4% (ν_3), 155 cm^{-1} = 11.2% (ν_4), 203 cm^{-1} = 16.6% (ν_5), 164 cm^{-1} = 14.9% (ν_6), 65 cm^{-1} = 10.4% (ν_7), 150 cm^{-1} = 14.5% (ν_8), and 51 cm^{-1} = 7.9% (ν_9). These differences are due to[45] a combination of (1) the tendency of the SCF/DZ+P method to overshoot the true harmonic vibrational frequencies and (2) the contributions of anharmonicity; generally speaking $\omega_i > \nu_i$ and anharmonicity corrections of 5 % are not unusual.

The classic paper by Millikan and Pitzer[10] labels the dimer infrared intensities as s (strong), m (medium), w (weak), etc. For several of the normal modes, more quantitative information concerning the IR intensities has been given by Marechal.[14] Since the IR intensities have been quantitatively predicted from theory here, an interesting comparison in Table IV is possible. Note, of course, that all A_g and B_g normal modes have zero IR intensity in the "double harmonic" approximation used here. The three greatest IR intensities are predicted theoretically for ν_{17} (1575 km/mol), ν_{19} (1188 km/mol), ν_{22} (478 km/mol). It is most encouraging that ν_{17}, ν_{19}, and ν_{22} are three of the four frequencies designated "very strong" by Millikan and Pitzer.[10] We predict a significant but smaller intensity (156 km/mol) for the

fundamental ν_{18} labeled very strong by Millikan and Pitzer. A designation of simply "strong" would have been more consistent with the *ab initio* predictions.

The fourth highest theoretical IR intensity (ν_{14}, 357 km/mol) is labeled "strong" by Millikan and Pitzer.[10] This is followed by ν_{23} (85 km/mol) and ν_{21} (75 km/mol), both designated "medium" from the observed IR spectrum. ν_{24} is predicted from SCF/DZ+P theory to have an intensity of 48 km/mol, a bit less than expected from Millikan and Pitzer's label "strong". The remaining four fundamentals are predicted to have IR intensities less than 20 km/mol (SCF/DZ+P). Those weak intensities concur with the experimental labels,[10,12] except for ν_{15}, which is designated "medium" by Millikan and Pitzer. A success for theory is that among modes with nonvanishing IR intensity, the vibrational frequency with weakest intensity is ν_{13} (1050 cm^{-1}) for which $I = 0.4$ km/mol (SCF/DZ+P). This is in fact the one fundamental (among $\nu_{13} - \nu_{24}$) above 200 cm^{-1} that was not observed as a well defined feature by Millikan and Pitzer.[10]

Except for two low-frequency vibrations, all the SCF/DZ+P harmonic frequencies ω lie above the corresponding observed fundamentals ν. The two exceptions are the O···O stretch (SCF/DZ+P $\omega_8 = 182$ cm^{-1}, $\nu_8 = 190$ cm^{-1}) and the O–H···O in-plane bending vibration (SCF/DZ+P $\omega_{24} = 223$ cm^{-1}, $\nu_{24} = 248$ cm^{-1}). Although the theoretical frequencies fall slightly below the experimental fundamentals, the absolute agreement is excellent. These two modes, O···O and O–H···O, are among the most sensitive to the theoretical description of the HCOOH···HCOOH interaction.

Perhaps more interesting than the vibrational frequencies themselves are the frequency shifts between dimer and monomer. These shifts are displayed in Table V. One sees in Table V that two critical pieces of experimental information are missing, namely $\Delta\nu(\nu_1)$ and $\Delta\nu(\nu_{11})$, predicted by theory to be two of the four largest frequency shifts. However, the remainder of the comparisons between theory and

experiment leave little doubt that theory is qualitatively reliable in these predictions.

Not surprisingly, the largest shifts occur for the O–H frequencies. The antisymmetric dimer O–H stretch ν_{17} is known[15] to be 459 cm^{-1} less than that for the isolated monomer, and theory predicts an even larger shift for the symmetric OH stretch ν_1. The simple explanation, of course, is that the formation of two strong hydrogen bonds in the dimer weakens the two O–H single bonds. In the limit of the D_{2h} transition state, the four O–H linkages become indistinguishable.

The next largest dimer-monomer vibrational shift occurs for ν_{14}, the in-phase combination of monomer out-of-plane O–H bending modes. This large shift is +276 cm^{-1} from experiment,[15] with SCF/DZ+P theory predicting +292 cm^{-1}, in good agreement. The comparable out-of-phase combination of oop O–H bending frequencies is not known from laboratory studies, but it should be close to the predicted $\Delta\nu(\nu_{11})$ = +242 cm^{-1}. These vibrational frequencies increase in the formic acid dimer, because the formation of the two hydrogen bonds has the effect of causing the monomers to become much more rigidly planar. That is, the nonplanar excursions of the O–H are now not only accountable to the singly bonded formyl group (HCO) but also to the partner monomer.

A significant dimer-monomer vibrational frequency shift also occurs for ν_4, the symmetric combination of in-plane H–O–C bending frequencies. For the reasons discussed in the previous paragraph, these vibrational modes are shifted to higher frequency in the dimer. SCF/DZ+P theory does not do terribly well in predicting this shift: $\Delta\nu(\nu_4)$ = +135 (theory) and +193 cm^{-1} (experiment). Further theoretical work will be necessary to ascertain whether these discrepancies are due to (1) an inadequate description of the potential energy surface, in which case the true harmonic shifts $\Delta\omega$ would be closer to $\Delta\nu$, or (2) neglect of important anharmonic effect.

Insight into the problem between theory and experiment for ν_4 is given by the

analogous comparisons for ν_{20} and ν_{21}. For these two shifts SCF/DZ theory seems to be doing a reasonable job, while the higher level SCF/DZ+P method does very poorly compared to experiment. The reason is that the separation between H–C–O and H–O–C bending modes is rather murky. Specifically, Bertie and Michaelian[15] identify the higher of these two B_u modes as H–O–C bending. This is consistent with the SCF/DZ potential energy distributions (PED's). However, in the SCF/DZ case the weightings are quite close, being 0.52 (H–O–C) and 0.36 (H–C–O). At the SCF/DZ+P level, the PED's reverse to give 0.71 (H–C–O) and 0.23 (H–O–C). Furthermore, since ν_{20} and ν_{21} are only separated by 85 cm^{-1} experimentally, one cannot be certain that the experimental designations of Bertie and Michaelian are unambigous. The best way to think about ν_4 and ν_5 and about ν_{20} and ν_{21} is that they are strongly interacting combinations of the H–C–O and H–O–C bending modes. This is, of course, confirmed by the accepted assignment that for the monomer the H–C–O bend lies higher, while for the A_g dimer vibrations the H–O–C bend lies higher.

Further insight into the assignments for ν_{20} and ν_{21} is possibly given by examination of the IR intensities. For the formic acid monomer, theory and experiment agree that the H–O–C bend has a higher IR intensity and lower fundamental frequency than the H–C–O bend (SCF/DZ+P: $I(4) = 10$ km/mol, $I(5) = 26$ km/mol). To the extent that the monomer results may be used to anticipate the dimer intensities, one would thus expect the H–O–C bending assignment to go to the lower dimer vibrational frequency with higher IR intensity. This is precisely what is predicted by SCF/DZ+P theory, but it is opposite to the experimental assignments.

The C–O single bond stretching frequencies are shifted upward by ~ 110 cm^{-1} in the dimer, and DZ+P SCF theory does a good job in reproducing this trend. Inspection of Figure 2 shows that the C–O single bonds are next-nearest neighbors to the H$\cdots$O hydrogen bonds and take on a small amount of "conjugation" or double

bond character upon dimer formation.

Perhaps most widely discussed among the formic acid dimer vibrations are the C=O double bond stretching frequencies. A recent paper by Dybal, Cheam, and Krimm[46] discusses in great detail the origin of the splitting between the symmetric (ν_3 = 1670 cm^{-1}) and antisymmetric (ν_{19} = 1754 cm^{-1}) components of the C=O stretch mode. This shift of 84 cm^{-1} between C=O dimer modes is predicted to be (1983 - 1927) = 56 cm^{-1} at the SCF/DZ+P level of theory. With the SCF/4-31G method Morokuma and co-workers[33] predicted 44 cm^{-1} for this shift. Karpfen predicts 58 cm^{-1} for this dimer shift in his *ab initio* study[34] using a small double-ζ basis set in conjunction with SCF theory. The three sets of *ab initio* harmonic vibrational frequencies are consistent with the conclusion of Dybal, Cheam and Krimm[46] that the remaining discrepancy (84 - 56 = 28 cm^{-1}) may be due to a difference in anharmonicity between the A_g and B_u modes.

It is encouraging that the smaller dimer-monomer vibrational frequency shifts are also treated in a reasonable manner by the present theoretical methods. For example, the symmetric combination of C–H stretches is predicted to be 10 cm^{-1} higher in the dimer, while the experimental shift is +7 cm^{-1}. In fact the *sign* of every known dimer-monomer vibrational frequency shift is properly predicted with SCF/DZ+P theory. SCF/DZ theory fails once, for ν_{18}, the asymmetric combination of C–H stretches. In that case $\Delta\omega$(SCF/DZ) = -2 cm^{-1}, $\Delta\omega$(SCF/DZ+P) = +7 cm^{-1}, and $\Delta\nu$(exptl) = +15 cm^{-1}.

Finally, a brief comparison of the dimer and monomer IR intensities is in order. Based strictly on the formic acid monomer results (Table III), one would expect the dimer C=O stretch (monomer intensity 533 km/mol) to be strongest, followed by the C–O single bond stretch (301 km/mol) and then by the O–H stretch (116 km/mol for the monomer; SCF/DZ+P level of theory). Although these three modes do have the largest IR intensities among the B_u dimer fundamentals, the order is different.

That is, the O–H stretch has the highest IR intensity (1575 km/mol) and the C–O single bond stretch the lowest (478 km/mol) of the three. Since the IR intensity is proportional to the square of the change in the dipole moment with respect to the appropriate normal coordinate, $(\delta\mu/\delta Q)^2$, the order of dimer IR intensities is not trivially deduced from those of the formic acid monomer.

4.2 $(HCOOD)_2$ Molecule

The theoretical predictions concerning the IR spectra of HCOOD and $(HCOOD)_2$ are summarized in Tables VI and VII. All monomer and dimer assignments are the same as those given from experiment by Bertie, Michaelian, Eysel, and Hagel.[16] It is also encouraging that every predicted SCF/DZ+P harmonic frequency except ν_{24} lies above the analogous observed fundamental. In the case of ν_{24} the absolute agreement is still quite good, with ω(SCF/DZ+P) = 218 cm^{-1} and ν(expl) = 240 cm^{-1}.

With two exceptions, the dimer–monomer vibrational frequency shifts agree quite well with experiment. The predicted A_g SCF/DZ+P dimer-monomer shift for the D–O–C bend is somewhat disappointing, being +70 cm^{-1}, while experiment shows no shift. We might be inclined to blame this on a poor description of the H–C–O and D–O–C mixing, but (1) these are now rather well separated by the deuterium substitution and (2) theory does quite well for the H–C–O shift from monomer to dimer.

The serious disagreement between theory and experiment occurs for the O–D stretching frequency ν_{18}, which Excoffon and Marechal[13] have assigned at 2068 cm^{-1}. The SCF/DZ+P ω_{18} is 35.1 % greater than experimental ν_{18}. This is clearly unreasonable and we are forced to conclude that the true ν_{18} must be significantly higher. We suggest that it is extremely unlikely that ν_{18} is less than 2200 cm^{-1}. Thus it

seems clear that Excoffon and Marechal have made a misassignment.

However, that the present results are based on the harmonic approximation while in ref.13 an attempt was made to include strong anharmonic couplings. As the main effect of these anharmonicities is to broaden the O–D stretching band, it may be reasonable to compare frequencies appearing in an harmonic frame with band centers of these broad anharmonic bands and not with the peculiar transition labeled 0000. In Table II of ref.13 this band center falls at 2281 cm^{-1}, which seems to fit in with the present theoretical predictions.

The theoretical IR intensities for $(HCOOD)_2$ may be compared with the qualitative experimental labels assigned by Millikan and Pitzer.[10] Theoretically, the strongest fundamental is predicted to be ν_{19}, the B_u C=O stretch, for which an intensity of 1129 km/mol is seen in Table VII. This prediction fits perfectly with Millikan and Pitzer's identification of ν_{19} as the only "very strong" fundamental. The second strongest theoretical vibration is ν_{18}, the O–D stretch, for which 891 km/mol is predicted, perhaps surprising considering the above–discussed misassignment of ν_{18}. However, if one looks at Figure 1b of the paper by Excoffon and Marechal,[13] it is clear that there is an intense IR band peaking at ~2300 cm^{-1}. Thus, although the correct assignment of ν_{18} was long concealed, the existence of an IR band of high intensity (consistent with the SCF/DZ+P prediction I = 891 km/mol for ω_{18}) is indisputable. Our third strongest fundamental is ν_{21} (371 km/mol), the C–O single bond stretch, and it is encouraging that this band is the only one designated "strong" by Millikan and Pitzer.[10] The four fundamentals (ν_{17}, ν_{20}, ν_{22}, and ν_{23}) experimentally labeled "medium" intensity by Millikan and Pitzer are predicted here to have intensities in the range 50–102 km/mol and thus the agreement is superb.

Three of the experimental $(HCOOD)_2$ fundamentals in Table VII were assigned by Carlson, Witkowski, and Fateley[11] from the far-infrared spectrum. Clearly these intensities fall on a different absolute scale than those of Millikan and Pitzer.[10]

Nevertheless, the relative ordering vs (ν_{24}) , s (ν_{15}), and m (ν_{16}) agrees perfectly with the *ab initio* intensities, which are 46, 11, and 4 km/mol, respectively.

4.3 $(DCOOH)_2$ Molecule

Tables VIII and IX give theoretical and experimental information pertinent to the infrared spectra of DCOOH and its dimer. Although seven fundamentals of the dimer are yet unobserved, all 17 known (anharmonic) frequencies lie below the corresponding SCF/DZ+P harmonic frequencies.

Again the *ab initio* IR intensities agree well with the experimental descriptions of Millikan and Pitzer.[10] The three most intense fundamentals in the IR are predicted to be the O–H stretch ω_{17} (1599 km/mol), the C=O stretch ω_{19} (1191 km/mol), and the C–O single bond stretch ω_{21} (389 km/mol). These are the only three fundamentals labeled "strong" by Millikan and Pitzer. Similarly, the C–D stretch is predicted to have substantial intensity (199 km/mol) and is labeled appropriately "ms" in the experimental analysis.

Table IX shows that there is a reversal in the theoretical and experimental descriptions of the A_u vibrations ν_{13} and ν_{14}. In the theoretical analysis ν_{13} is clearly the out-of-plane C–D bending motion. In contrast Bertie, Michaelian, Eysel, and Hager identify the higher frequency of ν_{13} and ν_{14} as the out-of-plane O–H bend. The experimental difference $(\nu_{13} - \nu_{14}) = 40$ cm^{-1} is, however, reasonably predicted by theory, which finds $(\omega_{13} - \omega_{14}) = 31$ cm^{-1}.

The experimental dimer–monomer vibrational frequency shifts (where available) are in general well-reproduced by SCF/DZ+P theory. The only disappointment occurs for ν_{17}, the dimer O–H stretch, which is predicted to be 282 cm^{-1} lower than the monomer O–H stretch. In constrast the experimental shift is much greater, namely (3098 – 3566) = –468 cm^{-1}. As noted earlier, an error of the same magnitude

is made by SCF/DZ+P theory for the $(HCOOH)_2$ species. Future theoretical studies would do well to pursue the source or sources of these rather significant errors.

4.4 $(DCOOD)_2$ Molecule

Comparable theoretical and experimental results for the per-deuteriated species DCOOD and $(DCOOD)_2$ are summarized in Tables X and XI. One sees immediately in Table X a disagreement between the SCF/DZ+P methods and experiment concerning the monomer assignment of ν_5 and ν_6, the D–C–O and D–O–C bending motions. From theory the higher of the two frequencies is assigned to the D–O–C bend. However, the assignment is marginal, with the PED's being 0.40 (D–O–C) and 0.20 (D–C–O) for ω_5. Bertie and Michaelian[15] instead assign ν_5 to the D–C–O bending motion. Interestingly, the theoretical difference $(\omega_5 - \omega_6) = 84$ cm^{-1} agrees quite well with the experimental $(\nu_5 - \nu_6) = 97$ cm^{-1}.

It is not surprising, in light of the monomer D–C–O and D–O–C assignments, that the SCF/DZ+P dimer assignments are not identical with those based strictly on experimental observations. The fact that these assignments are not trival is seen in footnote *e* of Table I in the paper by Bertie and Michaelian,[15] who state that ν_{21} and ν_{22} are a mixture of the D–O–C and D–C–O deformations. In fact theory and experiment *agree* for the assignment of ν_{21} (D–O–C) and ν_{22} (D–C–O). However, as seen in Table XI, there is a disagreement for ν_5 and ν_6. The SCF/DZ+P PED's identify ν_5 as the D–O–C bend, while Bertie and Michaelian prefer the D–C–O deformation. Again, however, theory and experiment are in good agreement concerning difference in frequencies: $\Delta\omega(5-6) = 105$ cm^{-1}; $\Delta\nu(5-6) = 91$ cm^{-1}.

The C=O stretch ν_{19} is predicted here to have the highest infrared intensity, namely 1139 km/mol. It is encouraging that this is also the strongest fundamental ("very strong") in the designations of Millikan and Pitzer.[10] The next strongest

IR fundamental, from theory, should be the O–D stretch ν_{17} (849 km/mol). However, we find no acceptable experimental identification of this fundamental. Bertie and Michaelian[15] cite Excoffon and Marechal for ν(O–D) = 2068 cm^{-1}, but this is apparently from $(HCOOD)_2$, for which the O–D should admittedly be comparable. However, we have already shown that the latter assignment of Excoffon and Marechal must be incorrect. Millikan and Pitzer assign ν_{17} (O–D) = 2323 cm^{-1}, and this is certainly closer to the truth than 2068 cm^{-1}. The remaining fundamentals labeled "strong" by Millikan and Pitzer are (in order of theoretical intensity, with SCF/DZ+P values in parentheses) ν_{20} (C–O, 321 km/mol), ν_{18} (C–D, 204 km/mol), ν_{14} (δO–D oop, 195 km/mol), ν_{22} (D–C–O, 88 km/mol), and ν_{23} (O–C=O, 90 km/mol). The fundamentals labeled "weak" all have significant smaller SCF/DZ+P IR intensities. Thus one sees again an essentially perfect correspondence between theoretical and experimental IR intensities.

5 Raman Intensities

Bertie and co-workers[15,16] have carried out definitive experimental studies of the Raman spectra of formic acid and its dimer, and they include in their papers considerable information concerning the Raman intensities. In the present theoretical study we define the Raman intensity following Gussoni[47] as

$$I = 45\alpha'^2 + 7\gamma'^2 \qquad (1)$$

where α' and γ' are the derivatives of the trace and anisotropy of the polarizability, respectively. The depolarization is then defined as[47]

$$\rho = 3\gamma'^2 / \left[45\alpha'^2 + 4\gamma'^2\right] \qquad (2)$$

The theoretical Raman intensities reported here were obtained with use of recently developed analytic method.[48] Since Raman intensities can be quite sensitive to basis set choice,[49,50] only the SCF/DZ+P results are reported here.

The predicted Raman intensities for the HCOOH monomer are compared with experiment in Table XII. There the theoretical predictions are seen to be generally helpful. Specifically, the two fundamentals (ν_5 and ν_8) not observed in the Raman and the one labeled questionable (ν_9) by Bertie and Michaelian[15] have the lowest theoretical Raman intensities, 0.9–1.2 Å^4/amu. Thus theory "explains" the difficulty of observing these fundamentals in the Raman spectrum. Furthermore the next two highest intensity Raman fundamentals (ν_6 and ν_7) hold this position according to either the theoretical or experimental intensities. A disappointment in the theoretical Raman intensities is their failure to show ν_1 and ν_3 having comparable intensities — SCF/DZ+P theory predicts $I(\nu_1)$ to be nearly six times more intense than $I(\nu_3)$.

The formic acid dimer Raman intensities are summarized in Table XIII. The allowed Raman fundamental predicted to have lowest intensity is ν_8, corresponding to the O$\cdots$O motion. This theoretical prediction fits well with the fact that ν_8 has not yet been observed in the Raman spectrum.[15] Two other Raman fundamentals are predicted by SCF/DZ+P theory to have intensities less than 1 Å^4/amu. Of these two frequencies ν_9 (A_g) has been observed in the Raman, while ν_{11} (B_g) has not to date been identified.

The Raman fundamental with highest theoretical intensity (ν_2, 203 Å^4/amu) is also found in the laboratory to have the greatest Raman intensity (100 counts/s). However, the second most intense Raman fundamental is predicted by theory to be

ν_1, the O–H stretch, at 147 Å^4/amu , and ν_1 is not observed at all in the laboratory. The non-identification of ν_1 is discussed in some detail in the paper by Bertie and Michaelian.[15] To summarize their conclusions, there are broad features in the expected region of the Raman spectrum, but these are muddled by the likely presence of overtone and combination bands, making the analysis treacherous. Of course, the mixing of ν_1 with overtones and combinations is not accounted for in the simple harmonic approximation adopted in the present theoretical study.

There is a reasonable correspondence between theory and experiment for the Raman depolarization ratios of the formic acid dimer. For example, the three smallest depolarization ratios occur for ν_6, ν_3, and ν_2 both theoretically and experimentally. Note that the B_g depolarization ratios do not provide a test of the theory since these are required by symmetry to be precisely 3/4. However, there are four Raman fundamentals with nontrivial experimental depolarization ratios in the range 0.4–0.75, and these are predicted by theory to be 0.49–0.70. We conclude that theoretical predictions of depolarization ratios at this level can be reliable and may be very helpful in the future in interpreting complicated Raman spectra.

Although not reported here, SCF/DZ Raman intensities for $(HCOOH)_2$ are generally within a factor of 2 of the DZ+P predictions, but they provide a poorer correspondence with the experimantal intensities.

6 Energetics of the Dimerization Reaction

Total and relative energies for formic acid and its dimer are reported in Table XIV. The only piece of energetic information available from experiment concerns the dissociation energy for the process

$$(HCOOH)_2 \longrightarrow 2HCOOH \qquad (3)$$

The most widely cited experimental value for ΔH is that reported by Clague and Bernstein[17] in 1969, namely 14.8 ± 0.5 kcal/mol. Earlier experimental dimerization energies fall in the range 15.2 – 18.0 kcal/mol and are discussed in the classic monograph by Pimentel and McClellan.[1] Clague and Berstein[17] used the ratio of infrared intensities of the dimeric to monomeric O–H stretching vibrations to determine the equilibrium constant for Eq.(3) and hence the dissociation energy. A related but independent experimental study, also appearing in 1969, was that of Mathews and Sheets,[51] who reported ΔH_{300} = 14.1 ± 1.5 kcal/mol.

In early 1987, Henderson reported a new value of the dimerization of formic acid based on Fourier transform infrared spectroscopy.[52] Henderson reports $\Delta H(1)$=11.7 ± 0.1 kcal/mol. Although we are a bit skeptical concerning the very narrow error bars associated with this new experimental dimerization energy, the fact that the experiment is sufficiently simple to be suitable for undergraduates to carry out as coursework is very impressive. Possible support for the experiment of Henderson[52] is the recent NMR study of Lazaar and Bauer,[20] who conclude that ΔE_0 for formic acid dimer dissociation is no more than 12 kcal. These authors also suggest that

$$D_0 = \Delta H_0 \simeq \Delta H_{300} - 1.5 \text{ kcal} \tag{4}$$

We have evaluated ΔH_{300} *ab initio* (see Table XIV) and find it to be 0.2 kcal larger than D_0 at the SCF/DZ+P level of theory.

As Table XIV shows, the formic acid dimer has significantly more zero-point vibrational energy (ZPVE) than do two monomers. At the highest level of theory this ZPVE correction is 2.0 kcal/mol. In this way SCF/DZ+P theory predicts D_0 = 12.3 kcal/mol for the dimerization energy. Although such hydrogen bond energies are not in general known with great precision from experiment, SCF/DZ+P theory

does agree satisfactorily with the available data for systems such as the water and hydrogen fluoride dimers.[53] In fact the SCF/DZ+P value D_0 = 12.3 kcal is quite consistent with the Lazaar-Bauer result ($\leq$ 12.0 kcal) when one realizes that the reliability of this level of theory is of the order of 1 kcal/mol for such dissociation energies. The DZ basis set predicts D_0 = 16.8 kcal, clearly larger than experiment, as is also the case for the H_2O and HF dimers.[53] In constrast, the minimum basis set SCF method does a good job of reproducing (to within 0.3 kcal) the more realiable SCF/DZ+P result. The reader should recall, of course, that the minimum basis set does not do superbly well in predicting the equilibrium geometrical structure of the dimer.

SCF/DZ+P theory predicts ΔH_{300} = 12.5 kcal/mol, to be compared with the experimental values 14.8, 14.1, and 11.7 kcal, respectively.[17,51,52] Considering the broad range of experimental dissociation energies, the theoretical prediction is quite satisfactory.

7 Energetics of the Double Hydrogen Transfer Reaction

To study the isomerization reaction (shown in Eq.(5)) which involves the double hydrogen atom transfer within the formic acid dimer, one needs the preliminary information such as the geometry, harmonic force field of the transition state and the reaction barrier height.

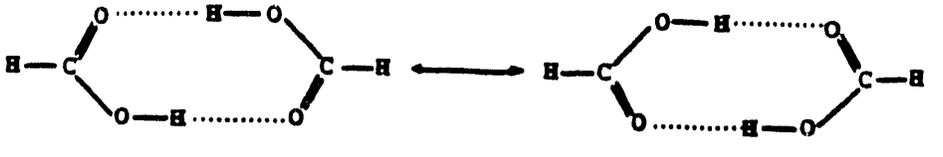

(5)

Since no "experimental" data at the transition state and the barrier height are available. One can only obtain these information through *ab initio* quantum chemistry. Section 7.1 presents the results from SCF calculations and section 7.2 gives a further investigation using higher level *ab initio* methods which includes the effect of electron correlations.

7.1 Results from SCF Method

The predicted transition state geometries with the three SCF level calculations were presented previously in section 2 and shown in Figure 3. Table XV gives the vibrational frequencies and IR intensities for transition state obtained with DZ and DZ+P basis sets. As expected, the single imaginary vibrational frequency (negative force constant in terms of normal coordinates) corresponds to the out-of-phase combination of O–H stretching motions. The frequency 1695i from the SCF/DZ+P calculation seems to be indicative of a substantial barrier height, which is shown in Table XVI to be 15.6 kcal/mol. Noteworthy is the variation of the barrier heights with the basis sets. At the STO-3G level, it is predicted to be 5.2 kcal/mol, about 10 kcal/mol lower than the higher level DZ+P calculation. Since the tunneling dynamics is sensitive to reaction barrier height, further investigation with more sophisticated approach is required in order to obtain the "true" value.

7.2 Results from Moller-Plesset Method

Among all the high level *ab initio* methods, the Moller-Plesset perturbation approach[54] provides an inexpansive way of including the electron correlations which contribute to the potential energies. The program codes used are those from CADPAC[55] or Gaussian88[56] and the calculations are carried out either in Cray/XMP or Cray2 machines. The geometries of the equilibrium dimer and dimer transition state have

been fully optimized by the energy gradient method at the MP2/DZ+P level of theory. The polarization function exponents used for these calculations are those suggested in CADPAC. That is, $\alpha_d(C) = 1.0$, $\alpha_d(O) = 0.90$, and $\alpha_p(H) = 0.80$. Calculation of the analytic MP2 second-derivatives for this 10 atom system takes about 4–5 CPU hours. Higher order corrections to the energies from electron correlations are obtained through the third (MP3) or fourth (MP4) order perturbation theories. A complete MP4(SDTQ) calculation of the energies is also performed and it needs roughly 2 gegabytes of disk space and 13 CPU hours in Cray2 machine. To test the effect of the size of the basis sets, the MP2/TZ2P calculations are applied to the MP2/DZP optimized geometries. The triple-ζ basis sets[57] contain 3s for the H atom, 5s4p for the first row atoms, and 9s6p for the second row atoms. For formic acid dimer, there are all together 210 basis functions.

The optimized geometries for equilibrium dimer, and dimer transition state are illustrated with parentheses in Figures 2–3. Table XVII reproduces the theoretical geometries and Table XVIII gives the vibrational frequencies for the equilibrium and transition state configurations. The total energies obtained at each levels for both configuration and the reaction bare barrier heights are presented in Table XVI. In general, there is little difference between the optimized geometries from the SCF/DZP and the MP2/DZP calculations. However, for most of the vibrational modes, the harmonic frequencies are decreased by a few percents using the MP2/DZP level of theory. This indicates that we are approaching the correct answers since the SCF/DZP theory often overestimates the frequencies by up to 15%. In fact, a better agreement of the vibrational frequencies between the MP2/DZP calculation and the experiments is found.

For the reaction barrier, one sees a sharp decrease from 15.6 kcal/mol to 6.4 kcal/mol as one moves from the SCF/DZP to the MP2/DZP method. Enlarging the size of the basis sets from DZP to TZ2P only increases the barrier by 1.5 kcal/mol.

The barrier height osciallates between a small range (6.4 to 8.55 kcal/mol) depending on the level of the correction. We believe a barrier height around 7 to 8 kcal/mol is close to the true value.

8 Tunneling Dynamics of the Double Hydrogen Transfer Reaction

The theoretical study of the reaction dynamics of polyatomic molecules is a great challenge due to the number of degrees of freedom involved. During the past 10 years also, various methods have been developed and employed in the Miller group for studying the tunneling dynamics in various systems. Among them, the simple 1-dimensional WKB method[58] provides the simplest estimation on the order of magnitude of the tunneling splitting. More accurate methods such as the reaction path Hamiltonian[59] which utilizes the minimum energy path (MEP) as the reference coordinate and the reaction surface Hamiltonian[60] which includes two large amplitude modes (LAM) as the system coordinates have been applied to the case of the single hydrogen transfer in malonaldehyde. Recently, a similar reaction path Hamiltonian[61] which is expressed in the cartesian coordinates was suggested. This new Hamiltonian has the advantages that the cumbersome kinetic coupling that occurs in the previous reaction path Hamiltonian is transformed into the potential coupling and that it is mass-independent, which makes the study of the isotope effect much easier. In the following, we apply the WKB method and the cartesian reaction path Hamiltonian approach to study the double hydrogen transfer in formic acid dimer. Then, a normal mode version of the EVB model combined with proper relative orientations among the reactant, transition state and product configurations is presented for obtaining global potential surface which will be used for future

trajectory study on this system.

8.1 Simple 1-Dimensional WKB Method

Within a simple one-dimensional symmetric double-well description of the potential, the WKB approximation gives the tunneling splitting as

$$\triangle E = \frac{\hbar\omega_F}{\pi} e^{-\theta}, \tag{6a}$$

where ω_F is the calssical vibrational frequency in one of the wells and θ is the WKB barrier penetration integral. If the barrier is approximated by an Eckart potential function[62], θ is given by

$$\theta = \frac{2\pi}{\hbar\omega_i}(V_{eff} - \sqrt{E_0 V_{eff}}), \tag{6b}$$

where V_{eff} is the effective potential barrier height, E_0 is the energy relative to the bottom of the wells, and ω_i is the imaginary frequency at top of the barrier. For the ground vibrational state,

$$V_{eff} = V_0 + \sum_{k=1}^{3N-7} \frac{1}{2}(\hbar\omega_k^* - \hbar\omega_k), \tag{6c}$$

and

$$E_0 = \frac{1}{2}\hbar\omega_F, \tag{6d}$$

where $\{\omega_k^*\}$ and $\{\omega_k\}$ are the vibrational frequencies of the remaining 3N-7 normal modes at the transition state and the equilibrium configurations.

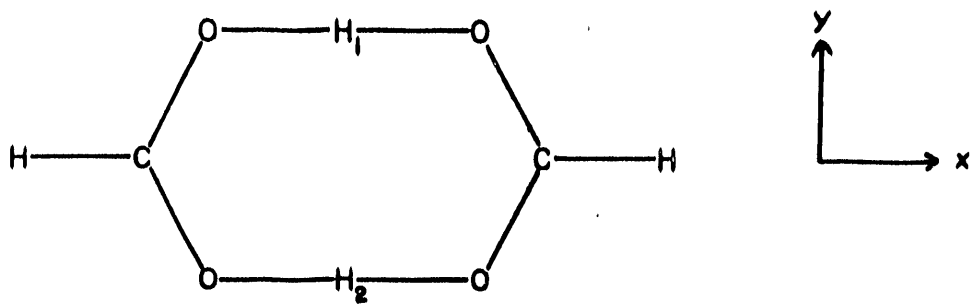

Figure 4: coordinate system used for the formic acid dimer

We carried out this calculation with the values obtained from SCF/STO-3G, SCF/DZ and SCF/DZ+P and MP2/DZP methods. The corresponding ω_F, which pertains to the O-H stretching in the reactant (and product) configuration, are 3708, 3620, 3782 and 3198 cm^{-1} and the imaginary frequencies are 1098i, 1663i, 1695i and 1199i, respectively. The bare barrier height V_0 are 5.2, 14.2, 15.56 and 6.4 kcal/mol. Using the above equations, we find the tunneling splitting of the gound vibrational state $\triangle E_0$ to be 70, 0.6, 0.3, and 66 cm^{-1}, respectively.

8.2 The Cartesian Reaction Path Hamiltonian Method

Readers are referred to ref.61 for detailed descriptions of this method. Due to the non-negligible geometry change (the relaxation) of the formic acid dimer during the double hydrogen transfer reaction, the flexible bath version of the method is used.

Since we are looking at a simultaneous double hydrogen transfer, the "system" coordinate should be a linear combination of the coordinates of the two involving H atoms. If one defines the x coordinate to be parallel to C $\cdots$ C (shown in Figure 4), the largest amplitude motion will be the motion of the two center H atoms along the x axis. Therefore, our system coordinate x_1 is defined as:

$$x_1 = \frac{1}{2}(x_{H_1} - x_{H_2}). \tag{7}$$

It describes the concerted motion of the two H atoms toward opposite directions. The proper mass m_1 for this coordinate is $2 \times m_H$.

The remaining 3N-1 coordinates (including $x_2 = 1/2(x_{H_1} + x_{H_2})$) are the bath modes, and are represented as $\mathbf{X}$. In the flexible bath version of the method, the reference geometry of the bath along the reaction path is allowed to vary with the system coordinate x_1. I.e.,

$$\mathbf{X} = \mathbf{X}_0(x_1), \tag{8}$$

the subscript "0" means it is along the reaction path.

The basic idea of this "Cartesian Reaction Path Hamiltonian" method is to make local approximation of the potential energy surface with a second order Taylor series expansion about the system coordinate x_1. The resulting Hamiltonian is

$$H(p_1, x_1, \mathbf{P}, \mathbf{X}) = \frac{1}{2m_1}p_1^2 + \frac{1}{2}\mathbf{P} \cdot \mathbf{m}^{-1} \cdot \mathbf{P} + V_0(x_1, \mathbf{X}_0(x_1))$$
$$+\frac{1}{2}[\mathbf{X} - \mathbf{X}_0(x_1)] \cdot \mathbf{K}(x_1, \mathbf{X}_0(x_1)) \cdot [\mathbf{X} - \mathbf{X}_0(x_1)] - \mathbf{f}(x_1, \mathbf{X}_0(x_1)) \cdot [\mathbf{X} - \mathbf{X}_0(x_1)]. \tag{9}$$

One of the drawbacks of the above Hamiltonian is that it contains not only the internal vibrational degrees of freedom, but also the overall translational and rotational motions. Unfortunately, if one wishes to maintain the simple form of the Hamiltonian, these motions can only be projected out in an approximate fashion.[61]

The details of the developement of the approximation can be found in the original paper. The main essences of the approximation are (1) only the translations and rotations of the substrate (instead of the whole molecule) are being projected. For example, the two H atoms in the middle of the formic acid dimer molecule are not considered, (2) a frozen substrate $\mathbf{X}_0(x_1^0)$ has to be used when defining the projection operator.[63] Usually, one choose $x_1^0 = 0$ which cooresponds to the transition state. The resulting Hamiltonian which has the translations and rotations projected out approximately is :

$$H(p_1, x_1, \mathbf{P}, \mathbf{Q}) = \frac{1}{2m_1} p_1^2 + V_{eff}(x_1)$$
$$+ \sum_{k=2}^{3N-6} \frac{1}{2} P_k^2 + \frac{1}{2} \mathbf{Q} \cdot \mathbf{K}_{eff}(x_1) \cdot \mathbf{Q} - \mathbf{f}_{eff}(x_1) \cdot \mathbf{Q}. \tag{10}$$

where Q contains the 3N-12 "normal mode" coordinates of the substrate (with N-2 atoms) and the remaining 5 cartesian coordinates of the 2 H atoms,

$$\mathbf{X} - \mathbf{X}_0(x_1) = \mathbf{X}_0(x_1^0) - \mathbf{X}_0(x_1) + \mathbf{m}^{-1/2} \cdot \mathbf{U} \cdot \mathbf{Q}, \tag{11a}$$

and,

$$\mathbf{K}_{eff}(x_1) = \mathbf{U}^T \cdot \mathbf{m}^{-1/2} \cdot \mathbf{K}(x_1) \cdot \mathbf{m}^{-1/2} \cdot \mathbf{U}, \tag{11b}$$

$$\mathbf{f}_{eff} = \{\mathbf{f}(x_1) + [\mathbf{X}_0(x_1) - \mathbf{X}_0(x_1^0)] \cdot \mathbf{K}(x_1)\} \cdot \mathbf{m}^{-1/2} \cdot \mathbf{U}, \tag{11c}$$

$$V_{eff}(x_1) = V(x_1, \mathbf{X}_0(x_1)) - \mathbf{f}(x_1) \cdot [\mathbf{X}_0(x_1) - \mathbf{X}_0(x_1^0)]$$
$$+ \frac{1}{2} [\mathbf{X}_0(x_1) - \mathbf{X}_0(x_1^0)] \cdot \mathbf{K}(x_1, \mathbf{X}_0(x_1)) \cdot [\mathbf{X}_0(x_1) - \mathbf{X}_0(x_1^0)], \tag{11d}$$

with $\mathbf{U}$ being the eigenvector matrix of the projected force constant matrix defined at $(x_1^0, \mathbf{X}_0(x_1^0))$, the transition state.

There are a few different methods of treating the dynamics of a "system-bath Hamiltonian". The basis set method developed by Makri and Miller[64] is used here. The complete basis function is a product of two parts,

$$\Psi_{i,\mathbf{n}} = \chi_i(x_1)\Phi_{\mathbf{n}}^i(\mathbf{Q}). \tag{12a}$$

$\{\chi_i\}$ is a set of distributed gaussians (with the center of the i-th gaussian at grid point x_i)

$$\chi_i(x_i) = (\frac{2\alpha}{\pi})^{-1/4} \exp[-\alpha(x - x_i)^2] \tag{12b}$$

of Hamilton and Light[65] for describing the wavefunctions along the system coordinate and $\{\Phi_{\mathbf{n}}\}$ is the shifted harmonic oscillator wavefunctions with $\mathbf{n}$ being the array of the vibrational quantum numbers for the bath modes. The matrix elements of the Hamiltonian $H_{i,\mathbf{n},i',\mathbf{n}'}$ and the overlap integral $S_{i,\mathbf{n},i',\mathbf{n}'}$ are then calculated. One can further simplify the calculation by including only the diagonal terms in the bath modes, i.e., $\mathbf{n} = \mathbf{n}'$. The eigen-energies are then obtained through diagonalization of

$$\mathbf{S}^{-1/2} \cdot \mathbf{H} \cdot \mathbf{S}^{-1/2}, \tag{13}$$

and the tunneling splitting of the ground state is obtained from the difference of the two lowest energy levels.

The quantities $V_0(x_1)$, $\mathbf{f}(x_1, \mathbf{X}_0(x_1))$ and $\mathbf{K}(x_1, \mathbf{X}_0(x_1))$ have to be calculated for a few grid points (roughly 10 points) along the reaction path through *ab initio* quantum chemistry. Due to the tremendous cost of calculating the second derivatives with high level *ab initio* theory (recall that for each single geometry, 4-5 CPU hours are reqired to obtain the 2nd derivatives at the MP2/DZP level), SCF/STO-3G is used to obtain these quantities for a first test. The number of the distributed gaussians and the parameter α are varied until the energies are converged. Typically, we find 25 to 40 gaussians necessary. For the simplest calculation where only ground state wavefunctions of the bath modes are included, i.e., n=0, a value of ~0.06 cm^{-1} is obtained for $\triangle E_0$, the tunneling splitting of the ground vibrational state. Basis functions with higher vibrational wavefunctions for the bath modes could be included in the calculation, but the dimension of the Hamiltonian and the overlap integral matrices quickly become unmanageable for this 24 (i.e. 3N-6) degrees system. Usually, one will include only the wavefunctions of one or two bath modes which have strongest coupling with the system coordinate.

8.3 Global Potential Surface via Normal Mode Version of EVB

Recall in Chapter II that the simplest diabatic potential around the potential minima contains the summation of a bunch of harmonic oscillators along its normal mode coordinates (for instance, Eq.(13) of Chap II). When applied to a few 2-D model potentials which simulate isomerization reactions between two symmetric double wells, the EVB approach reproduces the original potentials very well. For a real system such as the intramolecular hydrogen transfer in formic acid dimer, such a simple approach may be reasonable since the geometries of the reactant and the product are not too different and there are only a few large amplitude normal modes

which require anharmonic correction to the potential. However, as we encountered in the previous section, for a real system, special care has to be taken in order to exclude the overall translations and rotations from the expression of the potential energy surface.

The idea of this normal mode version is to represent the two diabatic potential energy surfaces in the normal mode coordinates defined at the reactant configuration (represented as (1)) and the product configuration (as (2))

$$V_{11} = V_1 + \frac{1}{2}\mathbf{Q}^{(1)} \cdot \omega^{(1)^2} \cdot \mathbf{Q}^{(1)}, \tag{14a}$$

$$V_{22} = V_2 + \frac{1}{2}\mathbf{Q}^{(2)} \cdot \omega^{(2)^2} \cdot \mathbf{Q}^{(2)}. \tag{14b}$$

The relationship of the 3N cartesians $\{x_{i\gamma}, i = 1, \cdots, N \ , \gamma = x, y, z\}$ and the normal modes coordinates ($\mathbf{Q}^{(1)}$ for the reactant, $\mathbf{Q}^{(2)}$ for the product and $\mathbf{Q}^{(*)}$ for the transition state configuration) are

$$\begin{aligned} x_{i\gamma} &= x_{i\gamma}^{(1)} + \sum_{k=1}^{3N} L_{i\gamma,k}^{(1)} Q_k^{(1)} \\ &= x_{i\gamma}^{(2)} + \sum_{k=1}^{3N} L_{i\gamma,k}^{(2)} Q_k^{(2)} \\ &= x_{i\gamma}^{(*)} + \sum_{k=1}^{3N} L_{i\gamma,k}^{(*)} Q_k^{(*)}. \end{aligned} \tag{15}$$

where $\{x_{i\gamma}^{(1)}\}$, $\{x_{i\gamma}^{(2)}\}$, and $\{x_{i\gamma}^{(*)}\}$ are the cartesian geometries of the reactant, product and transition state configurations, and the $\{L\}$'s are the corresponding normal mode eigenvectors. One can choose either $\mathbf{Q}^{(1)}$, $\mathbf{Q}^{(2)}$ or $\mathbf{Q}^{(*)}$ as the independent coordinate system for representing the adiabatic potential V. Let's pick $\mathbf{Q}^{(*)}$ and rewrite $\mathbf{Q}^{(1)}$ and $\mathbf{Q}^{(2)}$ in terms of $\mathbf{Q}^{(*)}$. Since

$$x_{i\gamma}^{(1)} + \sum_{k=1}^{3N} L_{i\gamma,k}^{(1)} Q_k^{(1)} = x_{i\gamma}^{(*)} + \sum_{k=1}^{3N} L_{i\gamma,k}^{(*)} Q_k^{(*)},$$

multiplying each sides of the equation by $L_{i\gamma,k'}^{(1)}$, and followed by summing over i, γ, one obtains

$$Q_{k'}^{(1)} = \sum_{i,\gamma} \left[x_{i,\gamma}^{(*)} - x_{i,\gamma}^{(1)} \right] L_{i\gamma,k'}^{(1)} + \sum_{k=1}^{3N} \left[\sum_{i,\gamma} L_{i\gamma,k'}^{(1)} L_{i\gamma,k}^{(*)} \right] Q_k^{(*)}, \quad k' = 1, 3N. \qquad (16a)$$

Similarly,

$$Q_{k'}^{(2)} = \sum_{i,\gamma} \left[x_{i,\gamma}^{(*)} - x_{i,\gamma}^{(2)} \right] L_{i\gamma,k'}^{(2)} + \sum_{k=1}^{3N} \left[\sum_{i,\gamma} L_{i\gamma,k'}^{(2)} L_{i\gamma,k}^{(*)} \right] Q_k^{(*)}, \quad k' = 1, 3N. \qquad (16b)$$

Substituting Eq.(16a) into Eq.(14a), we get the following equation in matrix notation

$$\begin{aligned} V_{11}(\mathbf{Q}^{(*)}) &= V_1 + \frac{1}{2}\left[\mathbf{x}^{(*)} - \mathbf{x}^{(1)}\right]^T \cdot \mathbf{K}^{(1)} \cdot \left[\mathbf{x}^{(*)} - \mathbf{x}^{(1)}\right] \\ &\quad + \left[\mathbf{x}^{(*)} - \mathbf{x}^{(1)}\right]^T \cdot \mathbf{K}^{(1)} \cdot \mathbf{L}^{(*)} \cdot \mathbf{Q}^{(*)} + \frac{1}{2}\mathbf{Q}^{(*)T} \cdot \mathbf{L}^{(*)T} \cdot \mathbf{K}^{(1)} \cdot \mathbf{L}^{(*)} \cdot \mathbf{Q}^{(*)} \\ &= V_1' + \mathbf{D}_1' \cdot \mathbf{Q}^{(*)} + \frac{1}{2}\mathbf{Q}^{(*)T} \cdot \mathbf{K}_1' \cdot \mathbf{Q}^{(*)} \end{aligned} \qquad (17)$$

where $\mathbf{K}^{(1)} = \mathbf{L}^{(1)} \cdot \omega^{(1)2} \cdot \mathbf{L}^{(1)T}$, $V_1' = V_1 + \frac{1}{2}\left[\mathbf{x}^{(*)} - \mathbf{x}^{(1)}\right]^T \cdot \mathbf{K}^{(1)} \cdot \left[\mathbf{x}^{(*)} - \mathbf{x}^{(1)}\right]$, $\mathbf{D}_1' = \left[\mathbf{x}^{(*)} - \mathbf{x}^{(1)}\right]^T \cdot \mathbf{K}^{(1)} \cdot \mathbf{L}^{(*)}$, and $\mathbf{K}_1' = \mathbf{L}^{(*)T} \cdot \mathbf{K}^{(1)} \cdot \mathbf{L}^{(*)}$. A similar equation is obtained for $V_{22}(\mathbf{Q}^{(*)})$.

8.3.1 Orientation

Same as in the case of the "Cartesian Reaction Path Hamiltonian" method, the potential functions contain the three translational and three rotational parts that need to be projected out. This is a common situation when one starts with the 3N cartesian coordinates.

Let us rewrite Eq.(15) as follows, where the 3N-6 local 'internal' normal coordinates are seperated from the remaining 6 local overall translations and rotations.

$$\begin{aligned} x_{i\gamma} &= x_{i\gamma}^{(1)} + \sum_{k=1}^{3N-6} L_{i\gamma,k}^{(1)} Q_k^{(1)} + \sum_{k=3N-5}^{3N} L_{i\gamma,k}^{(1)} Q_k^{(1)} \\ &= x_{i\gamma}^{(2)} + \sum_{k=1}^{3N-6} L_{i\gamma,k}^{(2)} Q_k^{(2)} + \sum_{k=3N-5}^{3N} L_{i\gamma,k}^{(2)} Q_k^{(2)} \\ &= x_{i\gamma}^{(*)} + \sum_{k=1}^{3N-6} L_{i\gamma,k}^{(*)} Q_k^{(*)} + \sum_{k=3N-5}^{3N} L_{i\gamma,k}^{(*)} Q_k^{(*)} \end{aligned} \tag{18}$$

The characteristics of the eigenvectors of these local translations and rotations vary from one geometry to another. However, one would like $\{L_k^{(1)}\}$, $\{L_k^{(2)}\}$ and $\{L_k^{(*)}\}$ (for k=3N-5,$\cdots$, 3N) to span the same space so that

$$\sum_{k=3N-5}^{3N} L_{i\gamma,k}^{(1)} Q_k^{(1)} = \sum_{k=3N-5}^{3N} L_{i\gamma,k}^{(2)} Q_k^{(2)} = \sum_{k=3N-5}^{3N} L_{i\gamma,k}^{(*)} Q_k^{(*)}, \tag{19a}$$

and,

$$x_{i\gamma}^{(1)} + \sum_{k=1}^{3N-6} L_{i\gamma,k}^{(1)} Q_k^{(1)} = x_{i\gamma}^{(2)} + \sum_{k=1}^{3N-6} L_{i\gamma,k}^{(2)} Q_k^{(2)} = x_{i\gamma}^{(*)} + \sum_{k=1}^{3N-6} L_{i\gamma,k}^{(*)} Q_k^{(*)}. \tag{19b}$$

Under this circumstance, simply by changing the upper limit of the subscripts k and k' from 3N to 3N-6, Eqs.(16-17) can be utilized to describe diabatic potentials which include only the 3N-6 "internal" coordinates. In order to satisfy Eq.(19), we pursue the conditions such that only one set of $\{L_k\}$, (k=3N-5 to 3N) is independent. I.e.,

$$L^{(1)}_{i\gamma,k} \stackrel{?}{=} \sum_{k'=3N-5}^{3N} L^{(*)}_{i\gamma,k} A_{k',k}, \tag{20a}$$

$$L^{(2)}_{i\gamma,k} \stackrel{?}{=} \sum_{k'=3N-5}^{3N} L^{(*)}_{i\gamma,k} A'_{k',k}. \tag{20b}$$

where $\mathbf{A}$ and $\mathbf{A}'$ represent the tranformation matrices with dimensions of 6 by 6 if the above equations are valid.

Ideally, Eq.(19-20) could be satisfied by properly orient the geometries of the reactant, product and transition state in the three dimensional space. But, this involves the complexity of finding the 3 Euler angles[66] of each geometries. A simpler alternative is to 'guess' and vary the relative orientations of the three geometries in space until minimum values of the following determinants $\triangle^{(1)}$ and $\triangle^{(2)}$ are obtained,

$$| \mathbf{L}^{(1)} - \mathbf{L}^{(*)} \cdot \mathbf{A} | \equiv \triangle^{(1)}, \tag{21a}$$

$$| \mathbf{L}^{(2)} - \mathbf{L}^{(*)} \cdot \mathbf{A}' | \equiv \triangle^{(2)}. \tag{21b}$$

If $\triangle^{(1)}$ (and $\triangle^{(2)}$) is found to be zero for some specific relative orientations, the conditions stated in Eqs.(19-20) are found. One can rewrite $\triangle^{(1)}$ (and $\triangle^{(2)}$) as

$$\begin{aligned}
\triangle^{(1)} &= tr\left[(\mathbf{L}^{(1)^T} - \mathbf{A}^T \cdot \mathbf{L}^{(*)^T}) \cdot (\mathbf{L}^{(1)} - \mathbf{L}^{(*)} \cdot \mathbf{A})\right] \\
&= tr\left[\mathbf{L}^{(1)^T} \cdot \mathbf{L}^{(1)} + \mathbf{A}^T \cdot \mathbf{L}^{(*)^T} \cdot \mathbf{L}^{(*)} \cdot \mathbf{A} - \mathbf{A}^T \cdot \mathbf{L}^{(*)^T} \cdot \mathbf{L}^{(1)} - \mathbf{L}^{(1)^T} \cdot \mathbf{L}^{(*)} \cdot \mathbf{A}\right] \\
&= 6 + \sum_{k,k'} A^2_{k,k'} - 2\sum_{k,k'} (L^{(1)^T} \cdot L^{(*)})_{k,k'} A_{k',k}.
\end{aligned} \tag{21c}$$

The identity

$$\mathbf{L}^{(1)^T} \cdot \mathbf{L}^{(1)} = \mathbf{I},$$

and

$$\mathbf{L}^{(*)^T} \cdot \mathbf{L}^{(*)} = \mathbf{I},$$

have been used in deriving the above equations. From variational principle,

$$\frac{\partial \triangle^{(1)}}{\partial A_{k,k'}} = 2A_{k,k'} - 2(L^{(1)^T} \cdot L^{(*)})_{k,k'} = 0.$$

one obtains,

$$A_{k,k'} = (L^{(1)^T} \cdot L^{(*)})_{k,k'},$$

and

$$\triangle^{(1)} = 6 - \sum_{k,k'} (L^{(1)^T} \cdot L^{(*)})^2_{k,k'}.$$

Since, for the translational degrees of freedom,

$$\sum_{k,k'=3N-5}^{3N-3} (L_k^{(1)^T} \cdot L_{k'}{}^{(*)})^2 = 3,$$

one can further simplify the expression of $\triangle^{(1)}$ as

$$\triangle^{(1)} = 3 - \sum_{k,k'=3N-2}^{3N} (L_k^{(1)^T} \cdot L_{k'}{}^{(*)})^2. \qquad (22)$$

With an initial guess of the relative orientations of the three geometries, one can minimize $\Delta^{(1)}$ by using a 3-dimensional rotational matrix M to vary the relative orientation. In other words, we seek a M that will minimize

$$\Delta^{(1)} = 3 - \sum_{k,k'} \left(\sum_{i\gamma} \sum_{\gamma'} M_{\gamma\gamma'} L^{(1)}_{i\gamma',k} L^{(*)}_{i\gamma,k'} \right)^2 . \tag{23}$$

We found that, if the reactant and product are orientated according to what we suggested in ref.67, one will get a minimum Δ if the reaction is restricted to be on a plane. To be more explicit, one calculate the angle ϕ that is required to rotate the original reactant geometry to a new orientation according to

$$\phi = \tan^{-1} \left[\frac{\sum_i m_i (x_i^{(1)} x_i^{(*)} + y_i^{(1)} y_i^{(*)})}{\sum_i m_i (x_i^{(1)} y_i^{(*)} - x_i^{(*)} y_i^{(1)})} \right], \tag{24}$$

if the motion of the molecule is restricted to be on the xy-plane. The superscripts (1) and (*) indicate the reactant and the transition state geometries. For example, using the MP2/DZP optimized geometries, if the original molecular orientations of the reactant, the product, and the transition state are such that the C$\cdots$C lie on the x-axis, using Eq.(24) we found that the reactant geometry should be rotate by about 0.033°, and the product geometry by -0.033°.

8.3.2 Global Minima of the Potential

The "approximate" 3N-6 dimensional global potental energy surface is easily obtained through this normal mode version of EVB approach. Again, the validity of this global potential surface needs to be examined. Here, the locations of the global minima are tested. The correct minimum locations of the "true" PES (i.e., Born-Oppenheimer PES obtained completely through *ab initio* calculations) are at

, for the reactant, $\mathbf{Q}^{(1)} = 0$ and , for the product, $\mathbf{Q}^{(2)} = 0$. These two locations can be rewritten in the transition state normal mode coordinate system using Eq.(16) with the knowledge of the eigenvectors $\mathbf{L}^{(1)}$, $\mathbf{L}^{(2)}$ and $\mathbf{L}^{(*)}$. Since the most important normal modes are those with same symmetry as the reaction coordinate (A_g in C_{2h} and B_{1g} in D_{2h}), we show in Figures 5 the 9 A_g symmetry normal modes obtained from MP2/DZP for the reactant geometries. Those of the product configuration can be obtained through rotation of normal modes in Fig. 5 by 180° about either x or y axis. The 5 A_g and 4 B_{1g} normal modes of the transition state configuration are shown in Figure 6. The minimum locations of these 9 normal modes are shown in Table XIX. The coordinates for the other modes with A_u, B_g and B_u (in C_{2h} point group) are essentially zero (due to zero coupling with the reaction coordinate) for these geometries at stationary points on the PES. On the other hand, the global minima of the "approximate" EVB potential surface are searched with the Newton-Raphson method[68] and compared with the correct values. As seen in Table XIX, very good agreement is obtained.

9 Concluding Remarks

The results presented and discussed here are just a fraction of the information available from the present study. For example, in the study of the vibrational frequencies and IR intensities with SCF, we have not reported theoretical predictions for any of the "mixed dimers", namely HCOOH·HCOOD, HCOOH·DCOOH, HCOOH·DCOOD, HCOOD·DCOOH, HCOOD·DCOOD, and DCOOH·DCOOD. Among the transition states for hydrogen or deuterium transfer, only $(HCOOH)_2$ among the ten distinct possibilities has been considered. Moreover, only for HCOOH and $(HCOOH)_2$ have Raman intensity data been presented. It is apparent that the formic acid dimer is a source of much theoretical and experimental information. As

such it provides a unique opportunity for the understanding of hydrogen-bonding and hydrogen atom transfer processes.

For the double hydrogen atom transfer reaction, since the dynamics depends sensitively on the information of the potential energy surface, we perform *ab initio* studies of the energetic and the harmonic vibrational frequencies of the transition state and the equilibrium dimers beyond SCF level of theory. The potential bare barrier height has been improved from 15.6 Kcal to about 7 - 8 kcal/mol with the Moller-Plesset method.

Tunneling splitting of the ground vibrational state pertaining to this double hydrogen atom transfer reaction is estimated with very simple WKB method. The results vary from 0.3 to 70 cm^{-1} depending on the set of *ab initio* data used. Obviously, this method can only give a vague guideline of the tunneling splitting even if definite values of the barrier height and harmonic frequencies are available. The method of cartesian reaction path Hamiltonian (with off diagonal bath mode coupling excluded) has also been applied here and a value of 0.06 cm^{-1} is obtained by using the STO-3G information. Higher order coorections to this method such as (1) including wavefunctions of higher vibrational states of the bath modes and (2) including off-diagonal bath mode coupling, may be added in order to obtain converged answer but the size of the matrices involved would quickly become tremendous.

One simple way to study the reaction dynamics is to perform trajectory calculations. Makri and Miller[69] suggested a semi-classical tunneling model which allows trajectories to leak from one potential well to the other in imaginary time. Results of the tunneling splitting using this method for a few simple potentials are encouraging. We have constructed a global (24 dimensions) potential energy surface via the normal mode version of the EVB approach for the formic acid dimer which is ready to be used for this type of study.

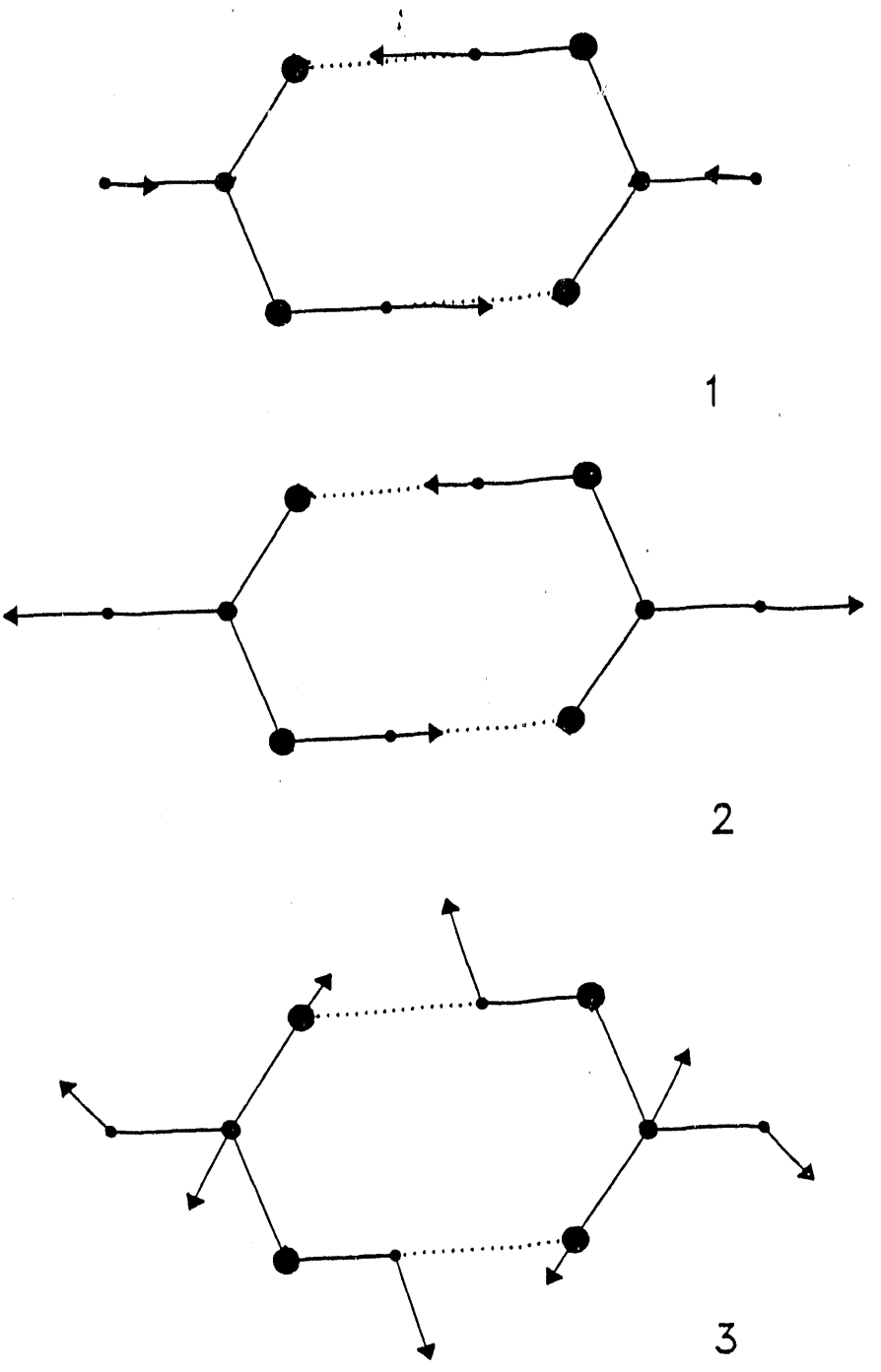

Figure 5: Normal modes of formic acid dimer with A_g symmetry at the MP2/DZP reactant configuration. The lable of each mode is same as that in Table XVIII. The three different atomes are represented by different sizes, with O>C>H.

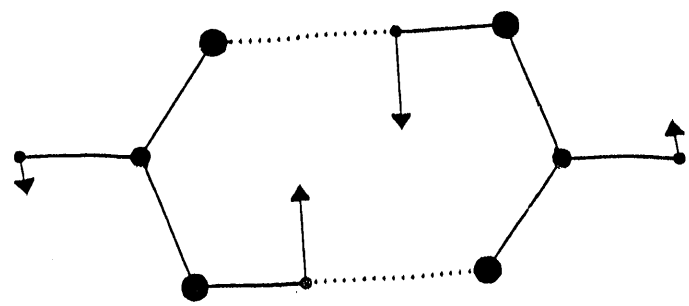

4

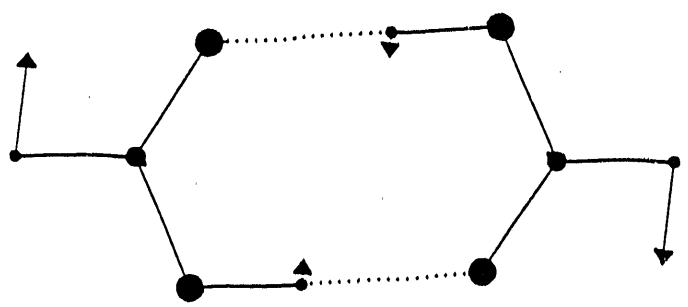

5

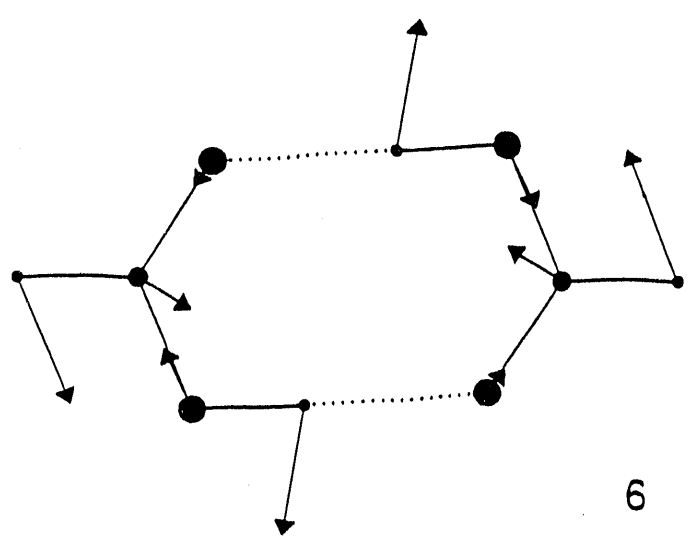

6

Figure 5, continued.

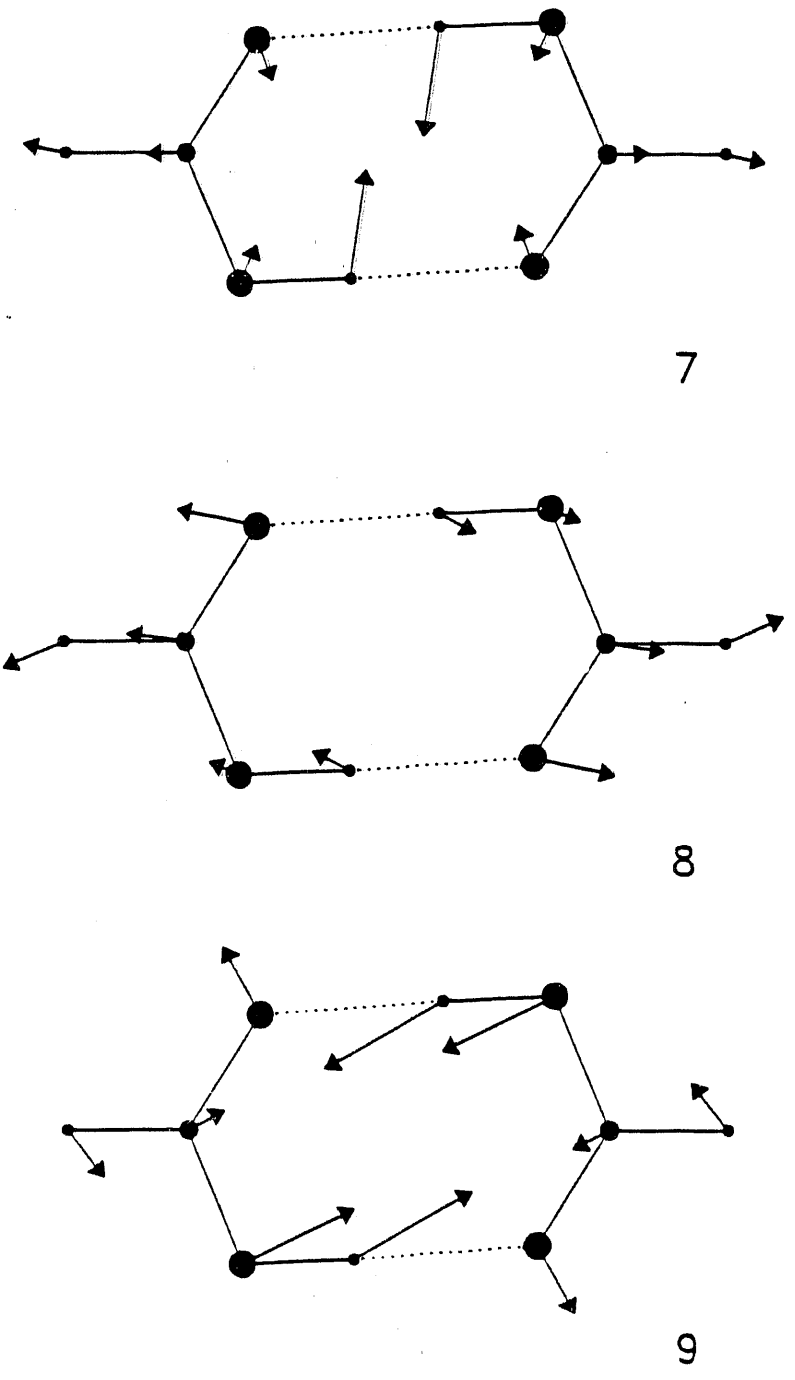

Figure 5, continued.

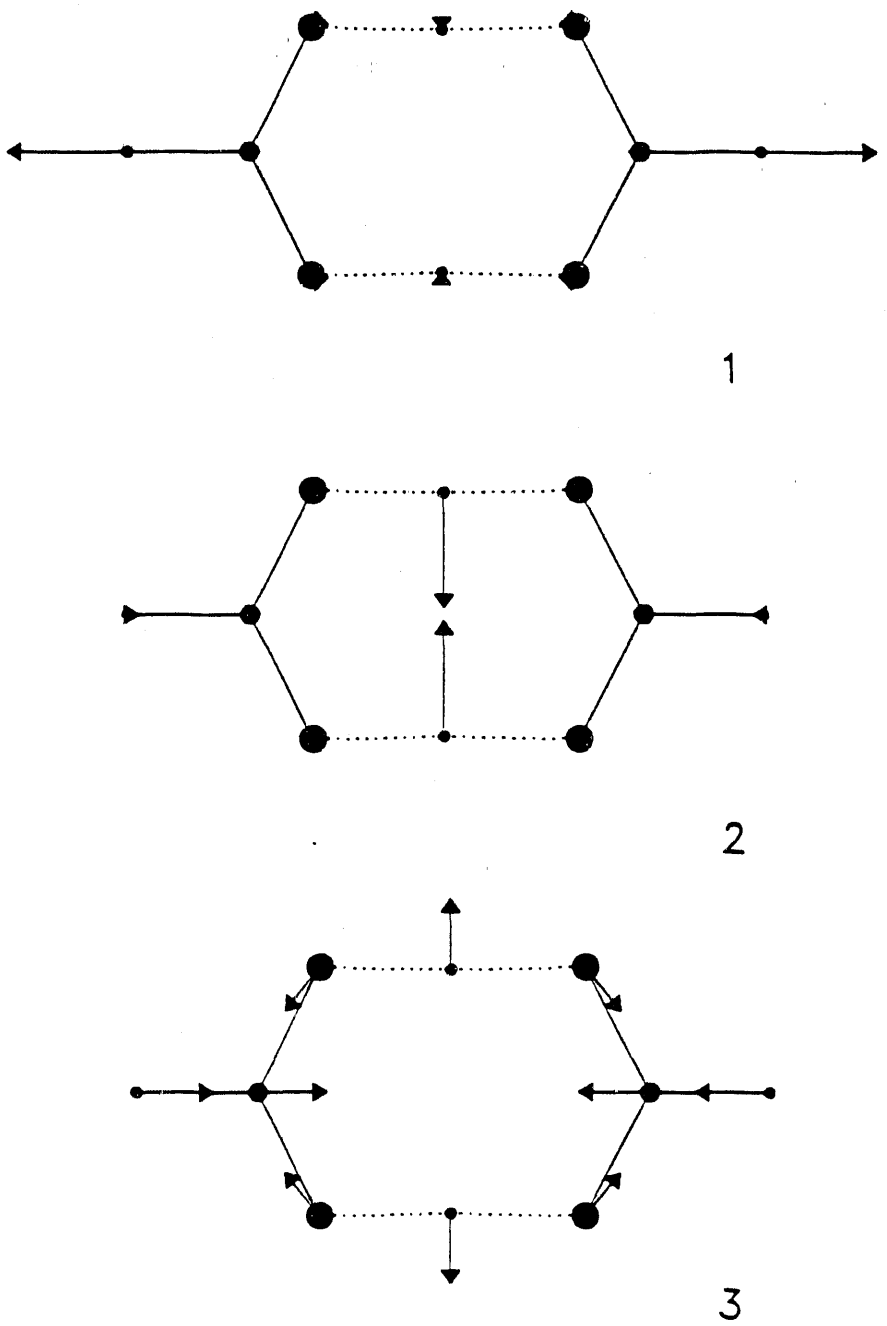

Figure 6: Normal modes of the transition state configuration with either A_g or B_{1g} symmetry.

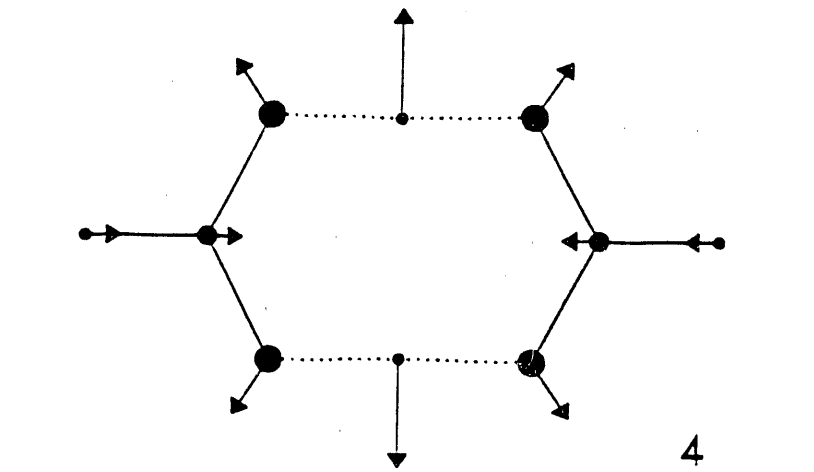

4

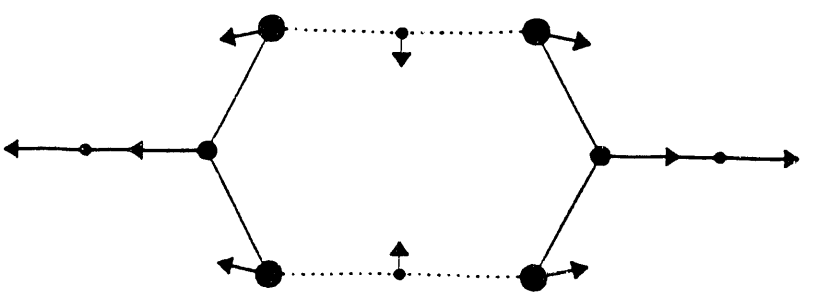

5

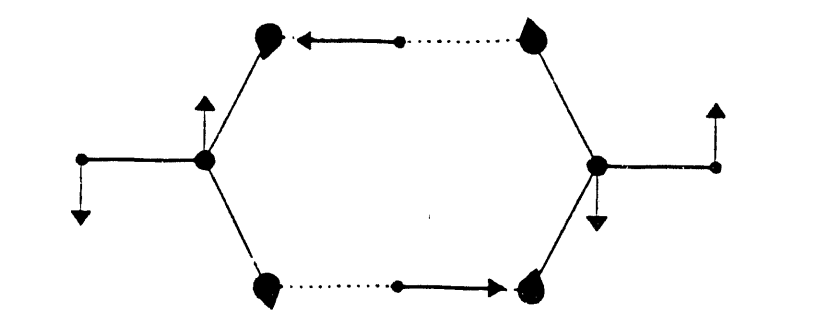

6

Figure 6, continued.

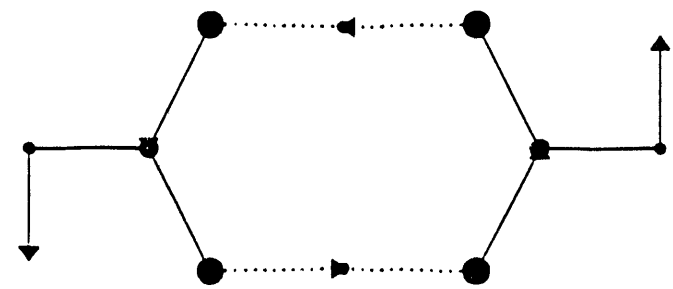

7

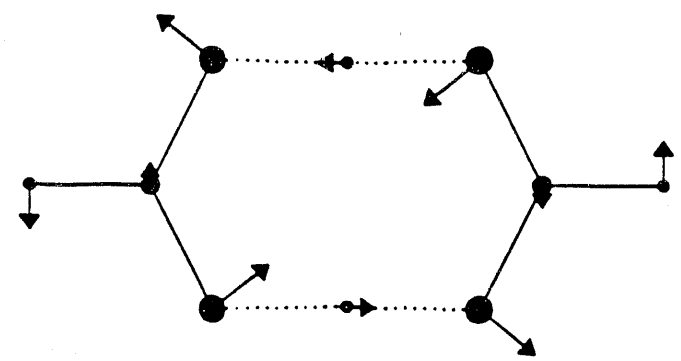

8

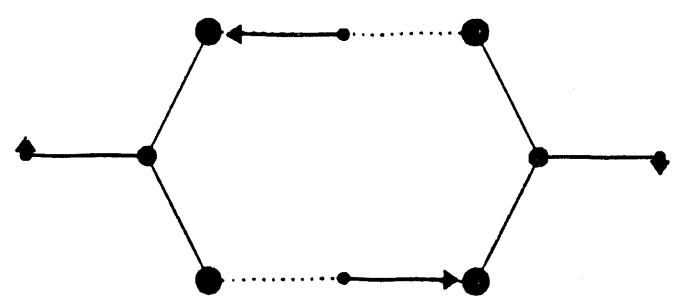

9

Figure 6, continued.

References

[1] G. C. Pimentel and A. L. McClellan, *The Hydrogen Bond*; Freeman: San Francisco (1960).

[2] S. N. Vinogradov and R. H. Linnell, *Hydrogen Bonding*; Van Nostrand-Reinhold: New York (1971).

[3] M. L. Joesten and L. J. Schaad, *Hydrogen Bonding*; Marcel Dekker: New York (1974).

[4] P. Schuster, G. Zundel, and C. Sandorfy, Eds. *The Hydrogen Bond. Recent Developments in Theory and Experiments*; North Holland: Amsterdam (1976).

[5] H. Ratajczak and W. J. Orville-Thomas, *Molecular Interactions*; Wiley: Chichester; Vol. 1 (1980); Vol. 2 (1981).

[6] L. Pauling and L. O. Brockway, *Proc. Natl. Acad. Sci. U. S. A.* **20**, 336 (1934).

[7] J. Karle and L. O. Brockway, *J. Am. Chem. Soc.* **66**, 574 (1944).

[8] O. Bastiansen, Chr. Finbak, and O. Hassel, *Tidsskr. Kjemi Bergves. Metall.* **9**, 81 (1944).

[9] A. Almenningen, O. Bastiansen, and T. Motzfeldt, *Acta Chem. Scand.* **23**, 2848 (1969); **24**, 747 (1970).

[10] R. C. Millikan and K. S. Pitzer, *J. Am. Chem. Soc.* **80**, 3515 (1958).

[11] G. L. Carlson, R. E. Witkowski, and W. G. Fateley, *Spectrochim. Acta* **22**, 1117 (1966).

[12] D. Clague and A. Novak, *J. Mol. Struct.* **5**, 149 (1970).

[13] P. Excoffon and Y. Marechal, *Spectrochim. Acta, Part A* **28**, 269 (1972).

[14] J. Bournay and Y. Marechal, *Spectrochim. Acta, Part A* **31**, 1351 (1975).

[15] J. E. Bertie and K. H. Michaelian, *J. Chem. Phys.* **76**, 886 (1982).

[16] J. E. Bertie, K. H. Michaelian, H. H. Eysel, and D. Hager, *J. Chem. Phys.* **85**, 4779 (1986).

[17] A. D. H. Clague and H. J. Bernstein, *Spectrochim. Acta* **25**, 593 (1969).

[18] J. L. Derrissen and P. H. Smith, *Acta Crystallogr., Sect. A* **34**, 842 (1978).

[19] S. Tomoda, Y. Achiba, K. Nomoto, K. Sato, and K. Kimura. *Chem. Phys.* **74**, 113 (1983).

[20] K. I. Lazaar and S. H. Bauer, *J. Am. Chem. Soc.* **107**, 3769 (1985).

[21] E. Clementi, J. Mehl, and W. von Niessen, *J. Chem. Phys.* **54**, 508 (1971).

[22] E. Ady and J. Brickmann, *Chem. Phys. Lett.* **11**, 302 (1971).

[23] J. E. Del Bene and W. L. Kochenour, *J. Am. Chem. Soc.* **98**, 2041 (1976).

[24] S. Iwata and K. Morokuma, *Theor. Chim. Acta* **44**, 323 (1977).

[25] P. Bosi, G. Zerbi, and E. Clementi, *J. Chem. Phys.* **66**, 3376 (1977).

[26] S. Yamabe, K. Kitaura, and K. Nishimoto, *Theor. Chim. Acta* **47**, 111 (1978).

[27] S. Scheiner and C. W. Kern, *J. Am. Chem. Soc.* **101**, 4081 (1979).

[28] P. H. Smith, J. L. Derissen, and F. B. van Duijneveldt, *Mol. Phys.* **37**, 501 (1979).

[29] J. Lipinski and W. A. Sokalski, *Chem. Phys. Lett.* **76**, 88 (1980).

[30] A. Agresti, M. Bacci, and A. Ranfagni, *Chem. Phys. Lett.* **79**, 100 (1981).

[31] F. Graf, R. Meyer, T.-K. Ha, and R. R. Ernst, *J. Chem. Phys.* **75**, 2914 (1981).

[32] G. N. Robertson and M. C. Lawrence, *Chem. Phys.* **62**, 131 (1981).

[33] S. Hayashi, J. Umemura, S. Kato, and K. Morokuma, *J. Phys. Chem.* **88**, 1330 (1984).

[34] A. Karpfen, *Chem. Phys.* **88**, 415 (1984).

[35] A. S. N. Murthy and S. Ranganathan, *Int. J. Quantum. Chem.* **27**, 547 (1985).

[36] C. Mijoule, M. Allavena, J. M. Leclercq, and Y. Bouteiller, *Chem. Phys.* **109**, 207 (1986).

[37] M. J. Wojcik, A. Y. Hirakawa, and M. Tsuboi, *Int. J. Quantum. Chem: Quantum Biol. Symp.* **13**, 133 (1986).

[38] (a) I. C. Hisatsune and J. Heicklen, *Can. J. Spectrosc.* **18**, 135 (1973).
(b) See also: R. L. Redington, *J. Mol. Spectrosc.* **65**, 171 (1977).

[39] (a) R. C. Millikan and K. S. Pitzer, *J. Chem. Phys.* **27**, 1305 (1957).
(b) T. Miyazawa and K. S. Pitzer, *J. Chem. Phys.* **30**, 1076 (1959).

[40] G. Kwei and R. Curl, *J. Chem. Phys.* **32**, 1592 (1960).

[41] A. M. Mirri, *Nuovo Cimento* **18**, 849 (1960).

[42] (a) S. J. Huzinaga, *J. Chem. Phys.* **42**, 1293 (1965).
(b) T. H. Dunning, *J. Chem. Phys.* **53**, 2823 (1970).

[43] (a) P. Saxe, Y. Yamaguchi, and H. F. Schaefer, *J. Chem. Phys.* **77**, 5647 (1982).
(b) Y. Osamura, Y. Yamaguchi, P. Saxe, D. J. Fox, M. A. Vincent, and H. F. Schaefer, *J. Mol. Struct.* **103**, 183 (1983).

[44] J. E. Boggs and F. R. Cordell, *J. Mol. Struct.* **76**, 329 (1981).

[45] Y. Yamaguchi and H. F. Schaefer, *J. Chem. Phys.* **73**, 2310 (1980).

[46] J. Dybal, T. C. Cheam, and S. Krimm, to be published.

[47] M. Gussoni, *Vibrational Intensities in Infrared and Raman Spectroscopy*; W. B. Person, G. Zerbi, Eds.; Elsevier: Amsterdam (1982); pp 221-238.

[48] M. J. Frisch, Y. Yamaguchi, J. F. Gaw, H. F. Schaefer, and J. S. Binkley, *J. Chem. Phys.* **84**, 531 (1986).

[49] D. J. Swanton, G. B. Bacskay, and N. S. Hush, *Chem Phys.* **83**, 69 (1984).

[50] R. D. Amos, *Chem. Phys. Lett.* **124**, 376 (1986).

[51] D. M. Mathews and R. W. Sheets, *J. Chem. Soc. A* 2203, (1969).

[52] G. Henderson, *J. Chem. Educ.* **64**, 88 (1987).

[53] P. A. Kollman, *Modern Theoretical Chemistry*; H. F. Schaefer, Ed.; Plenum: New York (1977); Vol. 4, pp 109–152.

[54] (a) A. Szabo and N. S. Ostlund, *Modern Quantum Chemistry*; Macmillan Publishing: New York (1982).
(b) R. D. Amos, *Chem. Phys. Lett.* **73**, 602 (1980).
(c) E. D. Simandiras, N. C. Handy, and R. D. Amos, *Chem. Phys. Lett.* **133**, 324 (1987).
(d) R. Krishnan, M. J. Frisch, and J. A. Pople, *J. Chem. Phys.* **72**, 4244 (1980).
(e) R. Krishnan and J. A. Pople, *Int. J. Quantum. Chem.* **14**, 91 (1978).

[55] CADPAC stands for "*The Cambridge Analytic Derivatives Package*". A user guide (issure 4.0) was written by R. D. Amos and J. E. Rice.

[56] Michael Frish, *Gaussian88 User's Guide and Programmer's Reference*, (1988).

[57] T. H. Dunning, Jr. *J. Chem. Phys.* **55**, 716 (1971).

[58] J. Bicerano, H. F. Schaefer, and W. H. Miller, *J. Chem. Phys.* **78**, 259 (1983).

[59] W. H. Miller, N. C. Handy, and J. E. Adams, *J. Chem. Phys.* **72**, 99 (1980).

[60] (a) T. Carrington, Jr. and W. H. Miller, *J. Chem. Phys.* **81**, 3942 (1984).
(b) T. Carrington, Jr. and W. H. Miller, *J. Chem. Phys.* **84**, 4364 (1986).

[61] B. A. Ruf and W. H. Miller, *J. Chem. Soc., Faraday Trans. 2*, **84**, 1523 (1988).

[62] See, for example, H. S. Johnston, *Gas Phase Reaction Rate Theory*, Ronald Press: New York (1966).

[63] See ref.59 for the definition of the projection operator.

[64] N. Makri and W. H. Miller, *J. Chem. Phys.* **86**, 1451 (1987).

[65] I. P. Hamilton and J. C. Light *J. Chem. Phys.* **84**, 306 (1986).

[66] H. Goldstein, *Classical Mechanics*; Addison-Wesley (1981); p.143.

[67] W. H. Miller, B. A. Ruf, and Y. T. Chang, *J. Chem. Phys.* **92**, 6298 (1989).

[68] Newton-Raphson method, see: W. H. Press, B. P. Flannery, S. A. Teukolsky, and W. T. Vetterling, *Numerical Recipes, The Art of Scientific Computing.*

[69] N. Makri and W. H. Miller, *J. Chem. Phys.* **91**, 4026 (1989).

Table I. Theoretical (Self-Consistent-Field) and Experimental Equilibrium Geometries for the Formic Acid Monomer[b]

	STO-3G	DZ	DZ+P	exptl[c]
$r(C_1{=}O_2)$[a]	1.214	1.210	1.185	1.202
$r(C_1{-}O_3)$	1.386	1.351	1.324	1.343
$r(C_1{-}H_4)$	1.104	1.075	1.088	1.097
$r(O_3{-}H_5)$	0.990	0.956	0.952	0.972
$\angle O_2{=}C_1{-}O_3$[d]	123.6	124.5	125.0	124.6
$\angle H_4{=}C_1{-}O_2$	126.0	125.2	124.5	124.1
$\angle H_4{=}C_1{-}O_3$	110.4	110.4	110.5	
$\angle C_1{=}O_3{-}H_5$	104.8	115.3	109.0	106.3

[a] Bond distances in Å.

[b] For atom numbering see Figure 1.

[c] Experimental structure is that chosen by: Harmony, M. D.; Laurie, V. W.; Kuczkowski, R. L.; Schwendeman, R. H.; Ramsay, D. A.; Lovas, F. J.; Lafferty, W. J.; Maki, A. G. *J. Phys. Chem. Ref. Data* **1979**, 8,619.

[d] Angles in degree.

Table II. Theoretical (Self-Consistent-Field) and Experimental Equilibrium Geometries for the Formic Acid Dimer[c]

	STO-3G	DZ	DZ+P	exptl[c]
$r(C_1{=}O_5)$	1.231	1.225	1.199	1.217±0.003
$r(C_1{-}O_3)$	1.348	1.321	1.300	1.320±0.003
$r(C_1{-}H_7)$	1.107	1.075	1.087	1.079±0.021
$r(O_3{-}H_9)$	1.009	0.975	0.966	1.033±0.017
$r(O_3\cdots O_4)$	2.536	2.700	2.779	2.696±0.007
$r(O_3\cdots O_5)$	2.296	2.260	2.227	2.262±0.004
$r(C_1\cdots C_2)$	3.690	3.847	3.890	
$r(O_4\cdots H_9)$	1.526	1.752	1.818	
$\angle O_3{-}C_1{=}O_5$	125.7	125.1	125.9	126.2±0.5
$\angle H_7{-}C_1{=}O_5$	122.2	122.5	122.2	115.4±3.1
$\angle H_7{-}C_1{-}O_3$	112.0	112.4	111.9	
$\angle C_1{-}O_3{-}H_9$	108.1	116.6	110.0	108.5±0.4
$\angle O_3{-}H_9\cdots O_4$	179.0	163.5	172.7	(180)[b]

[a] From ref 9 and the compliation by Harmony, et al., footnote c to Table I.
[b] Geometrical parameter assumed in the refinement of the electron diffraction data.
[c] Bond distances in Å, angles in degree.

Table III. Vibrational Frequencies and IR Intensities for the HCOOH Monomer[f]

		DZ		DZ+P			
		freq[a]	int[b]	freq[a]	int[b]	exptl	assignment
A'	ν_1	4030	104	4116	116	3569[c]	O–H
	ν_2	3400	34	3293	53	2942[c]	C–H
	ν_3	1872	481	2015	533	1777[c]	C=O
	ν_4	1519	7	1536	10	1381[c]	H–C–O
	ν_5	1382	22	1426	26	1223[e]	H–O–C
	ν_6	1185	335	1268	301	1104[c]	C–O
	ν_7	648	71	690	62	625[c]	O–C=O
A"	ν_8	1160	1	1183	0.3	1033[d,e]	H–C–O oop
	ν_9	680	310	693	201	642[c]	H–O–C oop

[a] In cm^{-1}.
[b] km/mol.
[c] From ref 15.
[d] From ref 43.
[e] From ref 42.
[f] Note that the theoretical prediction are harmonic frequencies, while the experimental values are the observed(anharmonic) fundamentals.

Table IV. Vibrational Frequencies and IR Intensities for the Formic Acid Dimer Equilibrium Geometry

		DZ		DZ+P		exptl[a]		
		freq	int	freq	int	freq	int	assignment
A_g	ν_1	3620	0	3782	0			O–H
	ν_2	3401	0	3303	0	2949		C–H
	ν_3	1800	0	1927	0	1670		C=O
	ν_4	1549	0	1561	0	1415		H–O–C
	ν_5	1503	0	1527	0	1375		H–C–O
	ν_6	1295	0	1357	0	1214		C–O
	ν_7	696	0	732	0	677		O–C=O
	ν_8	209	0	182	0	190		O···O
	ν_9	181	0	164	0	137		O–H···O ip
B_g	ν_{10}	1184	0	1200	0	1060		δC–H oop
	ν_{11}	1029	0	935	0			δO–H oop
	ν_{12}	262	0	250	0	230		O–H···O oop
A_u	ν_{13}	1190	43	1203	0.4	1050		δC–H oop
	ν_{14}	1075	566	985	357	917	strong	δO–H oop
	ν_{15}	188	24	174	13	163	medium	O–H···O oop
	ν_{16}	101	3	81	4	68	weak	twist about C–H bond
B_u	ν_{17}	3686	1551	3835	1575	3110	very strong	O–H
	ν_{18}	3398	130	3300	156	2957	very strong	C–H
	ν_{19}	1840	1145	1983	1188	1754	very strong	C=O
	ν_{20}	1536	5	1551	19	1450	very weak	HOC[b]
	ν_{21}	1495	140	1505	75	1365	medium	HCO[b]
	ν_{22}	1289	549	1358	478	1218	very strong	C–O
	ν_{23}	717	95	747	85	697	medium	O–C=O
	ν_{24}	249	54	223	48	248	strong	O–H···O ip

[a] Experimental fundamentala for the dimer are reviewed in ref 15; intensity labels are from Millikan and Pitzer, ref 10, and Clague and Novak, ref 12.

[b] These assignments are from DZ SCF theory and Bertie and Michaelien, ref 15. DZ+P SCF theory reverses the identifications of ν_{20} and ν_{21}.

Table V. Dimer-Monomer Vibrational Frequency Shifts (in cm^{-1}) for Formic Acid[b]

		$\Delta\omega$(DZ SCF)	$\Delta\omega$(DZ+P SCF)	$\Delta\nu$(exptl)	assignment
A_g	1	-410	-344		O-H
	2	+1	+10	+7	C-H
	3	-72	-88	-107	C=O
	4	+167	+135	+193	H-O-C
	5	-16	-9	-6	H-C-O
	6	+110	+89	+110	C-O
	7	+48	+42	+52	O-C=O
B_g	10	+24	+17	+27	δC-H oop
	11	+349	+242		δO-H oop
A_u	13	+30	+20	+17	δC-H oop
	14	+395	+292	+276	δO-H oop
B_u	17	-344	-281	-459	O-H
	18	-2	+7	+15	C-H
	19	-32	-32	-23	C=O
	20	+154	+15	+227	H-C-O[a]
	21	-24	+79	-16	H-O-C[a]
	22	+104	+90	+114	C-O
	23	+69	+57	+72	O-C=O

[a] These assignments are from DZ+P SCF theory. DZ SCF and Bertie and Michaelian reverse the identifications of ν_{20} and ν_{21}.

[b] Experimental Vibrational frequencies are from ref 10, 15, 42, and 43. Dimer frequencies with no immediate counterpart in the monomer are excluded here.

Table VI. Vibrational Frequencies (cm^{-1}) and IR Intensities (km/mol) for HCOOD[b]

		ω(theory)	int(theory)	ν(exptl)[a]	assignment
A'	1	3294	47	2938/2942	C-H
	2	2995	76	2631	O-D
	3	2010	511	1773	C=O
	4	1530	12	1368	H-C-O
	5	1327	235	1178	C-O
	6	1105	59	972	D-O-C
	7	616	59	560	O-C=O
A"	8	1182	1	1011	H-C-O oop
	9	544	124	508	D-O-C oop

[a] Bertie et al., ref 16; Hisatsune and Heicklen, ref 42.
[b] All theoretical predications were made at the DZ+P SCF level of theory.

Table VII. Vibrational Frequencies (cm^{-1}) and IR Intensities (km/mol) for $(HCOOD)_2^c$

			freq	int[a]		(dimer−monomer)[d]		assignment
A_g	1	3303	(2951)	0		+9	(+9/+13)	C–H
	2	2760	(–)	0		-235	(–)	O–D
	3	1913	(1663/1679)	0		-97	(-110/-94)	C=O
	4	1539	(1383)	0		+9	(+15)	H–C–O
	5	1400	(1261)	0		+73	(+83)	C–O
	6	1175	(972)	0		+70	(0)	D–C–O
	7	670	(624)	0		+54	(+64)	O–C=O
	8	182	(–)	0			NC	O···O
	9	160	(~144)	0			NC	O–D···O ip
B_g	10	1197	(1060?)	0		+15	(+49?)	δC–H oop
	11	692	(–)	0		+148	(–)	δO–D oop
	12	244	(224)	0			NC	O–D···O oop
A_u	13	1198	(1037)	3		+16	(+26)	δC–H oop
	14	741	(693)	221		+197	(+185)	δO–D oop
	15	166	(158)	11	(s)[b]		NC	O–D···O oop
	16	81	(68)	4	(m)[b]		NC	twist about C–H bond
B_u	17	3302	(2960)	102	(m)	+8	(+18/+22)	C–H
	18	2793	(2068)	891		-202	(-563)	O–D
	19	1977	(1745)	1129	(vs)	-33	(-28)	C=O
	20	1542	(1387)	50	(m)	+12	(+19)	H–C–O
	21	1399	(1259)	371	(s)	+72	(+81)	C–O
	22	1145	(1037)	93	(m)	+40	(+65)	D–O–C
	23	690	(651)	91	(m)	+74	(+91)	O–C=O
	24	218	(240)	46	(vs)[b]		NC	O···O

[a] Unless indicated, qualitative experimental intessity descriptions (in parentheses) are from Millikan and Pitzer, ref 10.

[b] Intensity labels from far infrared spectrum of ref 11.

[c] All predictions were made at the DZ+P SCF level of theory. Experimental results are given in parentheses. Note that theoretical vibrational frequencies are harmonic, while the experimental frequencies are the observed (anharmonic) fundamentals, taken from Bertie, Michaelian, Eysel, and Hager, ref 16. The controversial ν_{18} is from Excoffon and Marechal, ref 13.

[d] NC=no comparable monomer vibrational frequency.

Table VIII. Vibrational Frequencies (cm^{-1}) and IR Intensities (km/mol) for DCOOH[b]

		ω(theory)	int(theory)	ν(exptl)[a]	assignment
A'	1	4116	118	3566	O–H
	2	2458	87	2218	C–D
	3	1977	523	1760/1724	C=O
	4	1413	5	1297	H–O–C
	5	1311	254	1140	C–O
	6	1083	45	970	D–C–O
	7	683	62	620	O–C=O
A"	8	1000	9		D–C–O oop
	9	681	188	665	H–O–C oop

[a] Bertie et al., ref 16; Millikan and Pitzer, ref 39a; Miyazawa and Pitzer, ref 39b.
[b] All theoretical predications were made at the DZ+P SCF level of theory.

Table IX. Vibrational Frequencies (cm^{-1}) and IR Intensities (km/mol) for $(DCOOH)_2^c$

			freq	int[a]		(dimer−monomer)[b]		assignment
A_g	1	3782	(−)	0		-334	(−)	O–H
	2	2459	(2208)	0		+1	(-10)	C–D
	3	1896	(1643)	0		-81	(-117/-81)	C=O
	4	1536	(1385)	0		+123	(+88)	H–O–C
	5	1380	(1230)	0		+69	(+90)	C–O
	6	1101	(994)	0		+18	(+24)	D–C–O
	7	725	(672)	0		+42	(+52)	O–C=O
	8	180	(−)	0		NC		O···O
	9	163	(∼140)	0		NC		O–H···O ip
B_g	10	1013	(−)	0		+13	(−)	δC–D oop
	11	934	(−)	0		+253	(−)	δO–H oop
	12	218	(202)	0		NC		O–H···O oop
A_u	13	1014	(890)	28	(m,b)	+14	(−)	δC–D oop
	14	983	(930)	328	(m,b)	+302	(+265)	δO–H oop
	15	148	(−)	9		NC		O–H···O oop
	16	80	(−)	4		NC		twist about C–D bond
B_u	17	3834	(3098)	1599	(s)	-282	(-468)	O–H
	18	2456	(2251/2224)	199	(ms)	-2	(+33/+6)	C–D
	19	1956	(1726)	1191	(s)	-21	(-34/+2)	C=O
	20	1497	(1360)	30	(w)	+84	(+63)	H–O–C
	21	1384	(1239)	389	(s)	+73	(+99)	C–O
	22	1103	(996)	62	(m)	+20	(+26)	D–C–O
	23	740	(695)	85	(m)	+57	(+75)	O–C=O
	24	218	(−)	46		NC		O···O

[a] Experimental intensity descriptions are from Millikan and Pitzer, ref 10.
[b] NC= no comparable monomer vibrational frequency.
[c] All predictions were made at the DZ+P SCF level of theory. Experimental results are given in parentheses. Note that theoretical vibrational frequencies are harmonic, while the experimental frequencies are the observed (anharmonic) fundamentals, taken from Bertie, Michaelian, Eysel, and Hager, ref 16.

Table X. Vibrational Frequencies (cm^{-1}) and IR Intensities (km/mol) for DCOOD[b]

		ω(theory)	int(theory)	ν(exptl)[a]	assignment
A'	1	2995	71	2632	O-D
	2	2456	85	2232	C-D
	3	1973	504	1735	C=O
	4	1328	214	1170	C-O
	5	1145	3	945	D-O-C
	6	1061	54	1042	D-C-O
	7	611	58	556	O-C=O
A"	8	1000	10	873	D-C-O oop
	9	526	111	491	D-O-C oop

[a] Bertie and Michaelian, ref 15; Millikan and Pitzer, ref 39a; Miyazawa and Pitzer, ref 39b.
[b] All theoretical predications were made at the DZ+P SCF level of theory.

Table XI. Vibrational Frequencies (cm^{-1}) and IR Intensities (km/mol) for $(DCOOD)_2^c$

		freq		int[a]		(dimer−monomer)[c]		assignment
A_g	1	2759	(−)	0		-236	(−)	O–D
	2	2457	(2211)	0		+1	(-21)	C–D
	3	1887	(1648)	0		-86	(-87)	C=O
	4	1395	(1250)	0		+67	(+80)	C–O
	5	1196	(990)	0		+51	(+39)	D–O–C
	6	1091	(1081)	0		+30	(+45)	D–C–O
	7	665	(617)	0		+54	(+62)	O–C=O
	8	180	(−)	0		NC		O···O
	9	159	(130)	0		NC		O–D···O ip
B_g	10	1012	(892)	0		+12	(+19)	δC–D oop
	11	686	(−)	0		+160	(−)	δO–D oop
	12	214	(194)	0		NC		O–D···O oop
A_u	13	1014	(890)	26	(w,b)	+14	(+17)	δC–D oop
	14	730	(678)	195	(s)	+204	(+187)	δO–D oop
	15	143	(135)	8	(w)	NC		O–D···O oop
	16	80	(68)	4	(w)	NC		twist about C–D bond
B_u	17	2794	(−)	849	(−)	-201	(−)	O–D
	18	2455	(2226)	204	(s)	-1	(-6)	C–D
	19	1952	(1720)	1139	(vs)	-21	(-15)	C=O
	20	1395	(1246)	321	(s)	+67	(+76)	C–O
	21	1173	(1055)	14	(w)	+28	(+13)	D–O–C
	22	1085	(987/976)	88	(s)	+24	(+42/+31)	D–C–O
	23	685	(642)	90	(s)	+74	(+86)	O–C=O
	24	213	(227)	44	(s)	NC		O···O

[a] Experimental intessity designations (in parentheses) are from Millikan and Pitzer, ref 10, and Clague and Novak, ref 12.
[b] All predictions were made at the DZ+P SCF level of theory. Experimental results are given in parentheses. Note that theoretical vibrational frequencies are harmonic, while the experimental frequencies are the observed (anharmonic) fundamentals, taken from Bertie, Michaelian, ref 15.
[c] NC= no comparable monomer vibrational frequency.

Table XII. Raman Intensities for the Formic Acid Monomer[c]

		freq	exptl int	theor int	depolarization ratio	
		$\nu(cm^{-1})$[a]	(counts/s)[a]	($Å^4$/amu)	exptl	theory
A'	ν_1	3569	6	50.8	<0.1	0.27
	ν_2	2942	sh	78.2	<0.3	0.25
	ν_3	1777	9	8.5	0.1	0.21
	ν_4	1381	high T[b]	6.5		0.57
	ν_5	1223		1.2		0.43
	ν_6	1104	3	2.3	0.1	0.13
	ν_7	625	3	3.0	0.1	0.55
A"	ν_8	1033		0.9		0.75
	ν_9	642	0.5	0.9		0.75

[a] Bertie and Michaelian, ref 15.
[b] Observed only at high temperature.
[c] The theoretical results reported were obtained at the DZ+P SCF level of theory.

Table XIII. Raman Intensities for the Formic Acid Dimer, with Theoretical Results obtained at the DZ+P SCF Level of Theory[b]

		freq	exptl int	theor int	depolarization ratio	
		$\nu(cm^{-1})$[a]	(counts/s)[a]	($Å^4$/amu)	exptl	theory
A_g	ν_1			147.4		0.28
	ν_2	2949	100	203.1	0.1	0.26
	ν_3	1670	32	12.7	<0.1	0.10
	ν_4	1415	8	12.5	0.5	0.49
	ν_5	1375	7	2.3	0.4	0.65
	ν_6	1214	10	6.3	0.06	0.10
	ν_7	677	14	5.3	0.4	0.67
	ν_8	190		0.1		0.40
	ν_9	137	5	0.2	0.75	0.70
B_g	ν_{10}	1060	3	1.4	0.75	0.75
	ν_{11}			0.5		0.75
	ν_{12}	230	40	5.2	0.75	0.75

[a] Bertie and Michaelian, ref 15.

[b] Note that only Raman-allowed fundamentals of the dimer are included here.

Table XIV. Summary of Total (in hartrees) and Relative (in kcal/mol) Energies for the Formic Acid Monomer and Dimer

	STO-3G	DZ	DZ+P	exptl
monomer	-186.2179	-188.7061	-188.8144	
equilibrium dimer	-372.4599	-377.4429	-377.6516	
D_e for dimerization	15.1	19.3	14.3	
zero-point vib corr	-3.1	-2.5	-2.0	
D_0 for dimerization	12.0	16.8	12.3	$\leq$12.0[a]
$\triangle H_{300}$	12.6	17.2	12.5	14.8$\pm$0.5[b]
				14.1$\pm$1.5[c]
				11.7$\pm$0.1[d]

[a] Reference 20.
[b] Reference 17.
[c] Reference 51.
[d] Reference 52.

Table XV. Vibrational Frequencies (cm^{-1}) and IR Intensities (km/mol) for the Formic Acid Dimer Transition State (Point Group D_{2h})

		DZ		DZ+P		
		freq	int	freq	int	assignment
A_g	ν_1	3412	0	3313	0	C–H
	ν_2	1858	0	1845	0	H–O–C
	ν_3	1479	0	1554	0	C–O
	ν_4	788	0	821	0	H–C–O
	ν_5	536	0	555	0	O–H
B_{1g}	ν_6	1770	0	1910	0	C–O
	ν_7	1486	0	1513	0	H–C–O
	ν_8	237	0	239	0	H–O–C
	ν_9	1663i	0	1695i	0	O–H
B_{2g}	ν_{10}	1189	0	1210.3	0	δC–H oop
	ν_{11}	341	0	338	0	wag(CO_2)
B_{3g}	ν_{12}	1527	0	1460	0	δO–H oop
A_u	ν_{13}	133	0	99	0	twist (CO_2)
B_{1u}	ν_{14}	1574	571	1511	292	δO–H oop
	ν_{15}	1191	25	1209.8	26	δC–H oop
	ν_{16}	266	52	259	35	wag(CO_2)
B_{2u}	ν_{17}	1804	1463	1927	1392	C–O
	ν_{18}	1714	36	1704	1	C–O–H
	ν_{19}	1507	195	1524	134	H–C–O
	ν_{20}	629	19	641	10	O–H
B_{3u}	ν_{21}	3410	56	3311	79	C–H
	ν_{22}	1468	1246	1532	707	C–O
	ν_{23}	930	4034	962	4887	O–H + H–C–O
	ν_{24}	700	2683	779	3508	O–H + H–C–O

Table XVI. Summary of Total (in hartrees) and Relative (in kcal/mol) Energies for the Formic Acid Dimer[a]

	equilibrium dimer	transition dimer	reaction barrier
SCF/STO-3G	-372.4599	-372.4517	5.2
SCF/DZ	-377.4429	-377.4203	14.2
SCF/DZP	-377.6516	-377.6268	15.6
MP2/DZP	-378.714650	-378.704473	6.40
MP3/DZP	-378.719943	-378.706316	8.55
MP4(SDQ)/DZP	-378.742985	-378.729396	8.53
MP4(SDTQ)/DZP	-378.779543	-378.768345	7.09
CISD/DZP[b]	-378.645884	-378.632637	8.16
MP2/TZ2P	-379.024110	-379.011512	7.90

[a] MP2/DZP optimized equilibrium and transition state geometries.
[b] The core electrons are frozen in this calculation. The size-consistency correction is included.

Table XVII. Theoretical (MP2/DZP) Equilibrium and Transition State Geometries for the Formic Acid Dimer[a,b]

	Equilibrium	Transition State
$r(C_1{=}O_5)$	1.234	1.271
$r(C_1{-}O_3)$	1.320	1.271
$r(C_1{-}H_7)$	1.097	1.096
$r(O_3{-}H_9)$	1.003	1.203
$r(O_4\cdots H_9)$	1.665	1.203
$r(C_1\cdots C_2)$	3.800	3.540
$\angle O_3{-}C_1{=}O_5$	126.5	127.0
$\angle H_7{-}C_1{=}O_5$	121.9	116.5
$\angle H_7{-}C_1{-}O_3$	111.6	116.5
$\angle C_1{-}O_3{-}H_9$	109.1	115.4
$\angle O_3{-}H_9\cdots O_4$	178.4	177.7

[a] See Figure 1 in Chapter 4 for the atomic labelings.
[b] Bond distances in Å, angles in degree.

Table XVIII. Vibrational Frequencies for the Formic Acid Dimer Equilibrium and Transition State Geometry

equilibrium			transition state		
A_g	ν_1	3198	A_g	ν_1	3195
	ν_2	3185		ν_2	1728
	ν_3	1739		ν_3	1416
	ν_4	1502		ν_4	745
	ν_5	1419		ν_5	522
	ν_6	1275	B_{1g}	ν_6	1808
	ν_7	679		ν_7	1423
	ν_8	208		ν_8	231
	ν_9	171		ν_9	1199i
B_g	ν_{10}	1083	B_{2g}	ν_{10}	1063
	ν_{11}	1006		ν_{11}	325
	ν_{12}	280	B_{3g}	ν_{12}	1401.5
A_u	ν_{13}	1125	A_u	ν_{13}	86
	ν_{14}	1019	B_{1u}	ν_{14}	1454
	ν_{15}	189		ν_{15}	1064
	ν_{16}	79		ν_{16}	241
B_u	ν_{17}	3312	B_{2u}	ν_{17}	1793
	ν_{18}	3181		ν_{18}	1621
	ν_{19}	1806		ν_{19}	1419
	ν_{20}	1473		ν_{20}	593
	ν_{21}	1413	B_{3u}	ν_{21}	3194
	ν_{22}	1277		ν_{22}	1517.5
	ν_{23}	710		ν_{23}	1359
	ν_{24}	277		ν_{24}	794

Table XIX. Locations of the Global Minima in Normal Mode Coordinates[a]

A_g Symmetry	ab initio		Newton-Raphson	
	reactant	product	reactant	product
$Q_1^{(*)}$	-0.06	(-0.06)	-0.06	(-0.06)
$Q_2^{(*)}$	6.5	(6.5)	6.5	(6.5)
$Q_3^{(*)}$	-8.4	(-8.4)	-8.5	(-8.5)
$Q_4^{(*)}$	27.2	(27.2)	27.1	(27.1)
$Q_5^{(*)}$	94.3	(94.3)	94.3	(94.3)
$Q_6^{(*)}$	-3.1	(3.1)	-3.1	(3.1)
$Q_7^{(*)}$	1.5	(-1.5)	1.5	(-1.5)
$Q_8^{(*)}$	-75.9	(75.9)	-75.8	(75.8)
$Q_9^{(*)}$	46.4	(-46.4)	46.4	(-46.4)

[a] The subscripts of each modes are identical to those in Table XVIII. At the transition state, Q_9 is the reaction coordinate. Modes 1–5 have A_g symmetry in D_{2h} and behave even-coupling. Modes 6-9 have B_{1g} in D_{2h} and behave odd-coupling.

END

DATE FILMED

4/01/92